

ABSTRACT

Title of Document:

RELIABILITY OF LEAD-FREE HIGH
TEMPERATURE SURFACE MOUNT
COMPONENT ATTACHES

Timothy James Oberc, Master of Science, 2008

Directed By:

Associate Professor F. Patrick McCluskey
Department of Mechanical Engineering

This work investigates the relative reliabilities of SAC305, eutectic Au-Sn, and Ag-In transient liquid phase sintered (TLPS) solder joints subjected to high temperature passive thermal cycling. These solder materials were monitored for electrical resistance, mechanical pull strength, and microstructural changes during cycling. In fabricating the test assemblies, SAC305 and eutectic Au-Sn manufacturing parameters were gathered from the paste distributors while fabrication with Ag-In TLPS required in-house development. Work with the Ag-In TLPS paste revealed that reducing the additive (In) particle size led to statistically significant improvements in the solid volume fraction of the joints. Successful attachment of ceramic quadflat packs (CQFPs) to polyimide circuit boards using Ag-In TLPS demonstrated that surface mount joints with mechanical and electrical integrity could be manufactured from the material. Au-Sn was found to be the strongest of the materials while cracking in the SAC305 and Ag-In samples during cycling resulted in weaker joints.

RELIABILITY OF LEAD-FREE HIGH TEMPERATURE SURFACE MOUNT
COMPONENT ATTACHES

By

Timothy James Oberc

Thesis submitted to the Faculty of the Graduate School of the
University of Maryland, College Park, in partial fulfillment
of the requirements for the degree of
Master of Science
2008

Advisory Committee:

Dr. F. Patrick McCluskey, Chair and Advisor

Dr. Teng Li

Dr. Peter Sandborn

© Copyright by
Timothy James Oberc
2008

Dedication

To Rachel, Scruff McGruff, my parents and sister.

Acknowledgements

I would first like to thank my advisor, Dr. McCluskey, for all of his time and effort spent on this research. I would also like to thank my committee members, Dr. Teng Li and Dr. Peter Sandborn, for their input on how to improve the work herein.

I would also like to thank everyone in the McCluskey research group for making my time at the University of Maryland so enjoyable. Special thanks to Pedro, Rui, Lauren, Adam, and Rupal for being such good friends and teachers along the way.

I would also like to thank CALCE for the use of its facilities and equipment. Thanks in particular to Bhanu, Anshul, and Ahmed for their assistance in the labs.

Last, but certainly not least, I would like to thank Rachel and my family for their love and support during the creation of this work and for all the years leading up to it. I don't know where I would be today without all that you have given me.

Table of Contents

Dedication	ii
Acknowledgements	iii
Table of Contents	iv
List of Tables.....	vi
List of Figures	vii
Chapter 1: Introduction.....	1
1.1 Electronics for High Temperature Applications.....	2
1.2 Surface Mount Attach for High Temperature Environments	4
Chapter 2: Prior Work	10
2.1 SAC305 Studies	10
2.2 Eutectic Au-Sn Studies.....	13
2.3 TLPS for Surface Mount Attach.....	15
Chapter 3: Initial Embodiment of Ag-In TLPS Surface Mount Component Attach...	18
3.1 Selection of Ag-In System.....	18
3.2 Initial Ag-In TLPS Surface Mount Solder Joints	21
3.3 Ag-In TLPS Densification Study.....	23
3.3.1 Areal Analysis using ImageJ Software.....	24
3.3.2 Validation of Areal Analysis using the Point-Counting Method	26
3.3.3 Volume Fraction Trends	29
Chapter 4: Experimental Procedure.....	37
4.1 Test Vehicle Materials.....	37
4.1.1 Edge-card Circuit Boards.....	38
4.1.2 Ceramic Quadflat Pack Components.....	42
4.1.3 Combined Test Vehicle	45
4.1.4 Solder Pastes	46
4.1.5 Stencil Foils.....	48
4.2 Test Vehicle Fabrication.....	50
4.2.1 Stencil Printing	50
4.2.2 CQFP Placement	52
4.2.3 Reflow / Temperature Processing	53
4.3 Reliability Testing Procedures.....	64
4.3.1 Passive Thermal Cycling	66
4.3.2 In-situ Electrical Testing.....	68
4.3.3 Mechanical Pull Testing	70
4.3.4 Cross Sectional Sampling	72
Chapter 5: Reliability Assessment Results and Discussion.....	74
5.1 Solder Joint Strain Energy Density Estimation	75
5.1.1 Diagonal Lead Stiffness.....	76
5.1.2 Diagonal Length, CTE Mismatch, and ΔT	85
5.1.3 Minimum Load Bearing Area and Characteristic Solder Joint Height	86
5.1.4 Strain Energy Densities	88
5.2 Electrical Data Trends and Discussion.....	89

5.3	Mechanical Data Trends and Discussion	104
5.3.1	SAC305 Mechanical Results	106
5.3.2	Eutectic Au-Sn Mechanical Results	111
5.3.3	Ag-In TLPS Mechanical Results.....	115
5.4	Cross Sectional Data Trends and Discussions.....	119
5.4.1	SAC305 Microstructural Results	120
5.4.2	Eutectic Au-Sn Microstructural Results	127
5.4.3	Ag-In TLPS Microstructural Results.....	132
Chapter 6: Conclusions, Contributions, and Future Work.....		139
6.1	Conclusions.....	139
6.2	Contributions	141
6.3	Future Work.....	141
Appendix A – MATLAB Lead Compliance Formulas		142
Appendix B – MATLAB codes for Electrical Data Analysis.....		145
Works Cited		147

List of Tables

Table 1. Common electronic product temperature ranges.	2
Table 2. Solder alloys for HT applications.	7
Table 3. Point and volume fractions of an Ag-In surface mount solder joint.....	28
Table 4. Paste formulations for densification study.	33
Table 5. Omega furnace settings and procedures for proper reflow of SAC305 and eutectic Au-Sn.	60
Table 6. Ag-In TLPS processing open/close furnace door sequence.	63
Table 7. Sun Electronic Systems EC12 Controller LT and HT Programs.	67
Table 8. Average lead angles from 44-lead and 64-lead CQFPs.	80
Table 9. Estimated parameters of the inclined gull-wing structural model.	82
Table 10. Inclined gull-wing lead spring constants.....	84
Table 11. Characteristic solder joint heights and minimum load bearing areas.	88
Table 12. Strain energy densities.	89
Table 13. Strain range estimations.	89
Table 14. Adjusted Electrical Sample Populations.	103
Table 15. Observed mechanical testing periods and samples.	105
Table 16. SAC305 ANOVA results.	111
Table 17. Eutectic Au-Sn ANOVA results.	114
Table 18. Ag-In TLPS ANOVA results.....	117
Table 19. Observed cross section sampling schedule and sizes.....	120
Table 20. EDS point scan results of SAC intermetallic.....	127
Table 21. EDS point scan results of Au-Sn bulk solder.	128

List of Figures

Figure 1. Inclined gull-wing leaded surface mount package.	5
Figure 2. Temperature vs. time of a sample reflow profile for Sn-Ag-Cu solder.	6
Figure 3. Ag-In Binary Phase Diagram from Hansen and Anderko [30].	19
Figure 4. ImageJ transformation from threshold adjustment.	25
Figure 5. Bounded joint for area fraction analysis.	25
Figure 6. Point-counting method grid overlay.	28
Figure 7. Volume fraction as a function of particle ratio ($R = D_{Ag}/D_{In}$).	34
Figure 8. Ag-In TLPS unprocessed paste ESEM/EDS images (Ag in red).	35
Figure 9. Wetting comparison of P1 and P4 pastes under large package leads.	36
Figure 10. Small CQFP footprint.	39
Figure 11. Large CQFP footprint.	39
Figure 12. Polyimide test board edge-card feature.	40
Figure 13. Polyimide test board design.	41
Figure 14. 64-lead CQFP daisy chain wiring scheme.	43
Figure 15. 44-lead CQFP daisy-chain wiring scheme.	44
Figure 16. Desired CQFP Gull-wing geometry (not to scale).	45
Figure 17. Test vehicle metallization stack-up.	46
Figure 18. Stencil foil design in EAGLE 4.16.	49
Figure 19. Stencil printing fixture.	51
Figure 20. Stencil printing orientation and direction.	51
Figure 21. CQFP component placement fixture.	53
Figure 22. Furnace temperature testing thermocouple arrangement.	55
Figure 23. Manufacturer's recommended SAC305 reflow profile.	57
Figure 24. SAC305 reflow profile as measured within Omega furnace.	58
Figure 25. Manufacturer's recommended eutectic Au-Sn reflow profile.	59
Figure 26. Eutectic Au-Sn profile as measured within Omega furnace.	60
Figure 27. Ag-In TLPS profile as measured within Omega furnace.	64
Figure 28. LT and HT profiles.	67
Figure 29. Electrical testing wiring.	70
Figure 30. 45° pull test sample orientation [46].	71
Figure 31. Pre-cut locations on polyimide test board.	72
Figure 32. Structural model for inclined gull-wing [49].	78
Figure 33. Lead angle definitions.	79
Figure 34. Geometric overlay of cross section images to estimate gull-wing structure.	81
Figure 35. Measurement definitions in estimating characteristic solder joint height.	87
Figure 36. Au-Sn chain resistance and temperature as a function of passive thermal cycling time.	92
Figure 37. Representative baseline resistance signature of a 44-lead CQFP, SAC305 daisy chain.	94
Figure 38. Chain resistance degradation as a function of passive thermal cycles.	96
Figure 39. Potential failure sites within electrical wiring.	98
Figure 40. Resistance trend of a chain completed by an aluminum insert.	100

Figure 41. Observed chain similarities across varying samples and connectors.	101
Figure 42. Interfacial failure between component lead and solder joint during pull strength testing.....	106
Figure 43. Pull strength trends of SAC, 64-lead CQFP samples.	108
Figure 44. Pull strength trends of SAC, 44-lead CQFP samples.	109
Figure 45. Pad lift failure mode during pull strength testing.	112
Figure 46. Pull strength trends of Au-Sn, 44-lead CQFP samples.....	113
Figure 47. Pull strength trends of Au-Sn, 64-lead CQFP samples.....	114
Figure 48. Pull strength trends of Ag-In TLPS, 44-lead CQFP samples.....	116
Figure 49. Pull strength trends of Ag-In TLPS, 64-lead CQFP samples.....	116
Figure 50. Comparison plot of solder material pull strengths.....	119
Figure 51. SAC305 64-lead CQFP joint subjected to 0 thermal cycles.	121
Figure 52. SAC305 64-lead CQFP joint subjected to 800 LT thermal cycles.....	122
Figure 53. SAC305 64-lead CQFP joint subjected to 800 HT thermal cycles.	122
Figure 54. Intermetallic layer growth and crack progression in SAC 64-lead CQFP HT joints.....	123
Figure 55. SAC lead side intermetallic thickness as a function of thermal cycles...	124
Figure 56. SAC305 44-lead CQFP HT solder joint heel imaged using light microscope.....	125
Figure 57. EDS Map of lead side intermetallic.....	126
Figure 58. EDS Point Scan locations.....	126
Figure 59. Truncated Au-Sn binary phase diagram [56].	128
Figure 60. Phase distribution within eutectic Au-Sn solder joint.....	129
Figure 61. Solder joint heel of an Au-Sn 44-lead CQFP LT sample.	129
Figure 62. Lack of fatigue and microstructural coarsening in Au-Sn 64-lead CQFP HT solder joints.	131
Figure 63. Ag-In TLPS 64-lead CQFP solder joint subjected to 0 thermal cycles. .	132
Figure 64. Ag-In TLPS lead side intermetallic thickness as a function of thermal cycles.....	133
Figure 65. Au-In Binary Phase Diagram from [30].....	134
Figure 66. Crack progression in Ag-In TLPS 64-lead CQFP HT solder joints.	135
Figure 67. Cracking in Ag-In TLPS 44-lead CQFP HT solder joint subjected to 400 HT cycles.....	136
Figure 68. EDS map of Ag-In particle.....	137
Figure 69. Evidence of silver diffusion from Ag-In particles within Ag-In TLPS matrix.	137

Chapter 1: Introduction

The world of electronics has become an expansive realm that touches our lives in many ways. Electronic systems are now available for a wide array of functions ranging from computational aides and monitoring devices to defense systems and information networks. These systems have contributed to a significant increase in the standard of living around the world. Research in the field of electronics, as in any other, has encompassed the continual pursuit of new knowledge that can be used to improve existing products as well as to develop novel technologies capable of previously unachievable feats. The boundaries that limit the capability of electronic technologies are continually expanded by these research efforts, which have subsequently resulted in an ever-increasing variety of electronic products.

Due to the overwhelming variety of electronic products that exist, categorization of these devices is required to simplify discussion within the field. At its highest level, this categorization can serve to qualitatively group electronic products based on their end use within society. Another more useful categorization of electronic products serves to organize them based upon some metric that describes their capabilities or conditions of use. A popular method of quantitative categorization uses the temperature ranges over which the technologies are designed to operate. In particular, all electronic technologies can be categorized as capable of operating within the commercial, industrial, military, or extreme temperature ranges. These temperature ranges are provided in Table 1 [1][2].

Table 1. Common electronic product temperature ranges.

	Temperature Range (°C)
Commercial	0 to 70
Industrial	-40 to 85
Military	-55 to 125
Extreme	Below -55 or Above 125

As the table above shows, the extreme temperature range covers any electronic technology capable of operating from below -55°C , commonly referred to as the low temperature (LT) range, or above 125°C , commonly referred to as the high temperature (HT) range [2]. As the title of this work indicates, this thesis investigation will address a portion of the packaging required for electronic products capable of performing within the HT range.

1.1 Electronics for High Temperature Applications

The push for electronic technologies capable of operating in high temperature environments has resulted from the need for the electronics to perform distributed sensing, actuating, and control functions in harsh, uncontrolled environments. Common applications of electronics in distributed sensing and control systems subjected to HT conditions can be found in the automotive, avionics, and energy exploration industries. Distributed sensing and control, which refers to the implementation of signal processing and control capabilities local to the sensors interacting with the environment, improves system performance over the conventional centralized architecture where signal processing capabilities are housed away from the sensing elements. An example of distributed control is a drill system in a HT down-hole environment capable of sensing pressure and adjusting the rotational speed without needing to send a signal back to the surface for processing;

all sensing and computation takes place down-hole, effectively eliminating the need for wiring between the drill-head and surface. The application of HT electronics in a particular system is often preferred over the alternative of implementing standard temperature electronics in these applications because they can be operated at higher temperatures than their normal temperature counterparts, therefore eliminating the need for passive or active cooling technologies that can add cost and complexity to a given sensing and control system.

In order for electronic systems to be capable of withstanding HT conditions, all electronic components of the system must be able to reliably operate in the given environment. Proper operation of the electronic components is dependent upon the temperature related behavior of the electrical devices on the die in addition to the materials used to package it. Some newer devices fabricated from silicon carbide (SiC) have been successfully operated at temperatures of 500°C [3][4] while other sources have claimed operation at temperatures up to 600°C. These temperatures are well above the capability of silicon (Si) devices, which cannot be used above ~300°C due to limits imposed by the material's reverse breakdown voltage [5]. With new SiC devices able to operate at increasingly higher temperatures, the development of materials to package and connect them at these temperatures remains a significant hurdle that must be overcome. The foremost materials-related problem addressed by researchers within the packaging community has been that of the first-level interconnection between device and substrate. Suggested die attach technologies to satisfy this packaging problem have ranged from exotic, high melting point alloys to various sintered metals and even high temperature organic attaches. Although this

first level of interconnection is an important packaging task to address, it is also critical to research materials suitable for other levels of interconnection as well. This thesis seeks to contribute to the knowledge base regarding second level interconnection of surface mount devices to printed wiring boards (PWB) for HT conditions.

1.2 Surface Mount Attach for High Temperature Environments

Second level interconnection of electronic packages can be achieved in a number of ways. Prior to the advent of the surface mount package, 2nd level interconnection was performed using through-hole connection of packages, whereby leads attached to the electronic parts were inserted into plated through holes in the circuit board and an interconnection was made by filling the space around the lead in the hole with molten solder which was then allowed to solidify. The shift to surface mounted components has largely eliminated through-hole connections, allowing for the miniaturization of many electronic systems by increasing utilization of the PWB area. The shift to surface mounting of electronic components has spurred the invention of a wide array of package geometries that include the commonly used small outline (SOP), quad flatpack (QFP), ball grid array (BGA), and the more unique column grid array and leadless chip carrier packages. All of these package designs incorporate unique features for use in connecting to the PWB. In particular, devices on QFPs are connected to the PWB in part through surface mount leads bent into gull-wing geometries. An illustration of a surface mount package featuring inclined gull-wing leads can be seen in Figure 1.

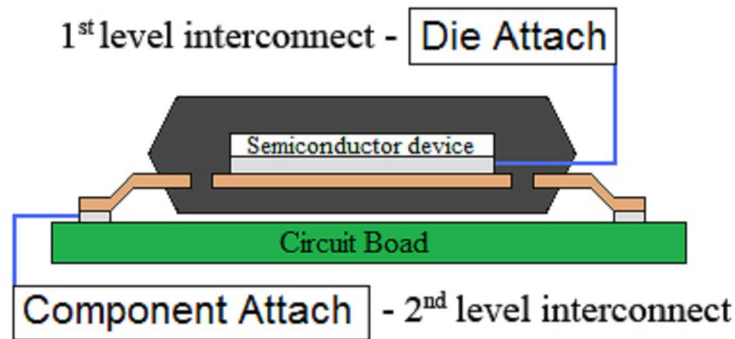


Figure 1. Inclined gull-wing leaded surface mount package.

Second level interconnection relies on component attach to serve critical electrical and mechanical functions. Electrically, the component attach is called upon to carry an electrical signal between the leads and the PWB without distortion or discontinuity. With respect to its mechanical function, it is required to fasten the component to the PWB and resist any loading that would separate the two. Although these two functions are distinct, it is clear that they are interrelated because without a mechanical connection, electrical continuity cannot exist. Some surface mount component attaches also serve a thermal function by transmitting heat from the semiconductor device to the PWB.

The common method of manufacturing joints between the surface mount package and PWB involves the screen or stencil printing of a metal paste onto the PWB and subsequent placement of the surface mount package on top of the printed paste pads. The entire assembly is then subjected to a temperature profile that includes a hold time in which the melting temperature of the metal paste is exceeded, followed by cooling to a temperature at which the joints solidify. This temperature excursion is referred to as reflow and a sample profile is shown in Figure 2. Put another way,

reflow processing of electronic assemblies operates on the basic principle that the maximum temperature of reflow, T_r , must exceed the melting temperature, T_m , of the surface mount component attach.

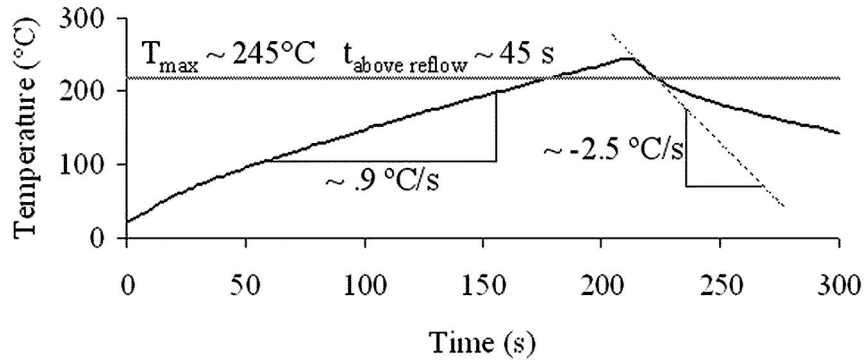


Figure 2. Temperature vs. time of a sample reflow profile for Sn-Ag-Cu solder.

In order for the surface mount solder joints to perform their intended functions at a given temperature they must be solid, which implies the application temperature, T_a , needs to remain lower than T_m . This translates into the need for solder materials with higher melting temperatures when a surface mount component attach is required for HT conditions. Solder materials commonly used for products subject to the commercial temperature range are typically not implemented as part of an electronic product subject to HT conditions because of their lower melting temperatures. For example, the popular component attaches of 96.5 wt. % Sn 3.0 wt. % Ag 0.5 wt. % Cu (SAC305) and the former industry standard, 63 wt. % Sn 37 wt. % Pb (eutectic Sn-Pb) feature melting temperatures of 217°C and 183°C, respectively. Although some HT conditions may not exceed these temperatures, the threat of time dependent deformation is a common reliability concern when using these solders at elevated temperatures because the proximity of the operating temperatures to the melting point

of the material is known to accelerate the creep phenomenon. Because of these reliability concerns, many gold-based solders and high-Pb alloys are utilized for HT conditions because of their higher melting temperatures and resistance to creep. A few of these alloy formulations are listed in Table 2. For those combinations that are off-eutectic, the temperature range is given for the melting temperature.

Table 2. Solder alloys for HT applications.

Solder Alloy (wt. %)	Solidus Temperature (°C)	Liquidus Temperature (°C)
97Au 3Si	363	363
88Au 12Ge	356	356
95Pb 5Sn	308	312
80Au 20Sn	280	280
90Pb 10Sn	275	302

As the table shows, these melting temperatures are significantly higher than those of SAC305 and eutectic Sn-Pb. Typical reflow profiles call for peak temperatures ~30 to 40°C above a solder's liquidus temperature, meaning that implementation of these HT solder alloys would require profiles with peak temperatures ranging from ~310 to 400°C. Such high temperature reflow profiles can lead to significant processing related damage of the assembly and component materials prior to application. These damages may include charring of the PWB, delamination of the copper from the boards, popcorning, outgassing, and burning of the component encapsulant as well as increased intermetallic formation. In addition to such damage, residual stresses built into the electronic assembly are proportional to the absolute difference between peak reflow and room or operating temperature. As a result, the reflow profiles for HT solders can lead to increased residual stresses within the assemblies, which together with thermal damage translates into consumption of an appreciable amount of the assembly's useful life prior to implementation in the field.

In order to avoid the necessity of processing at such elevated temperatures to achieve a HT second-level interconnection, a transient liquid phase sintered (TLPS) material has been investigated as a possible solution. TLPS is a variation on liquid phase sintering whereby a liquid is formed and consumed by diffusional homogenization during the sintering process [6]. In effect, the processing temperatures for TLPS materials remain below the melting point of at least one of the material constituents, so that solid and liquid phases coexist until the liquid is completely consumed by the diffusional process. When the material constituents are chosen carefully, the TLPS process can be a very powerful tool in the manufacture of HT electronics. During this investigation, implementation of a TLPS material composed of a select ratio of Ag and In powders subject to processing temperatures more commonly associated with SAC305 yielded a high temperature component attach that can remain solid up to at least 540°C. Although TLPS processing offers an attractive alternative to traditional reflow processing, the transient liquid during the process is influenced by several parameters that make TLPS extremely sensitive to processing conditions [6]. Prior work with the Ag-In TLPS system [7][8] provided the necessary predictive capabilities for manufacturing interconnections from the Ag-In TLPS material. This work serves to investigate the feasibility of implementing the Ag-In TLPS material as an alternative high temperature component attach by utilizing common surface mount attach fabrication methods to fabricate samples and compare them to assemblies manufactured from commercially available solder pastes: SAC305 and 80 wt. % Au 20 wt. % Sn (eutectic Au-Sn). The successful application of the Ag-In TLPS alloy as a 2nd level interconnection not only depends on whether surface mount joints can be

successfully fabricated from the material, but also on how reliable the subsequent joints are when subjected to environmental stressing conditions. Relative reliability of the three component attaches was determined from HT passive thermal cycling of samples fabricated on identical test vehicles that were monitored for changes in critical mechanical and electrical metrics.

Chapter 2: Prior Work

This chapter outlines the results of prior work that were employed in developing the design and manufacturing approaches used in this study. In the manufacturing of interconnections from the commercially available surface mount materials, SAC305 and eutectic Au-Sn, an effort was made to adhere to commonly accepted manufacturing practices gathered from the available literature. With respect to the Ag-In TLPS material, efforts were made to utilize the previous work [7][8] regarding implementation of this processing method and binary metallic system while contributing original work that serves to advance it as a HT surface mount component attach and encourage future investigation in this area.

2.1 SAC305 Studies

RoHS and WEEE legislation has served as a catalyst for significant materials related research aimed at identifying a suitable replacement for the former industry standard solder paste, eutectic Sn-Pb. Now that these directives have been in effect for over two years, a number of ternary and quaternary alloys composed of select ratios of tin, silver, and copper have become the front runners for manufacturing of commercial electronic products that feature surface mount technology. Of the ternary alloys, SAC305 has been heavily researched as an attach material for a wide variety of electronic packages and applications. These investigations have attempted to provide behavior predictive data so that users of the surface mount attach possess a good understanding of the limitations associated with its manufacture and application environments. With respect to this investigation, all recommended manufacturing

processes regarding the SAC305 paste were readily available from the paste supplier. The handling, application, and temperature control of test assemblies manufactured with the SAC305 material were all performed according to these recommendations. This information included the recommended reflow profile tailored to the particular flux packaged with the SAC305 alloy. Discussion of the joint manufacture for this solder paste is provided in detail within the experimental methods of this work. In an effort to make contributions in the area of testing SAC305, investigations were consulted to understand the limits of past temperature related environmental testing on SAC assemblies. This information, when assessed along with that collected for eutectic Au-Sn and Ag-In TLPS, provided important data that aided in the selection of the type and magnitude of environmental testing of the experimental assemblies.

As a direct result of the research resources dedicated to understanding SnAgCu solders, solder pastes such as SAC305 are now widely used materials in electronics manufacturing. Because these solder materials have been tasked with replacing eutectic Sn-Pb, much research has gone into uncovering how SnAgCu solders would perform under material and environmental conditions similar to those of the former Sn-Pb assemblies. Although SnAgCu alloys have served as suitable replacements to leaded solders, changes to the electronics manufacturing industry were required to accommodate them. The most notable of these adaptations was that made to the reflow profile. Lead-free alloys like SAC305 ($T_m = 217^\circ\text{C}$) require higher reflow temperatures on the order of ~ 240 to 250°C to process the pastes. In contrast to the eutectic Sn-Pb melting temperature of 183°C , this higher SnAgCu melting temperature opens up the possibility of elevated temperature applications

inappropriate for electronic assemblies featuring eutectic Sn-Pb attaches. Based on a survey of the current temperature tests performed on SAC assemblies, the maximum temperature of many of these investigations has been $\sim 150^{\circ}\text{C}$. Choubey et. al. [9][10][11] worked to characterize the intermetallic growth between lead-free solders, including SAC305, and various board metallizations at aging temperatures up to 150°C . In one particular investigation [10], the growth constants and activation energies of intermetallic formation for the various lead-free solders and finish combinations were predicted from the collected data. The effect of aging temperature and board finish on the pull strength of surface mount leads were also assessed as a function of time at aging temperature. In Kim et. al. [12], lead-free and eutectic Sn-Pb solders were used to fabricate solder joints that were subjected to temperature cycling from room temperature up to a maximum of 150°C . The fatigue testing of these samples demonstrated that for higher ΔT values, eutectic Sn-Pb solders exhibited higher fatigue resistance while for lower ΔT values, the lead-free assemblies exhibited higher fatigue resistance. An investigation performed by Suhling et. al. [13] featured passive thermal cycling of lead-free ternary and lead-free quaternary alloy samples between -40 and 125°C as well as -40 and 150°C . In contrast to other similar studies, the samples fabricated for that investigation paired ceramic chip resistors with organic circuit boards in an attempt to simulate the material combinations of automotive electronics. Lastly, Ma et. al. [14] assessed the relative reliability of SnAgCu solders during temperature aging tests at maximum temperatures of 150°C . From the temperature related lead-free investigations that were reviewed in preparation for this study, it is clear that passive thermal cycling

and temperature aging tests are popular environmental conditioning schemes for evaluating the reliability of lead-free and eutectic Sn-Pb systems. From these studies [9][10][11][12][13][14], it is clear that the commonly used maximum temperature for testing of the lead-free assemblies has been 150°C. In an effort to supplement these types of reliability studies, the maximum temperature of testing during this investigation will push the limits of these prior works and assess the reliability of SAC305 surface mount solder joints at even higher temperature extremes. The resulting data could prove useful to those looking to implement a lead-free solder paste alloy for more demanding HT applications.

2.2 Eutectic Au-Sn Studies

In contrast to the wealth of studies and data available for SnAgCu, the investigations conducted on eutectic Au-Sn are fewer. The comparatively smaller number of applications for the material combined with its significantly higher cost translates into fewer studies on the alloy. Featuring a melting temperature of 280°C, eutectic Au-Sn is an alloy capable of surviving many demanding HT applications. This hard solder is well known for its excellent fatigue and creep resistance due to its high flow stress [15] and high melting temperature, which make it an ideal candidate to serve as a HT baseline against which the performance of the SAC305 and Ag-In TLPS solders can be compared in this study. Many applications of the eutectic Au-Sn alloy feature solder preforms shaped as ribbons, pellets, or ring frames [16]. However, as the size and pitch of surface mount devices continue to decrease, the feasibility of preforms as an option in manufacturing HT electronic assemblies decreases as well. Early studies

with the Au-Sn alloy demonstrated that highly reliable joints could be formed with eutectic Au-Sn preforms. In studies conducted by Matijasevic and Lee [17][18], GaAs devices were successfully attached to alumina substrates using eutectic Au-Sn preforms. In order to ensure void-free attachment, pressure was applied to the die/preform/substrate stack-up when subjected to the reflow profile. Further study [19] demonstrated that silicon devices could be successfully attached to alumina substrates in the same manner. In all three of these studies, thermal shock testing of the samples between -196 and 160°C demonstrated reliability in that all test assemblies avoided joint or die cracking during testing. In contrast to the performance of eutectic preforms, the application of eutectic Au-Sn solder paste has shown the tendency to form voids in joints and attachments fabricated from the paste material [16][20]. Fabrication with eutectic Au-Sn preforms is often flux free and pressure assisted, circumventing the voiding associated with flux containing solder pastes. However, minimization of voids within Au-Sn bonds comes at a cost: manufacturing of electronic assemblies through the application of Au-Sn solder preforms is complicated by the need for more fixturing and features lower throughput when compared to conventional stencil printing methods. In an effort to make the implementation of eutectic Au-Sn pastes more practical and appealing, the work by Ishikawa et. al. [16] addressed the voiding issues inherent in the manufacturing process of Au-Sn pastes. Recommendations from the work ranged from lowering the surface oxidation of the metals by using larger particle sizes to increasing the temperature and time of the reflow profile preheat stage to making slight changes to the composition of the alloy by moving to ~ 1 to 2 wt. % richer in Sn [16]. Although

eutectic Au-Sn is commercially available in paste form, there are few studies in existence that investigate this embodiment of the alloy as a surface mount component attach. The work performed during this investigation will serve to augment the available data on the Au-Sn alloy by conducting passive thermal cycling under unique temperature excursions and subsequent stressing conditions for the flux containing solder paste version of the alloy. Successful manufacture of Au-Sn solder joints without the aid of an inert atmosphere during reflow will demonstrate manufacturability of the paste using standard electronics manufacturing practices.

2.3 TLPS for Surface Mount Attach

While the SAC305 and eutectic Au-Sn alloys are well characterized, commercially available solder materials, the novel Ag-In TLPS material proposed as a surface mount attach for this investigation will require significantly more process development to successfully attach surface mount components to the PWB. Although the principle of TLPS has been investigated and demonstrated for a number of material systems and applications, there has not yet been a translation of the technology to successfully attach surface mount components to the PWB using traditional manufacturing methods. Furthermore, there has not been any work that serves to assess the viability of such an attach material based upon its behavior during environmental testing. Prior work [21][22] with the Sn-Bi and Sn-Sb systems demonstrated that solder pastes mixed from elemental particles and flux were able to undergo a shift in melting temperature that resulted from compositional homogenization that occurred during the TLPS process. However, further steps to

attach surface mount components to circuit boards with these pastes in order to assess their performances under environmental stresses were not undertaken. In addition, the melting temperature shifts exhibited during studies of the Sn-Bi and Sn-Sb were within the 140 to 250°C range which are notably lower than those possible when using the Ag-In system. In Palmer et. al. [23], bonding of copper strips was accomplished using liquid assisted sintering of an altered commercial solder paste. During this investigation, Sn-Ag solder paste was doped with an Sn-Bi alloy that served as the liquid forming constituent during temperature processing. Joints formed between the copper strips using liquid assisted sintering demonstrated mechanical strength values comparable to Sn-Pb joints while those Sn-Ag joints sintered without the Sn-Bi metal present in the mixture failed to demonstrate mechanical integrity. Successful attachment of surface mount components using hybrid conductive adhesives that implemented TLPS to form internal metallic frameworks was accomplished by Gallagher and Shearer [24][25]. The cohesive structures formed by the metals having undergone TLPS were shown to have improved the mechanical integrity of samples fabricated with the hybrid conductive adhesive over those fabricated with discrete metallic particles dispersed in the adhesive matrix. More recently, a multi-stage study of the Ag-In system processed through TLPS was completed [7][8]. This investigation, conducted at the University of Maryland, first worked to provide modeling tools that would allow for prediction of required processing related parameters during TLPS manufacture of the Ag-In system based on a number physical considerations that included silver particle size, constituent weight ratios, ramp rate during processing, isothermal temperature during processing,

and isothermal hold time [8]. Subsequent work with the Ag-In TLPS material provided electrical and mechanical characteristics of the processed material as a function of constituent weight ratios and concluded with the demonstration of the material's applicability as a die attach for HT or high power environments. Although successful attachment of silicon devices to alumina substrates was demonstrated [8], a full reliability analysis of the Ag-In TLPS was never conducted. In addition, the use of the material as a surface mount attach was not investigated. The encouraging results from this work served to inspire the investigation of the Ag-In TLPS system as a viable HT surface mount attach as part of this study. The work performed on the Ag-In TLPS system during this investigation will serve to demonstrate its manufacturability using common surface mount manufacturing methods. Inherent in this demonstration will be the successful attachment of surface mount components using the Ag-In TLPS paste. Lastly, this work will provide novel data regarding the material's reliability during environmental conditioning when used as a surface mount solder joint.

Chapter 3: Initial Embodiment of Ag-In TLPS Surface Mount Component Attach

3.1 Selection of Ag-In System

Before discussing the initial embodiment of the Ag-In TLPS solder attach, it is necessary to give some insight into why the binary system was selected as a candidate for applying TLPS manufacturing. Many researchers [21][22][26][27][28][29] have worked on understanding and applying the TLPS process for their particular alloy of interest. The phase diagrams of these selected systems feature characteristics that are conducive to producing a successful TLPS compact. Systems such as Au-Sn, Al-Au, Fe-Ti, Fe-Al, Ag-Sn, Cu-Sn, Sn-In, Sn-Bi and Ag-In, among others, have been identified or used as TLPS candidates due to availability of a comparatively low melting temperature eutectic or additive liquid during processing.

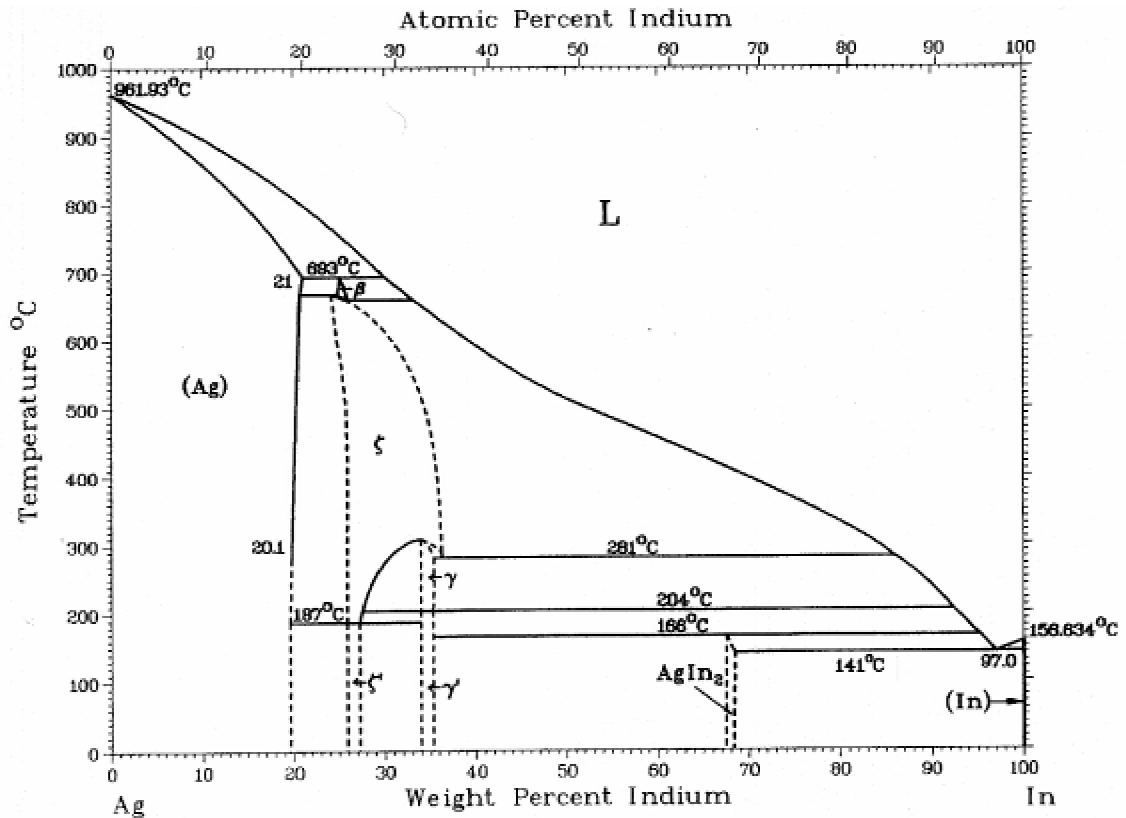


Figure 3. Ag-In Binary Phase Diagram from Hansen and Anderko [30].

With respect to the Ag-In system, the phase diagram shown in Figure 3 demonstrates a few features that made it attractive to use for TLPS processing of HT solder joints. First, the additive metal, indium, has a large solid solubility in silver. As the diagram shows, up to 20 wt. % indium can be accommodated within the silver phase over a wide temperature range while additional high melting temperature phases extend all the way to ~35 wt. % indium. This solubility of indium in the base metal, silver, is an important characteristic as it allows for a substantial amount of liquid forming additive to exist during initial stages of TLPS prior to compositional homogenization. In prior applications of TLPS materials, the systems have generally been constrained by the surrounding surfaces of a mold or combination of die and substrate. These constraints leave the liquid formed during processing largely responsible for the

rearrangement and densification of the base metal prior to solidification. However, during TLPS processing of surface mount solder joints, the liquid is also required to form the desired heel and toe geometries common to surface mount solder joints. Because of this additional requirement, the availability of a significant amount of liquid is a very desirable characteristic in the TLPS manufacturing of surface mount solder joints. In addition to the availability of liquid, the melting point differential between silver and indium makes it an attractive system because indium rich liquid can be formed at temperatures significantly lower than the melting temperature of the final composition. For example, during prior investigations with this system [26][27] a final composition of 75-80 wt. % Ag and 20-25 wt. % In was set prior to processing through deposition of thin films. Subsequent processing of these thin films at ~200 to 220°C over time (many hours) yielded a bond capable of remaining completely solid up to 693°C with a liquidus temperature of ~750 to 780°C. This subsequent shift in melting temperature is significant because it allows for the relatively low temperature processing of HT materials. Lastly, silver and indium metals are commonly used materials in electronics packaging. Silver features the highest electrical conductivity of any element while indium is a metal commonly recognized for its exceptional wetting abilities. Because of the aforementioned characteristics, Ag-In was considered one of the most promising binary alloy systems to manufacture surface mount assemblies using TLPS.

3.2 Initial Ag-In TLPS Surface Mount Solder Joints

Before the Ag-In TLPS material could be tested as part of any reliability study, its application as a surface mount attach needed to be demonstrated first. Although Ag-In paste had been used to successfully attach silicon devices to alumina substrates [8], the physical characteristics of the application were different than those of surface mount components. In particular, the volume of material deposited for attachment of the 10 mm by 10 mm devices [8] was well over 100 times what is needed for attachment of a surface mount lead. A material that performs well when applied in comparatively large volumes does not necessarily behave the same way when these amounts are significantly scaled down. Additionally, when applied as a surface mount component attach, the Ag-In TLPS material will need to demonstrate compatibility with common PWB metallizations whereas the aforementioned silicon devices and alumina substrates were coated with a layer of silver to facilitate bonding.

In recognition of these differences, a paste was mixed from -325 mesh silver and indium particles and a commercially available, high temperature, no-clean flux in order to demonstrate that Ag-In TLPS could be applied as a surface mount component attach. The composition of the metal load was selected to be 75 wt. % Ag and 25 wt. % In, which was well within the compositional window (< 35 wt. % In) that would result in the desired melting point shift during TLPS. For stencil printing purposes, the metal load of the paste was set to 91% by weight during the mixing process. The resulting Ag-In TLPS paste was printed onto ENIG, polyimide PWBs through an 8-mil (200 μ m) thick stencil prior to surface mount component placement

and temperature processing. Additional details regarding these materials and methods are provided in the experimental procedure section of this work.

The resulting Ag-In TLPS solder joints demonstrated mechanical integrity and electrical conductivity; however, the density and wetting behavior of the material needed improving. Because the silver within the mixture does not melt during processing, the resulting TLPS joints are inherently porous. In response to this, subsequent formulations of the Ag-In paste were mixed to a composition of 67 wt. % Ag and 33 wt. % In to provide additional indium rich liquid during processing for improved wetting and densification. In order to further improve densification of the joints, the effect of indium particle size on joint volume fraction was investigated. The methods and results of this study will be discussed in the following section.

Lastly, fabrication of the initial Ag-In joints demonstrated that paste control during deposition and component placement is critical, as the Ag-In TLPS paste does not self-align during processing like other solder pastes. This is due to the fact that only a fraction of the joint melts during processing. The excessive paste volume that resulted from printing with an 8-mil (200 μm) thick stencil was addressed in subsequent fabrications by using a 6-mil thick (150 μm) stencil instead. Apertures of this 6-mil (150 μm) stencil were also adjusted to deposit slightly smaller solder pad footprints as well. These adjustments allowed for improved paste control during fabrication of the Ag-In TLPS samples for reliability testing.

3.3 Ag-In TLPS Densification Study

In order to quantify the porous nature of the Ag-In surface mount joints formed during TLPS processing, cross sections were prepared and imaged using a light microscope and accompanying camera. In this investigation it was observed that as the grit size of the abrasive cross sectioning paper decreased, the probability and frequency of material scooping increased during polishing of the Ag-In samples. In order to avoid removal of material from the plane of interest, sample preparation was adjusted accordingly. Infiltration of the porous Ag-In joints was performed by pouring the liquid mixture of epoxy and hardener over the surface mount joints prior to the removal and potting of the joint as an individual sample. This ensured that vibration during sample cutting did not cause additional cracking or damage to the solder joint as well as provided the liquid epoxy-hardener mixture the opportunity to penetrate the porous structure of the surface mount joints prior to potting. In addition to infiltrating the samples prior to potting, a rougher polishing scheme was used to prepare cross sections to measure volumetric density of the Ag-In joints. These samples were subjected to 240 and 400 grit treatments only. In contrast, all samples prepared for imaging of any visual progression that occurred during passive thermal cycling were subjected to 240, 400, 600, 800, and 1200 grit treatments to provide a polished surface capable of highlighting stress-related cracking. All grinding and polishing paper used for sample preparation during this investigation featured silicon carbide as the abrasive material.

3.3.1 Areal Analysis using ImageJ Software

Following the 400 grit treatment of the samples prepared for volume fraction measurements, images of the cross sections were collected for analysis. The National Institute of Health (NIH) image processing software, ImageJ, was used to estimate the volume fraction of the samples using their cross section images. First, unprocessed images were cropped to areas surrounding the solder joint to limit the file size.

Following this, the black/white threshold of the image was adjusted so that areas in which material existed were transformed into pure black pixels whereas those areas void of material were transformed into pure white pixels. It is important to note that care was taken to image the samples using the light microscope with a filter conducive to highlighting the contrast between the epoxy potting compound and the metals of the solder joint, copper pad, and lead foot. This natural contrast captured by the original image helped reduce errors associated with changing the black/white threshold as it provided clear distinctions between metal/non-metal areas during the transformation. An example of this transformation on one of the images can be seen in the following figure.



Figure 4. ImageJ transformation from threshold adjustment.

After the threshold transformation was conducted, the entire periphery of the surface mount solder joint was bounded using the polygon selection tool of the ImageJ software. With the area of interest bounded, an analysis was performed to estimate the volume fraction of the Ag-In solder joint. The bounding performed with the polygon selection tool can be seen below in Figure 5 as the solid line surrounding the entire Ag-In solder joint.



Figure 5. Bounded joint for area fraction analysis.

Following its analysis of the bounded area, the ImageJ software returned the area fraction of non-zero, white pixels representative of joint's empty space; therefore, subtracting this reported area fraction from unity yielded the Ag-In area fraction of interest where material existed within the joint. It was assumed that the area fraction calculated from the ImageJ analysis was equivalent to the true volume fraction of the

entire Ag-In solder joint. This assumption has been demonstrated for opaque, two-dimensional sections and serves as a basis for areal analysis [31].

3.3.2 Validation of Areal Analysis using the Point-Counting Method

The aforementioned areal analysis was carried out on all samples in an effort to reduce the time required to complete volume fraction estimation over more traditional estimation methods like the point-counting technique described in ASTM Specification E562 [32]. In addition, the software offers potentially higher accuracies on the volume fraction estimates because of the significantly higher resolution of the areal analysis; the program calculates the percentage of non-zero (white) pixels within the bounded area to determine the area fraction [33]. The scale of this pixel-by-pixel grid is significantly more refined than any observer would use for an areal or point-counting analysis and the software execution is practically instantaneous when compared to the time necessary to perform an analysis by hand. Although the ImageJ software can be used for the area fraction calculation described above, it is important to ensure that the reported area fractions are within reason when compared to estimations performed using point-counting methods. In an effort to demonstrate agreement between volume fractions estimated using the ImageJ software and the point-counting technique, the representative sample from Figure 4 was analyzed using both methods. Point-counting involves overlaying a grid of the desired size on top of the image to be analyzed. The array of points generated by the intersection of the orthogonal grid lines determines where the cross section will be sampled for material or lack thereof. At each of these point locations the observer assesses

whether the point does or does not lie on the phase of interest, Ag-In material in this case, or whether it lays on the phase boundary. Each point that does lie on the phase of interest is counted as one and each that lays on a phase boundary is counted as one-half. When the entire grid has been assessed, the sum of points scored for material or boundary hits, $\sum P_m$, is divided by the total number of points within the grid area, P_T [31]. The resulting value is referred to as the point fraction, P_P , and is assumed to be equivalent to the linear, L_L , area, A_A , and volume, V_V , fractions of the given field [31]. These relationships can be represented as

$$P_P = \frac{\sum P_m}{P_T} = L_L = A_A = V_V. \quad (1)$$

With respect to the point-counting method, there are a number of recommendations that are suggested for using it in the most accurate and efficient manner [31]. As a general rule of thumb, the sample magnification should be high enough so that the observer may be able to accurately assess the location of the grid points on top of the sample. However, the magnification should be low enough so that, if possible, no more than one grid point falls on a given phase of interest in order to preserve statistical accuracy of the density estimations. For this particular investigation, it was observed that an area of 750 square pixels per grid point satisfied the aforementioned balance of magnification. For the given image in Figure 4, this grid resolution translates to an area of $\sim 5.29 \times 10^{-6} \text{ in}^2$ ($3410 \mu\text{m}^2$) per grid point. The overlay of this grid on the cropped, original image of the Ag-In solder joint from Figure 4 can be seen in Figure 6.

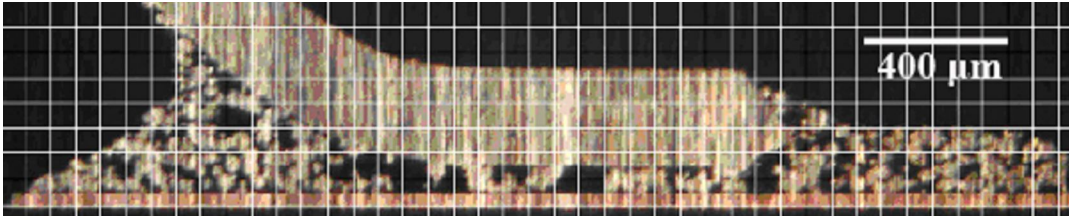


Figure 6. Point-counting method grid overlay.

The ImageJ software was used to size and randomly place a grid over the image. Following placement of the grid, the point-counting method was employed as previously described. From the overlay, it was observed that the field within the solder joint area contained approximately 80 to 85 grid points, depending on the randomized placement of the grid over the image. In order to achieve an average point fraction for the volume fraction estimation of the Ag-In solder joint, five randomly placed grids of previously described spacing were laid over the image and a point fraction was measured in each instance. The point fraction measured for each of these five instances can be viewed below in Table 3.

Table 3. Point and volume fractions of an Ag-In surface mount solder joint.

Instance	$\sum P_m$	P_T	Point fraction, P_P	Volume fraction, V_V
1	59.5	85	0.700	70.0%
2	49.5	85	0.582	58.2%
3	48.5	80	0.606	60.6%
4	57.0	82	0.695	69.5%
5	52.0	80	0.650	65.0%
AVG	53.3	82.4	0.647	64.7%

An ImageJ areal analysis of the same sample using the previously described process yielded an area fraction of 61.5%, which agrees to within 5% of the average area/volume fraction of 64.7% from the point-counting method. With the volume fraction estimation process using the ImageJ software substantiated by the measurements performed with the point-counting method, it is now appropriate to

discuss the volume fraction trends identified within the Ag-In surface mount solder joints with changing particle sizes.

3.3.3 Volume Fraction Trends

The intent of the volume fraction study was to understand the relationship between the sample area fraction and the constituent particle size with the goal of increasing the volume fraction of the Ag-In solder joints so as to improve the mechanical, electrical, and thermal properties of the joints. With respect to the mechanical properties, an increase in volume fraction provides more material to withstand the shear forces developed during passive thermal cycling. In terms of electrical and thermal performance, higher material volume fractions correspond to higher joint cross-sectional areas to carry current and heat, therefore reducing the inherent electrical and thermal resistances of the solder joints.

With respect to persistent liquid phase sintered and TLPS solder joints, there are a multitude of variables that can be altered in order to improve the final material volume fraction. These include particle size, green density, amount of additive metal, time, temperature, heating rate, additive homogeneity, and powder porosity, among others [6]. In the previous list, the term additive refers to the metal responsible for forming the liquid phase during processing while green density refers to the density of the solder joint or compact prior to liquid phase or transient liquid phase sintering. Prior to continuing the discussion on how to improve volume fraction, it is necessary to relate the term to one more commonly used in liquid phase and transient liquid phase sintering literature. Many times density, rather than volume fraction, is used to

describe how solid or compact a TLPS sample is. As described by German [6], density is the mass per unit volume and is often expressed as the fraction of theoretical density, ρ_t . Porosity serves as the complement to fractional density, and when summed together, the two fractions must equal unity [6]. Volume fraction and density can be related to one another through ρ_t . By defining volume fraction as

$$V_v = \frac{V_{metal}}{V_{solder\ jnt}} , \quad (2)$$

and the total mass of a porous solder joint as

$$m_{solder\ jnt} = m_{metal} + m_{voids} = \rho_t V_{metal} + \rho_{air} V_{voids} , \quad (3)$$

a relationship between V_v and the density of the solder joint can be established with some additional simplification. When metals are used for the solder joint, $\rho_t \gg \rho_{air}$, and therefore the $\rho_{air} V_{voids}$ term can be dropped from equation (3). By dividing both sides of the remaining expression by $V_{solder\ jnt}$, one arrives at

$$\rho_{solder\ jnt} = \rho_t V_v . \quad (4)$$

As equation (4) demonstrates, the term density commonly referred to in liquid phase and transient liquid phase sintering literature is directly proportional to the volume fraction through a constant given by the theoretical density of the metals used to form the joint. Subsequently, any reference to an increase in the density of the joint is synonymous with an increase in the volume fraction and vice versa. Prior to discussion of the trends in TLPS works, the concept of densification needs to be defined. It can be qualitatively described as the change in porosity of a compact

following processing normalized to its initial or green porosity [6]. Positive densifications therefore correspond to compacts that have eliminated a given fraction of pores or voids from their structures during liquid phase or transient liquid phase sintering. Densification is often expressed as a percentage because it is a dimensionless value [6].

Although the final density of a TLPS solder joint or compact is sensitive to a large number of material and process related variables, there are only a few that can be easily altered. In particular, the size of the constituent metals is a variable that can be changed by simply mixing TLPS solder pastes using particles of varying sizes. Due to the commercial availability of metal spheres and in order to maintain a manageable experimental scope, the base metal particle size was held constant while additive indium spheres of varying sizes were utilized in preparing a number of Ag-In solder pastes in an effort to improve the volume fraction of the resulting TLPS solder joints. Research in the area of liquid phase and transient liquid phase sintering has demonstrated that smaller particle sizes of the constituent metals have correlated to greater densification and final compact densities [6]. In particular, finer additive particle sizes positively influence the densification and final density of a processed compact for a number of reasons [6]. First, during the liquid phase or transient liquid phase sintering process, the size of the additive particles determines the size of the pores that form at their locations prior to their melting, spreading, and interdiffusion with the base metal particles. Smaller additive particle sizes therefore leave behind smaller pores or voids after they form the liquid constituent of the TLPS material during processing. Second, smaller additive particles sizes lead to higher green

densities that in turn correlate to higher final densities of liquid phase and transient liquid phase sintered compacts. A third reason that finer additive particle sizes aid in densification and improve final compact density is that as the size of the additive particle decreases, the distribution of the additive within the mixture improves, therefore improving homogeneity and subsequently leading to higher densifications due to a uniform distribution of liquid phase within the joint during processing. This trend in increasing final compact densities with decreasing additive particle size is common to liquid phase, transient liquid, and reactive sintering processes for a variety of metallic combinations [28][34][35].

As previously mentioned, the aim of using smaller indium particles was to improve the densification, and subsequently, the volume fraction of the Ag-In solder joints. For this portion of the study, Ag-In pastes were mixed in-house using commercially available metal powders from Alfa Aesar and Advanced Machine and Materials. Silver powder with a characteristic diameter of 50 microns was obtained from Alfa Aesar. Indium powders from Advanced Machine and Materials with characteristic diameters of 45, 25, 10, and 5 microns were purchased as well. These characteristic diameters correspond to mesh sizes -325, -500, -1250, and -2500, respectively. Each indium powder was mixed with the 50 micron silver powder in order to achieve varying ratios of silver particle diameter over indium particle diameter. These ratios, R , in addition to the naming convention assigned to the subsequent mixtures can be seen in Table 4. The no-clean, Indium tack flux NC-SMQ51SC was mixed with these metal powders in order to formulate the pastes for the densification assessment. Prior to mixing, all three constituents were weighed in order to achieve a metal load of 91%

by weight. The composition of the metal load was formulated to be 67 wt. % Ag and 33 wt. % In.

Table 4. Paste formulations for densification study.

Paste	Composition (wt. %)	Metal Load (wt. %)	D_{Ag} (μm)	D_{In} (μm)	$R = D_{Ag}/D_{In}$
P1	67Ag 33In	91	50	45	1
P2	67Ag 33In	91	50	25	2
P3	67Ag 33In	91	50	10	5
P4	67Ag 33In	91	50	5	10

The surface mount components, test boards, processing time, and processing temperature required to appropriately manufacture Ag-In solder joints from these pastes are all described in detail within the experimental procedure section of this work. In addition, however, each solder joint was processed under compression from the weight of the surface mount component. Two distinct gull-wing, surface mount package sizes were used to fabricate samples with each of the pastes for a total of 8 distinct samples; small samples fabricated from pastes P1 through P4 had solder joints subjected to an average lead pressure of ~ 0.23 psi (1585 Pa), while large package samples had solder joints subjected to an average lead pressure of ~ 0.14 psi (965 Pa). These pressures are the direct result of the weight of the packages acting over the surface area of the leads that come in contact with the solder pads during processing. In order to assess any change in densification as a result of indium particle size, four distinct cross sections were collected and averaged for each paste and pressure combination for a total of 32 volume fractions estimated altogether. The results of the densification study are summarized in Figure 7.

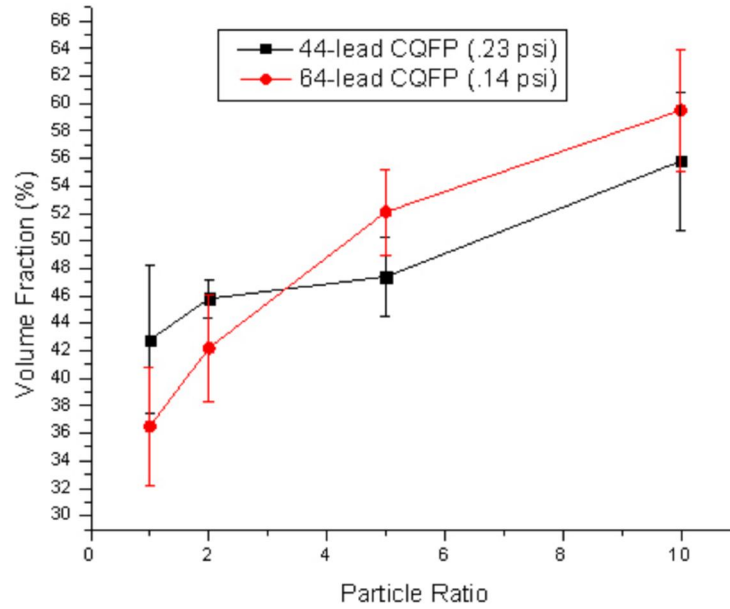


Figure 7. Volume fraction as a function of particle ratio ($R = D_{Ag}/D_{In}$).

As shown in Figure 7, as the indium particle within the Ag-In paste becomes smaller, indicated by an increasing particle ratio, the volume fraction or density of the processed solder joints increases monotonically. Statistically significant differences in volume fraction can be observed between the joints formed with a particle ratio of 10 and 1 when using the 90% confidence intervals provided. It is believed that these volume fraction improvements are a direct result of increasing green density and indium distribution homogeneity within the Ag-In TLPS paste with decreasing indium particle size. The progressive improvement of these characteristics within the unprocessed Ag-In TLPS pastes is evident in Figure 8.

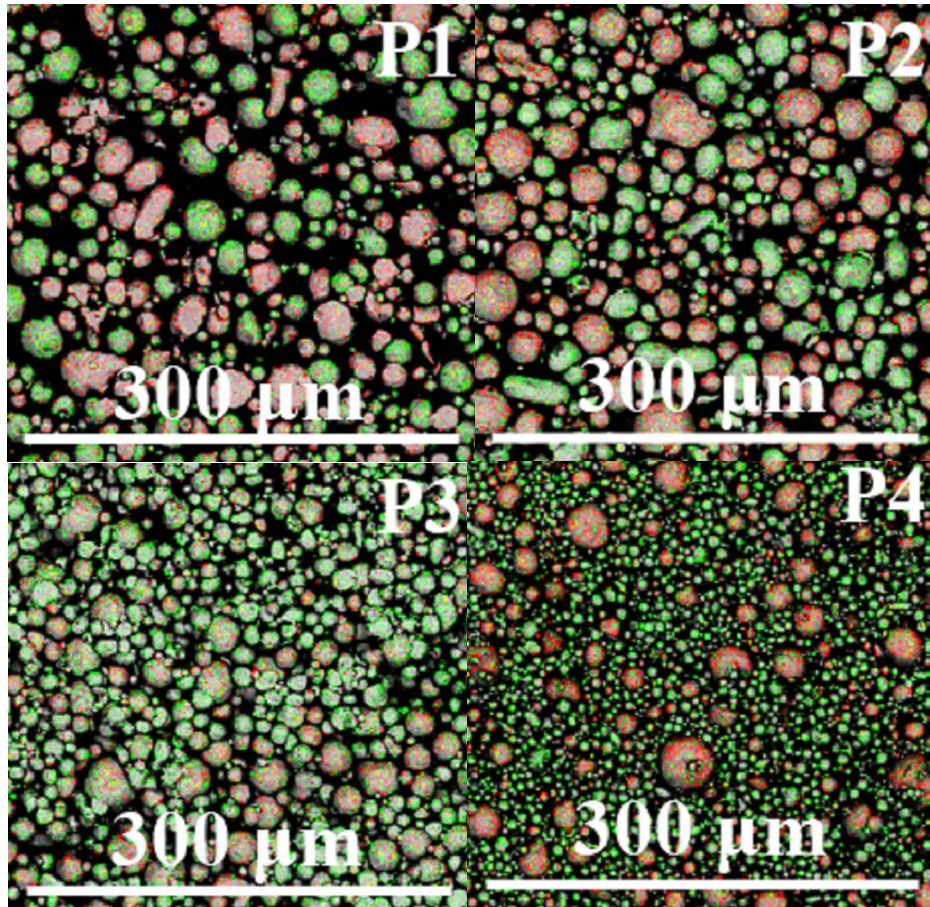


Figure 8. Ag-In TLPS unprocessed paste ESEM/EDS images (Ag in red).

Due to the higher volume fractions observed for the P4 paste samples ($R = 10$, $D_{Ag} = 50 \mu\text{m}$, $D_{In} = 5 \mu\text{m}$), it was decided that samples fabricated for subsequent reliability testing would feature the P4 paste as described in Table 4. It is also worth noting that the wetting behavior exhibited by the liquid phase during TLPS of the joints seemed to increase as indium particles became smaller. This qualitative assessment was observed at the heel and toe areas of the Ag-In TLPS solder joints. A comparison of black/white images of a large package P1 and P4 Ag-In solder joint demonstrates this trend. The volume fractions of the two formulations are clearly different in addition to the fact that the P1 paste has largely maintained its as-deposited shape while the P4

paste has formed a heel and toe on the lead common to commercial surface mount solder attaches.

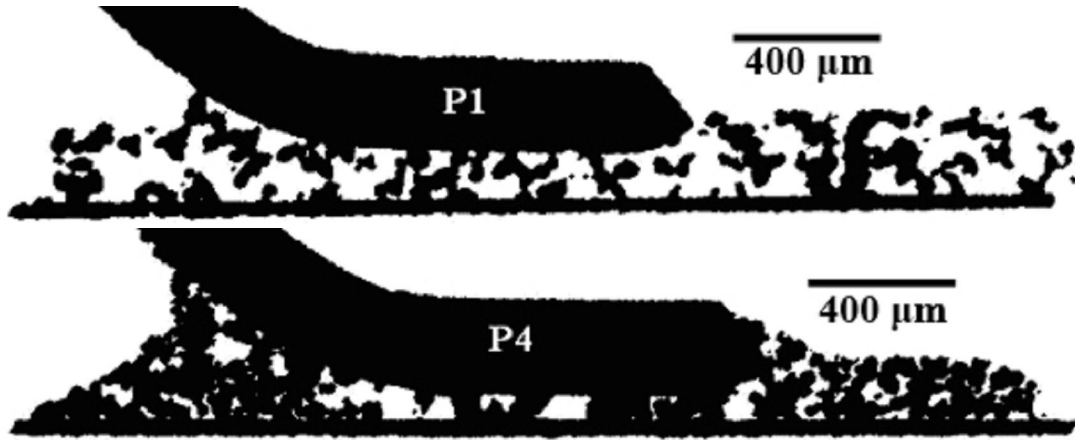


Figure 9. Wetting comparison of P1 and P4 pastes under large package leads.

Chapter 4: Experimental Procedure

This chapter describes the materials, methods, and testing procedures necessary for executing the comparative reliability study between the three solder materials:

SAC305, eutectic Au-Sn, and Ag-In TLPS. Materials and manufacturing considerations regarding the test assembly are discussed in depth along with the selection and implementation of passive thermal cycling for environmental stressing of the test assemblies.

4.1 Test Vehicle Materials

In order to perform the comparative reliability study mentioned earlier in this work, a sufficient number of samples of each of the three solder attach materials was required for testing. SAC305 and eutectic Au-Sn were fabricated using best-known manufacturing methods collected from product literature. Ag-In TLPS samples were fabricated using methods developed as part of this thesis. All sample fabrication was performed in-house using the necessary materials in conjunction with the appropriate, available equipment at the University of Maryland, College Park. The test vehicle used during this investigation was composed of a polyimide laminate circuit board in conjunction with ceramic, gull-wing, surface mount components. Materials used during sample fabrication of the SMT samples included the following: edge-card circuit boards, ceramic quadflat pack (CQFP) components, solder pastes (SAC305, eutectic Au-Sn, and Ag-In TLPS), and stencil foils.

4.1.1 Edge-card Circuit Boards

For this investigation a polyimide, edge-card test board was designed in-house and fabricated by an outside supplier, K&F Electronics, Inc. Polyimide was selected as the laminate of choice due to its relatively high T_g (~250°C) with respect to other popular organic laminates such as FR-4 ($T_g \sim 135\text{-}175^\circ\text{C}$) or BT resin ($T_g > 175^\circ\text{C}$). A material possessing a high T_g was selected for the following two reasons: first, the higher T_g ensured that the breakdown/decomposition temperature of the organic laminate was above 250°C, and second, board expansion with respect to temperature would remain a linear phenomenon during the thermal cycling of the reliability study, as it would not surpass this 250°C T_g limit. This simplifies the strain estimations within the solder joints. Ceramic boards processed through low temperature cofiring (LTCC) methods were also considered, but design constraints and their brittle nature ruled them out. In summary, the robustness of organic laminates, the additional survivability that comes with a high T_g , and the constant CTE during the selected thermal cycling were all considerations that led to polyimide as the selected test board material. This mirrors the fact that most applications in the 125 to 200°C range routinely use polyimide boards.

Design of the polyimide test boards was conducted with the layout editor, EAGLE 4.16. This CAD program allows users to designate groups of electrically connected nodes within the design, referred to as “nets,” and connect them. Manual routing of the electrical nets was conducted in the study. Each polyimide test board was designed to accommodate a total of 4 CQFP components. The description of these

ceramic package geometries will follow the discussion of the test boards. For simplicity, of these 4 CQFP packages per board, 2 44-lead CQFPs were designated as “small” and the remaining 2 64-lead CQFPs were designated as “large.” These simple names refer to the overall package footprint, which directly translates to the strains imposed on the solder joints connecting them to the test boards. A visual comparison of the package sizes can be seen in Figure 10 and Figure 11 below.

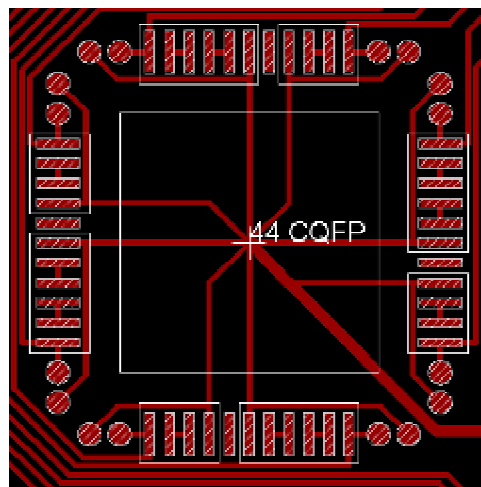


Figure 10. Small CQFP footprint.

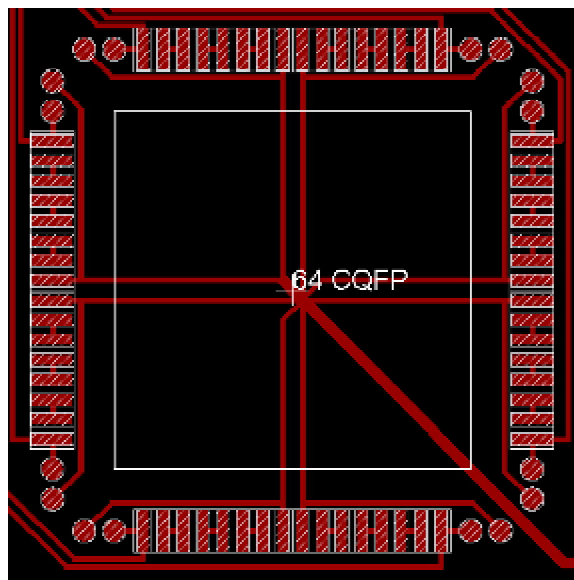


Figure 11. Large CQFP footprint.

In order to facilitate installation, removal, and repair of the test board assemblies during the reliability study, the polyimide test boards were designed to interface with selected edge card connectors. By implementing an edge card connection to the test boards, one allows for the electrical connection of the board to the necessary monitoring equipment without requiring a permanent solder connection. The edge card connection allows for the easy removal and reinstallation of the polyimide test boards during reliability testing if and when inspection of the boards is required. A description of the materials and geometries of the edge card connectors will be given in the subsequent equipment section of this work. A close-up CAD image of the male, edge-card feature of the polyimide test boards is displayed in Figure 12.

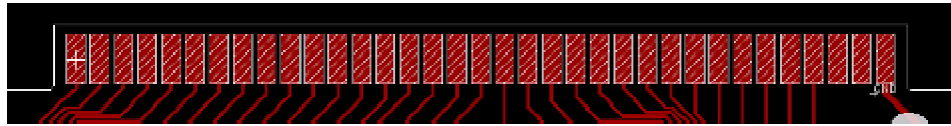


Figure 12. Polyimide test board edge-card feature.

The test board had an overall footprint of 4" (102 mm) by 3.2" (82 mm). For the given version of the EAGLE 4.16 software, this was the maximum footprint permissible by the program. Although a smaller board was possible with the given space and trace requirements, the board was intentionally oversized in order to facilitate handling during the sample fabrication and testing steps. A board thickness of 59 mil (1.5 mm) was selected in order to ensure robustness of the boards during handling in addition to proper interfacing with the selected edge card connectors.

Due to the simplicity of the board design, a single layer of copper was required to electrically connect all of the CQFP packages to the edge card fingers. The thickness

of this single layer of copper was specified as 1-ounce per square foot, which translates to 1.4 mil (35 μm). All signal traces on the test boards, excluding the ground trace, were designed as 10 mil (255 μm) trace and 10 mil space. The ground trace, which can be identified as the trace running along the right side of the board design in Figure 13, was specified as 25 mil (635 μm) trace width in order to reduce the total loop resistance of each of the electrical chains. Trace and surface pad arrangement on the test boards was performed in order to create an electrical “daisy-chain” pattern that, when assembled with the CQFP components, would form continuous electrical chains. A total of 8 distinct electrical chains were specified for each CQFP, resulting in a total of 32 distinct chains per test board. Details regarding the wiring within the CQFP components will be given in the following section. The surface mount pads of the polyimide board were finished with 3 to 8 micro inches (0.076 to .2 μm) of immersion gold over 100 to 200 micro inches (2.54 to 5.08 μm) of electroless nickel (ENIG); edge connector pads were finished with 30 micro inches (.76 μm) of gold over 500 micro inches (12.7 μm) of nickel.

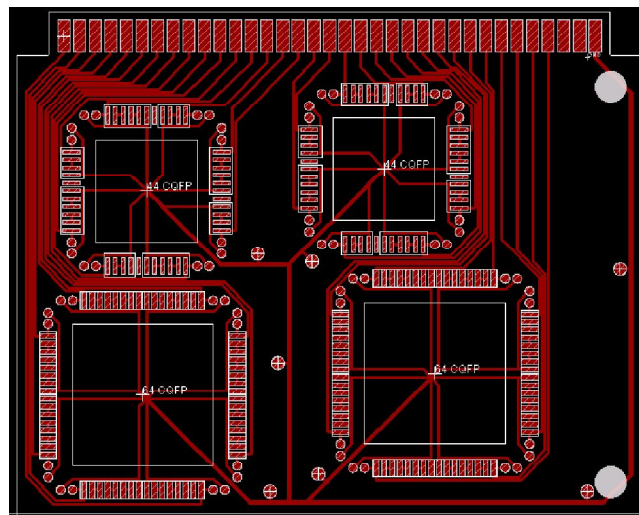


Figure 13. Polyimide test board design.

4.1.2 Ceramic Quadflat Pack Components

Selection of the type of surface mount components was as critical to this study as the selection of the test boards. Elevated temperatures during fabrication and thermal cycling eliminated epoxy-based SMT components from consideration due to their low glass transition temperatures. For example, a popular molding compound used in many dummy components, Sumitomo 6300H, features a glass transition temperature of $\sim 165^{\circ}\text{C}$ [36] which falls within the extremes of the planned temperature cycling of this investigation. Although suitable for lead-free manufacturing and subsequent standard temperature cycling, this type of material was unlikely to survive the elevated reflow temperatures required for eutectic Au-Sn assembly, the extended processing time required for the Ag-In TLPS assembly, or the elevated temperature cycling. In light of the need to avoid common plastic encapsulated surface mount packages for the test assemblies, ceramic body components were researched as an alternative. Ceramic surface mount components were purchased from Practical Components as flat “CQFP” packages. In contrast to typical plastic encapsulated quadflat packages, these ceramic packages were only available with flat leads connected to a common tie-bar around the perimeter of the package. Two component sizes were selected for the study: “large”, 64-lead CQFPs and “small,” 44-lead CQFPs. The desired ceramic packages were purchased as inactive, dummy components with internal daisy-chain patterns designed to mate with those on the polyimide test boards to form continuous electrical chains. The package daisy chains, when connected to those on the polyimide test boards, were designed to create 8

electrically distinct chains within each package. The intent of each of these electrical chains was to allow for monitoring of their respective corner solder joints, as these joints are expected to be the first to fail during temperature cycling. Schematics of the particular daisy-chain wiring schemes within the “large” and “small” CQFPs can be seen in Figure 14 and Figure 15, respectively. The bold, curved lines between adjacent leads denote an internal electrical connection.

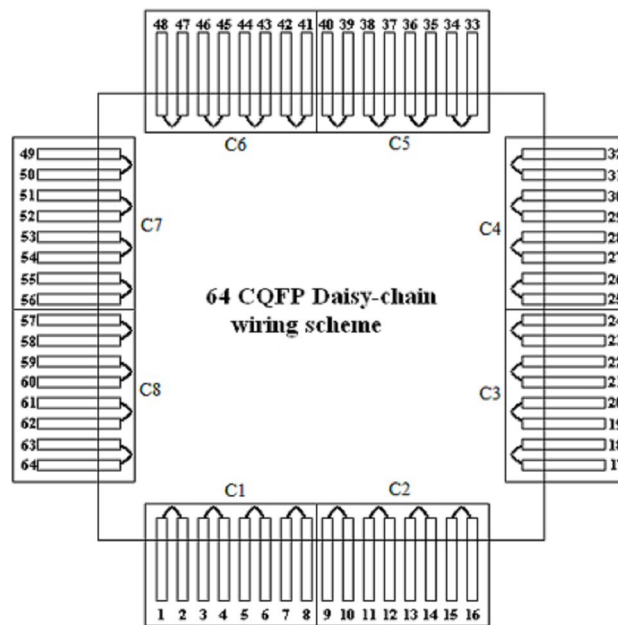


Figure 14. 64-lead CQFP daisy chain wiring scheme.

It is important to note that due to the odd number of leads per side on the 44-lead CQFP, not every lead could be utilized in creating a pattern capable of forming 8 electrical chains when joined to the test board. In the case of the 64-lead CQFP above, the even number of leads per side allows for all to be used in the continuous electrical chain. Although failure at the corner joints was expected during temperature cycling, it is worth mentioning that the daisy-chain patterns specified for the ceramic packages were designed in order to detect joint failure at any of the solder

joints within the package. The only caveat to this was that a single interior lead on each side of the 44-lead CQFP could not be monitored.

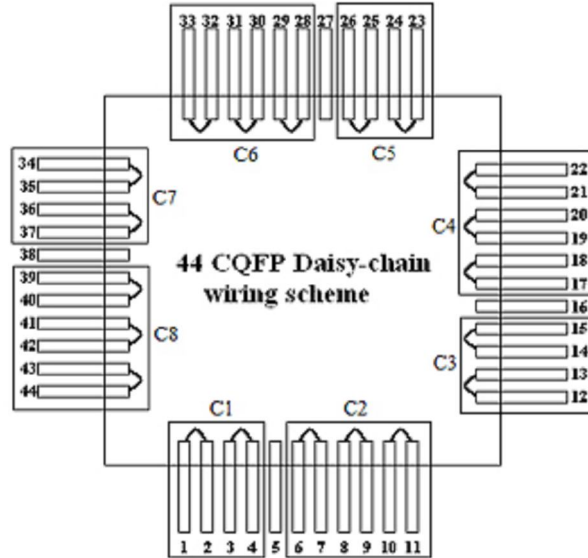


Figure 15. 44-lead CQFP daisy-chain wiring scheme.

In order to singulate and bend each of the flat leads into gull wing geometries common in many surface mount packages, a gull wing bending tool was necessary. A custom designed bending and cutting tool from Excelta Corporation made it possible to form and trim the flat leads of the CQFP packages into the desired gull-wing geometry displayed in Figure 16. These dimensions are important because they, in conjunction with the thickness and width of the leads, determine the lead compliancy that affects the strain energy density within the joints during passive thermal cycling. In both “large” and “small” CQFP packages, the distance between adjacent leads (lead pitch) was 50 mil (1.27 mm). The decision to use parts with such a large lead pitch was influenced heavily by manufacturability concerns; when the pitch gets smaller, assembly limitations as well as adjacent pad shorts become significant hurdles to constructing experimental samples.

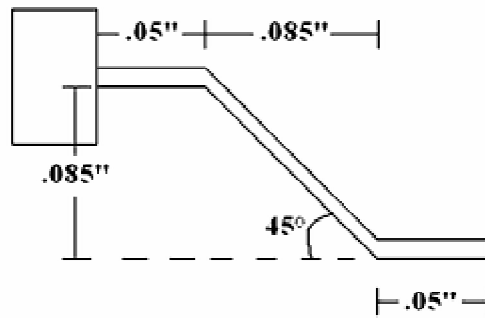


Figure 16. Desired CQFP Gull-wing geometry (not to scale).

With respect to the materials that composed the CQFP components, the ceramic in the packages was Kyocera A-440 alumina, while the leads were Alloy 42. The leads of all CQFP packages were finished with 60 micro inches (1.52 microns) of gold over 100 micro inches (2.54 microns) of nickel.

4.1.3 Combined Test Vehicle

When assembled, the resulting global coefficient of thermal expansion (CTE) mismatch between the polyimide board and ceramic components ($\alpha_{\text{polyimide}} - \alpha_{\text{alumina}}$) was approximately 5 ppm/°C. This disparity in global expansion between the two materials is responsible for the strains imposed on the solder joints during passive thermal cycling. The design of the test vehicle allowed for the selection of ideal board, assembly, and component materials. The resulting metallization stack-up prior to processing of the test vehicle assemblies is summarized in Figure 17.

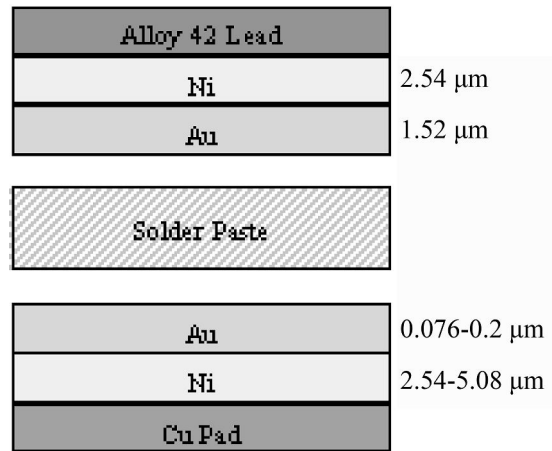


Figure 17. Test vehicle metallization stack-up.

4.1.4 Solder Pastes

The first of the three solder pastes to be discussed is SAC305. The SAC305 solder paste used during this investigation was Kester's EnviroMark 907. This lead-free paste formulation featured a no-clean chemistry, meaning that post-reflow steps involving the cleaning of flux residues were not required during the fabrication sequence. Notable characteristics of the Kester SAC305 paste include its excellent solderability to ENIG surface metallizations, successful stencil printing down to component pitches of 16-20 mil (0.4-0.5 mm), as well as the ability to be processed in an air or nitrogen atmosphere during reflow [37]. With respect to the metal to flux ratio within the SAC paste, a typical metal load of 88.5% by weight was used. Metal loads up to ~90% by weight are typical of pastes intended for stencil printing, while those up to ~88% by weight are intended for dispense processes [38]. The size of the metal particles within the SAC305 paste were type 3 (-325/+500 mesh). Particles classified as type 3 mesh range in diameter from 25-45 microns (~1-2 mil). The recommended reflow profile of the Kester SAC305 paste was provided in the data

sheet accompanying the product. Further discussion of the recommended reflow parameters for this paste will follow in a discussion of the Omega furnace.

The second of the three solder pastes investigated was eutectic Au-Sn. This Au-Sn solder paste was acquired from Indium Corporation of America, where it is classified as Indium Alloy 182. As indicated by the “eutectic” labeling, the metal load of the paste is composed of 80 wt. % Au and 20 wt. % Sn. The metal particles within the paste were again type 3 (-325/+500 mesh). The metal load of the eutectic Au-Sn solder paste was 91% by weight. The paste was formulated by mixing the previously described metal load with Indium flux NC-SMQ51SC. This particular flux is characterized by a no-clean formulation and wide reflow processing window that allows it to be used in conjunction with the high melting temperature eutectic Au-Sn alloy [39]. The recommended reflow parameters [40] of the eutectic Au-Sn solder paste will be discussed in a subsequent section.

The last of the solder pastes used for sample fabrication for the reliability investigation was the Ag-In TLPS paste. This paste was mixed in-house using indium and silver powders along with a high-temperature flux formulation. Earlier experimentation with the effect of particle size on densification provided guidance regarding the size of silver and indium particles that should be used in the final embodiment during the reliability testing portion of the investigation. Silver powder with a characteristic diameter of 50 microns was obtained from Alfa Aesar. Indium powder from Advanced Machine and Materials with a characteristic diameter of 5 microns was purchased as well. The no-clean, Indium tack flux NC-SMQ51SC was

mixed with these two metal powders in order to formulate the final paste for reliability testing. Prior to mixing, all three constituents were measured in order to achieve a metal load of 91% by weight. The composition of the metal load was formulated to be 67 wt. % Ag and 33 wt. % In. As described earlier, this composition provides a melting point shift during processing that results in a final melting temperature of 540°C.

4.1.5 Stencil Foils

In order to manufacture test assemblies using the test boards, CQFPs, and solder pastes previously described, a method of depositing the solder paste onto the boards was required. In SMT manufacture, paste deposition is one of the first steps performed in the fabrication sequence, prior to component placement and reflow processing. There are a number of ways to deposit solder paste in a controlled manner, some of which include screen printing, stencil printing, as well as dispensing. In this investigation, stencil printing was selected as the method of deposition. This is a common method of SMT assembly which provides improved deposition control over the older screen printing methods. As was the case with the polyimide test boards, the design of the stencil foil was performed in EAGLE 4.16. A CAD image of the stencil foil design can be seen in Figure 18.

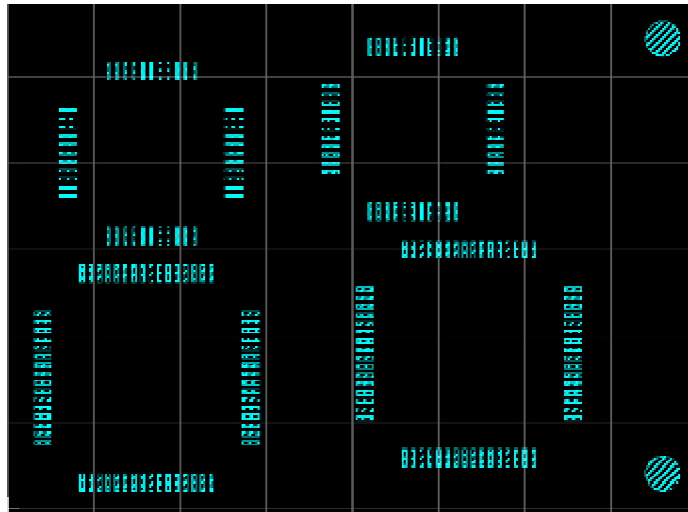


Figure 18. Stencil foil design in EAGLE 4.16.

Those areas in hatched texture represent the apertures within the stencil foil that allow paste to be printed onto the test board solder pads when properly aligned. In order to ensure proper stencil alignment, two circular stencil apertures 200 mil (5.08 mm) in diameter were placed on the far right side of the stencil. Corresponding fiducials placed on the test board, as seen in Figure 13, were used to help properly align the stencil prior to printing. The stencil foil designs were forwarded to Photostencil for fabrication by laser cutting on stainless steel foils. Specification of the stencil apertures ensured that the aspect and area ratios were above the commonly prescribed minimum values [41], 1.5 and .66, respectively. Apertures of the 64-lead CQFPs featured aspect ratios of 2.85 and area ratios of 1.156 while those of the 44-lead CQFPs featured aspect ratios of 1.85 and area ratios of .804. In order to fabricate the SAC305 and eutectic Au-Sn test assemblies, an 8-mil (200 μm) thick stencil foil with the above aperture design was utilized. Initial attempts to fabricate Ag-In TLPS samples using this stencil thickness led to issues regarding unnecessarily large solder volumes. Subsequent Ag-In TLPS samples were fabricated with a foil thickness of 6

mil (150 μm), which produced more consistent test assemblies with the solder material.

4.2 Test Vehicle Fabrication

Fabrication of the board and CQFP assemblies for each of the component attaches was performed by stencil printing the paste, placing the CQFPs, and subjecting the assembly to a specified profile within the Omega LMF-3550 infrared (IR) furnace. Recommended profiles for the SAC305 and eutectic Au-Sn solder pastes were gathered from the available data sheets [37][40] while the processing profile for the Ag-In TLPS paste was designed using an empirical model capable of predicting the remaining weight % indium based on a number of factors that include holding time, ramp rate, processing temperature, among others [8].

4.2.1 Stencil Printing

Stencil printing of the SAC305, eutectic Au-Sn, and Ag-In TLPS solder pastes occurred by way of a manual, fixture-assisted method. A hinged fixture to hold the stencil foil and polyimide test board was constructed and implemented during this portion of the fabrication sequence. Hinging of the stencil foil provided a fixed stencil edge that helped secure the foil during the printing process as well as facilitated the controlled removal of the foil following paste printing. This fixture can be seen in Figure 19. All boards were cleaned with isopropyl alcohol in order to remove any contaminants prior to the stencil printing process.

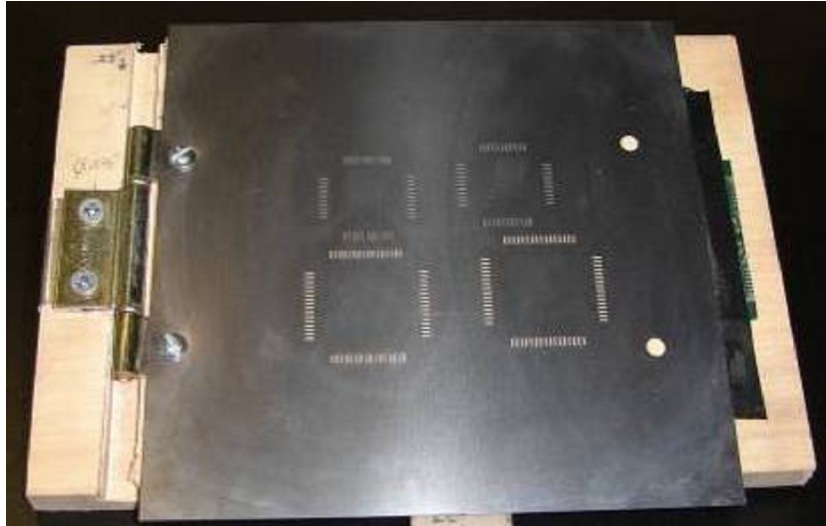


Figure 19. Stencil printing fixture.

Prior to printing, alignment of the stencil foil to the test board was performed by using the circular stencil apertures and corresponding test board fiducials mentioned earlier. Once alignment was achieved, a paste roll approximately 200 mil (5.08 mm) in diameter was deposited along one side of the stencil foil. Using an electroformed nickel squeegee blade, this paste roll was swept across the stencil in order to deposit the paste within the open apertures of the foil design. The direction of the paste print with respect to the design of the stencil foil can be viewed in Figure 20.

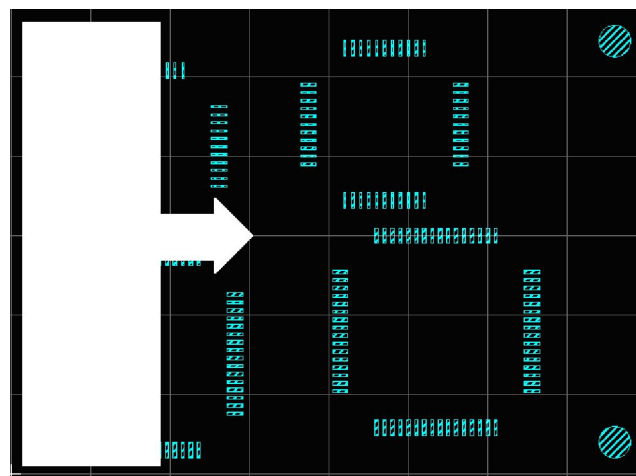


Figure 20. Stencil printing orientation and direction.

Following a successful single pass of the squeegee blade and inspection of the filled aperture holes, the stencil foil was carefully removed from the surface of the test board by opening the hinged fixture. It is important to note that each pass of the squeegee was terminated before arriving at the circular stencil apertures to avoid depositing paste directly on the soldermask of the test boards. With the paste successfully deposited on the surface mount pads of the polyimide test boards, the next step performed in the fabrication sequence was that of CQFP component placement.

4.2.2 CQFP Placement

Placement of the CQFP packages was also performed by way of a manual, fixture-assisted method. Prior to placement, all CQFP components were checked for coplanarity and then cleaned in a series of solvents: acetone, then methanol, and lastly, isopropyl alcohol. The fixture used to assist the manual placement of these CQFPs was designed to house a vacuum pick tool with the freedom to move in the vertical direction. The fixture was intended to facilitate the alignment and placement process by providing a reliable way in which the components could be suspended above the paste printed test boards during the alignment process. An image of this fixture with the vacuum pick tool can be observed in Figure 21.

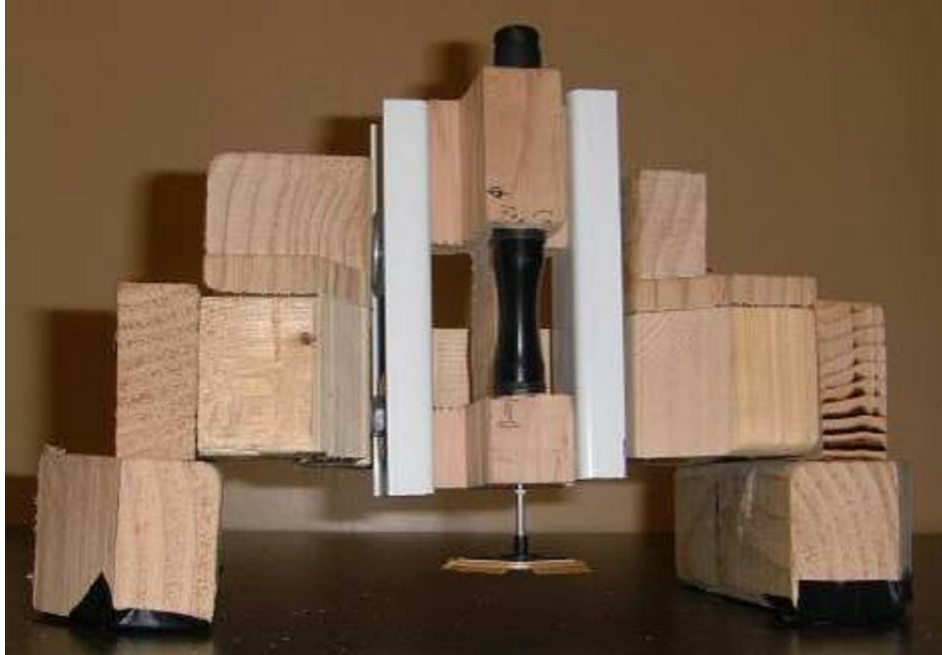


Figure 21. CQFP component placement fixture.

Using the component placement fixture, parts were picked up, positioned over top of their location on the paste printed test board, lowered to an appropriate height for alignment, and finally placed onto the board. Because of the coarse pitch of the surface mount packages, alignment could be performed visually by aligning two perpendicular sides of a package and checking for alignment of the remaining two. The design of the component placement fixture ensured that visual alignment could be performed by looking down onto the board: the ideal perspective for the task. The last of the fabrication steps, reflow/temperature processing, followed directly after the completed placement of all components on the test board.

4.2.3 Reflow / Temperature Processing

Final processing of the assembled test vehicles required reflow temperature processing within the Omega LMF-3550 infrared (IR) furnace. The specifications of

the machine state that it is capable of reaching temperatures ranging from 50 to 1100°C at a ramp rate of 0 to 40°C/min [42]. In order to achieve a more acceptable ramp rate for reflowing electronic assemblies (on the order of 60°C/min) and to ensure that the solder paste within the test assembly was experiencing the desired reflow profiles, temperature testing of the chamber was required. Earlier work with the Omega furnace had demonstrated that the optimum sample placement within the machine to achieve maximum ramp rate was approximately half of its vertical height. All temperature tests and sample processing occurred at this height by way of a lightweight, aluminum stand fabricated for use within the furnace.

Due to the internal size restrictions of the Omega furnace, only two fully populated test assemblies could be processed at the same time. Because of this constraint, all temperature testing was performed on a dummy set of two polyimide test boards, without solder paste, and fully populated with CQFPs. K-type thermocouples were evenly distributed among the two test boards and positioned underneath the gull wing leads of the CQFPs in order to mimic pads of solder paste subjected to the selected temperature profile. The arrangement of the thermocouples with respect to the boards and CQFP components can be seen in Figure 22. It is important to note that thermocouples 1 through 4 were arranged as a primary diagonal around which thermocouples 5 through 8 were used to collect temperature data on other geographical extremes of the test board arrangement.

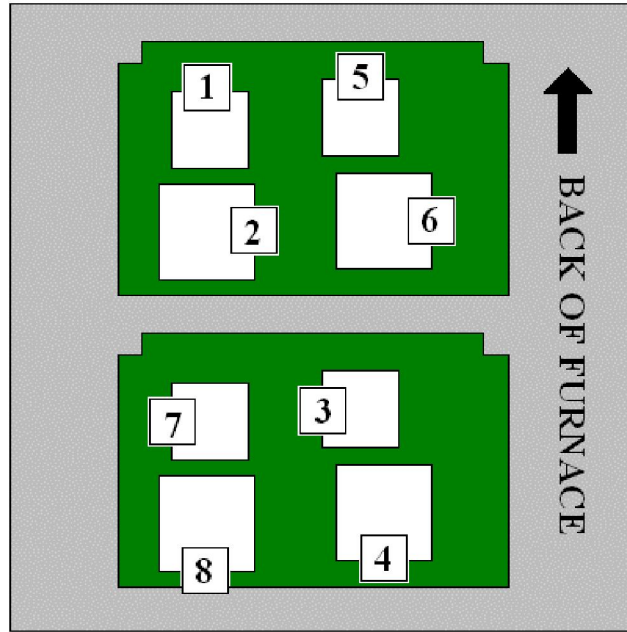


Figure 22. Furnace temperature testing thermocouple arrangement.

The Agilent 34970A Data Acquisition Switch Unit was used to collect temperature data from these prearranged K-type thermocouples. Each thermocouple was wired into its respective channel on the 34901A 20-channel multiplexer module that interfaced directly with the 34970A data logger. Data was gathered at a rate of 1 reading every 2 seconds. Further description of the data logger and switch units will be provided later during a discussion of the monitoring performed for reliability testing.

In order to create a distinct profile for each of the pastes used for this study, active monitoring of the temperature data as received by the 34970A data-logging unit was required. When necessary, adjustment to the typical furnace procedures were performed in order to achieve temperature profiles as recommended by the paste manufacturers [37][40]. Regarding these adjustments, pre-heating of the furnace to a given steady-state temperature was used to increase the ramp rate of processing

performed within the furnace. Because the furnace was not equipped with any cooling technologies, removal of the test assemblies to the ambient was performed to cool them at an acceptable rate. Alternative cooling schemes were considered and attempted, but heterogeneous cooling rates in addition to significantly longer cooling times thought to negatively influence microstructure of the as-built joints were observed during their implementation. To summarize, pre-heating and sample removal was implemented in all three reflow/temperature processing profiles in order to achieve the desired forms.

4.2.3.1 SAC305 Reflow Profile

Development of the SAC305 reflow profile was based upon that recommended within the EM907 product data sheet [37]. As this profile in Figure 23 shows, the manufacturer recommended a ramp of less than $2.5^{\circ}\text{C}/\text{sec}$ to a peak temperature between 235 and 255°C approximately 3.5 minutes (210 seconds) into processing. The total time above reflow was recommended as 60-75 seconds and no more 90 seconds altogether. Although a cool down rate was not prescribed within the SAC305 documentation, a recommendation of less than $4^{\circ}\text{C}/\text{sec}$ was found within eutectic Au-Sn documentation and used for all solder materials.

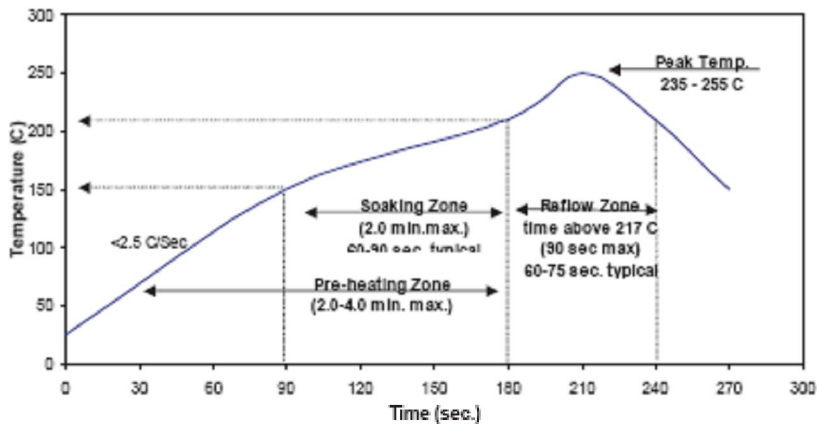


Figure 23. Manufacturer's recommended SAC305 reflow profile.

In order to achieve the SAC305 reflow profile prescribed above, the Omega furnace was preheated to 275°C and allowed to stabilize to ensure temperature uniformity. The aluminum stand populated with the test assemblies was then introduced to the furnace which was set to ramp at 40°C/min to a temperature well above the original set point of 275°C. Following ~212 seconds within the furnace, the aluminum stand still populated with the test assemblies was removed to the ambient temperature of ~24°C. The resulting temperature data from the aforementioned series of processing steps can be viewed in Figure 24. This trace is the averaged data from the collection of eight K-type thermocouples attached to the test assemblies. Although not presented individually for the sake of simplicity, all temperature-time data collected from each of the thermocouples was found to be within the recommended specifications cited earlier. As the plot below shows, the average ramp rate of the measured SAC305 reflow was approximately 0.9°C/sec while the cool down rate was approximately 2.5°C/sec. An average peak temperature of 245°C was reached during a time above reflow of 45 seconds. During the practical application of the profile, the target time above reflow of 60 seconds had to be shortened to 45 seconds due to

considerations regarding furnace operation. In order to ensure the maximum temperature of the solder joints did not exceed the recommended upper bound of 255°C, the time above reflow needed to be cut back 15 seconds from the prescribed one minute because ramp rate was in effect constant during the process. From room to peak temperature, the process took approximately 212 seconds.

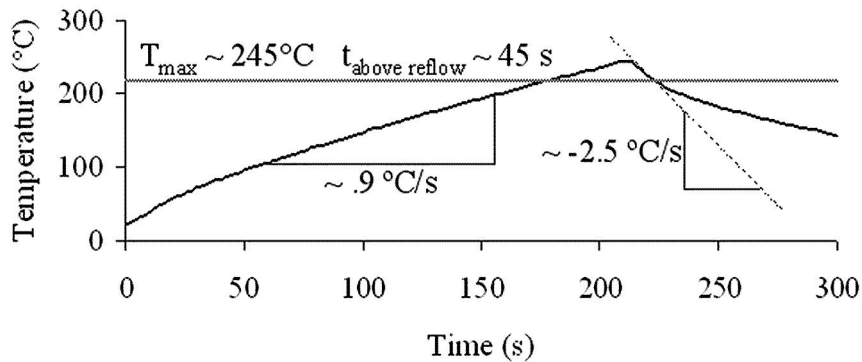


Figure 24. SAC305 reflow profile as measured within Omega furnace.

4.2.3.2 Eutectic Au-Sn Reflow

With respect to the eutectic Au-Sn reflow profile, recommendations regarding the process were gathered from the related data sheet [40]. A linear ramp rate of 1-2°C/sec was recommended to a maximum temperature of 310-330°C. Time above liquidus was prescribed as ranging from 45 to 90 seconds above 280°C. During cool down, a rate of no more than 4°C/sec was recommended, as too slow of a cool down would prematurely coarsen the microstructure of the solder joint and too fast of a cool down would overstress the test assembly by way of thermal shock. A representation of these recommendations as taken from [40] is shown in Figure 25.

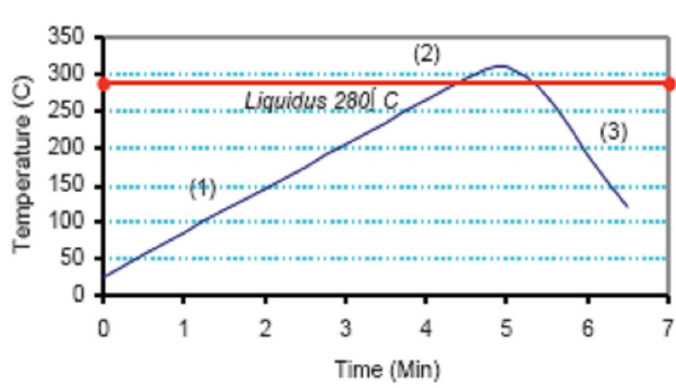


Figure 25. Manufacturer's recommended eutectic Au-Sn reflow profile.

Practical implementation of the eutectic Au-Sn reflow profile occurred by preheating the Omega furnace to 300°C and allowing temperature stabilization to occur.

Following sample introduction into the furnace, the machine's maximum ramp rate of 40°C/min was programmed to reach a temperature well above the original set point of 300°C. After ~274 seconds from introduction to the furnace, the test assemblies were removed to the ambient temperature of ~24°C. The resulting temperature data from the eight thermocouples monitored during the process is shown below in Figure 26. Again, the plot in the figure below is an average of the aforementioned thermocouple data. As it shows, an average ramp rate of 1.05°C/sec was achieved during reflow while the test assemblies experienced a cool down rate of 3.25°C/sec. The average maximum temperature of the eutectic Au-Sn solder joints was 315°C while time above liquidus was 55 seconds. It is clear from this description that all parameter ranges recommended by the product documentation were followed in the reflow profile developed for use with the Omega furnace.

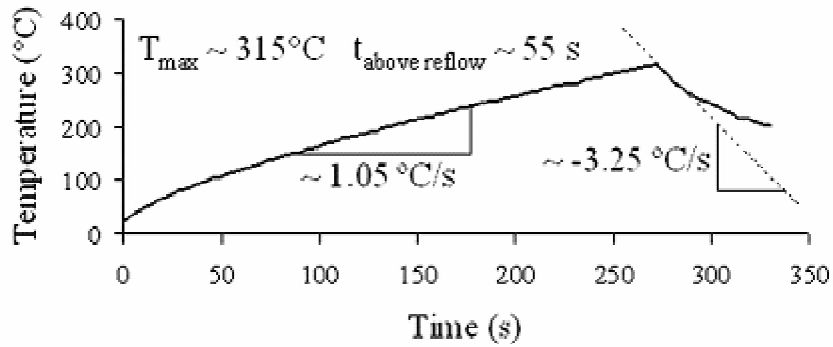


Figure 26. Eutectic Au-Sn profile as measured within Omega furnace.

A summary of the furnace settings required to achieve the SAC305 and eutectic Au-Sn reflow profiles can be viewed in Table 5. It is important to note that the final set point of both reflow processes was selected in order to be an unachievable value for the furnace to attain during the time the samples were inside of the furnace. This ensured that the furnace was continually heating while the samples were inside, effectively supplementing the sample ramp rate due to the preheat temperature. This type of scheme was critical in attaining average ramp rates of approximately 60°C/min (1°C/sec) necessary for proper solder paste reflow.

Table 5. Omega furnace settings and procedures for proper reflow of SAC305 and eutectic Au-Sn.

Solder	Preheat Set point	Ramp Rate	Final Set point	Overall time in furnace
SAC305	275°C	40°C/min	400°C	212 seconds
Au-Sn	300°C	40°C/min	400°C	274 seconds

4.2.3.3 Ag-In TLPS Temperature Processing

The final of the three pastes manufactured for this investigation required a far more elaborate effort in order to create a suitable profile for temperature processing. As previously discussed, the Ag-In TLPS paste used to fabricate the reliability testing

samples was characterized by a composition of 67 wt. % Ag and 33 wt. % In. This paste composition in conjunction with a number of factors including silver particle size, processing ramp rate, processing temperature, and hold time was shown to influence the remaining wt. % In of the resulting solder joints [8]. Unlike traditionally reflowed component attaches, the TLPS paste does not require temperatures during processing to exceed its overall melting temperature for solidification to occur. The temperature of the TLPS paste during processing was specified in order to melt the In and ensure that all In-rich phases remain liquid until diffusion of In has occurred to the point where a new, high melting temperature phase was formed from the Ag-In mixture. Based on the given silver particle size, paste composition, and assuming a processing ramp rate of $\sim 1^\circ\text{C}/\text{sec}$, it was determined that processing at 250°C for a duration of 90 minutes would be required to eliminate all low melting temperature phases. 250°C was selected as the processing temperature because it was low enough to be compatible with surface mount processing but high enough to permit Ag-In reaction in a reasonable amount of time. In this state all In-rich phases would have been diffused into the Ag matrix, thus achieving the melting point shift and a new melting temperature of 540°C [30].

It is important to note that temperatures during processing remain significantly lower than the melting point of the Ag particles, thus rendering this a liquid-assisted sintering process. The melting of the low melting point constituents within the TLPS paste provides two favorable characteristics over traditional sintering: one, the rates of diffusion between liquid and solid during TLPS are much higher than those between solid and solid, and two, the liquid within the mixture provides wetting

between Ag particles as well as between Ag particles and the surfaces to be joined. Details regarding the phase transformations and stages of diffusion of this TLPS material during processing are available in the prior work [8].

As was the case with the SAC305 and eutectic Au-Sn reflow profiles, the temperature processing profile developed for the Ag-In TLPS material consisted of a preheat step and ended in removal of the test assemblies to ambient for cooling. In contrast to the profile descriptions from earlier, additional effort on the part of the furnace operator was required in achieving the desired profile that involved a 1°C/sec ramp to 250°C, followed by a hold of 90 minutes prior to removal of the test assemblies from the furnace. Much of this effort was focused on eliminating the significant temperature overshoot of the temperature controller when ramping to 250°C. Prior to introduction of the Ag-In TLPS test assemblies, the furnace was stabilized at 275°C. Immediately following insertion of the samples into the furnace the set point was changed to 400°C at a programmed ramp rate of 40°C/min. As the sample thermocouples approached 235°C, the furnace set point was reprogrammed to 250°C. This reprogramming was performed to ensure that the furnace would maintain the desired processing temperature during the extended hold of 90 minutes. Although the chamber controller performs poorly with respect to temperature overshoots resulting from long ramp up times, it was shown to be very reliable at maintaining a preprogrammed steady-state temperature. After the samples reached the appropriate 250°C processing temperature, a sequence of partial openings and closings of the furnace door was performed to exhaust the overheat produced by the furnace during the ramp up. The furnace door was consistently opened to a height of ~1.5" (38 mm)

from a fully closed position and returned to a fully closed position during the partial opening and closing procedure. The timing associated with the open/close procedure can be viewed in Table 6. It is important to note that following this ~19 minute period, the furnace was completely stabilized at 250°C at which time the furnace door remained closed for the remainder of the 90 minute processing profile.

Table 6. Ag-In TLPS processing open/close furnace door sequence.

	Time (MIN:SEC)		Time (MIN:SEC)
Furnace set to 400°C	0:00	Open 6	8:00
Furnace reset to 250°C	3:00	Close 6	8:30
Open 1	3:19	Open 7	9:00
Close 1	5:05	Close 7	9:30
Open 2	5:25	Open 8	10:00
Close 2	5:40	Close 8	10:30
Open 3	6:00	Open 9	12:00
Close 3	6:15	Close 9	12:30
Open 4	6:35	Open 10	14:00
Close 4	7:05	Close 10	14:30
Open 5	7:20	Open 11	18:30
Close 5	7:40	Close 11	18:45

The resulting profile generated by the previous operations can be viewed in Figure 27. As the temperature processing profile demonstrates, an average ramp rate of 1°C/sec was achieved while ramping to the processing temperature of 250°C. Although some transients can be observed during the initial 19 minute period of the open/close sequence, it is clear that they are insignificant with respect to the processing temperature. Removal of the samples from the furnace following the 90 minute process resulted in a cooling rate of 1.3°C/sec.

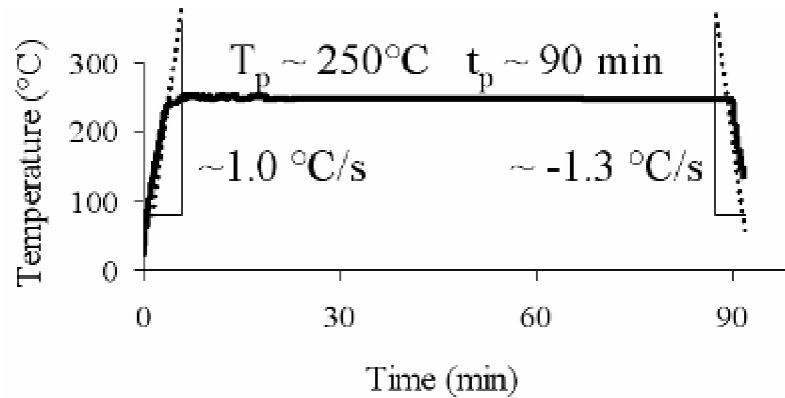


Figure 27. Ag-In TLPS profile as measured within Omega furnace.

Having discussed the test vehicles for the reliability study in addition to the fabrication of test assemblies with each of the three solder pastes it is now appropriate to describe the design of the testing procedures implemented during the reliability study portion of this investigation.

4.3 Reliability Testing Procedures

One of the aims of the reliability study portion of this investigation was to assess the suitability of the new Ag-In TLPS solder paste as a SMT material. It is not enough to simply serve as a connection between two surfaces; the given solder joint must be capable of reliably performing its intended functions for the desired amount of time to be accepted as a suitable solder material. Solder joints at the 2nd level of interconnection serve three important functions: electrical, mechanical, and thermal [15]. With respect to small signal applications associated with many SMT devices, the electrical and mechanical functions of the solder joints are paramount in realizing a successful package on the circuit board. Electrically, the solder joint is responsible for transferring the signal quickly and without distortion. With respect to its

mechanical responsibility, the solder joint must be capable of reliably fixing a SMT package to a given location on the circuit board under any number of loads that include vibration, shock, and bending, among others. In order to assess the electrical and/or mechanical reliability of a given set of solder joints, a number of tests can be performed that include thermal cycling, power cycling, vibration, shock, and thermal aging to name a few. For this investigation, passive thermal cycling of the sample assemblies was selected as the test to assess their relative reliabilities. In order to accurately assess the reliabilities of the solder materials, an experimental method was designed and implemented. The purpose of this method was to systematically apply the stressing conditions provided through passive thermal cycling and monitor the subsequent response from the SAC305, eutectic Au-Sn, and Ag-In TLPS test assemblies. Response of the solder joints was monitored through electrical testing, pull strength testing, and cross sectional sampling. Electrical testing was carried out through in-situ monitoring while pull strength testing and cross sectional sampling occurred at distinct intervals during cycling. Electrical testing of the experimental samples was used to monitor for and identify solder joints failures stemming from cracking and fatigue during passive thermal cycling. Mechanical testing was intended as supporting evidence of these failures because significant cracking within the joints would subsequently weaken the pull strengths of the samples. Although electrical and mechanical testing of solders is common practice, these methods of monitoring simply serve as indicators instead of representations of physical phenomena within the solder joint. For this reason, repeated sampling of solder joint cross sections over the duration of cycling was performed in order to understand the

physical changes within the joints that led to the electrical and mechanical behaviors that were observed.

4.3.1 Passive Thermal Cycling

During passive thermal cycling, the global CTE mismatch of 5 ppm/°C between the polyimide boards and the CQFPs was what caused stress to be placed on the solder joints and associated gull wing leads. For this assessment, two passive thermal cycling profiles were implemented in separate Sun Electronic Systems EC12 chambers. The Sun EC12 is a nitrogen cooled, bench-top temperature cycling machine capable of minimum and maximum temperatures of -184°C and 320°C, respectively [43]. Ramp rates up to 15°C/min are possible within the chamber. For simplicity, one of the profiles will be referred to as the high temperature (HT) profile while the other will be referred to as the low temperature (LT) profile. The HT profile was designed to subject test assemblies to temperature cycling from -55 to 185°C with a 5-minute dwell at -55°C and a 10-minute dwell at 185°C. This HT profile resulted in a ΔT of 240°C characterized by a mean temperature, T_{mean} , of 65°C. The LT profile was designed to subject test assemblies to temperature cycling from -55 to 150°C with a 5-minute dwell at -55°C and a 10-minute dwell at 150°C. This LT profile resulted in a ΔT of 205°C characterized by a T_{mean} of 47.5°C. Both of these profiles were designed to complete a full cycle every 96 minutes. Because of the difference in the ΔT magnitudes between the thermal profiles, the HT profile must heat and cool at a rate of ~6°C /min while the LT profile must heat and cool at a rate

of $\sim 5^{\circ}\text{C}/\text{min}$ in order to satisfy the aforementioned cycle period. A visual representation of the LT and HT profiles is illustrated in Figure 28.

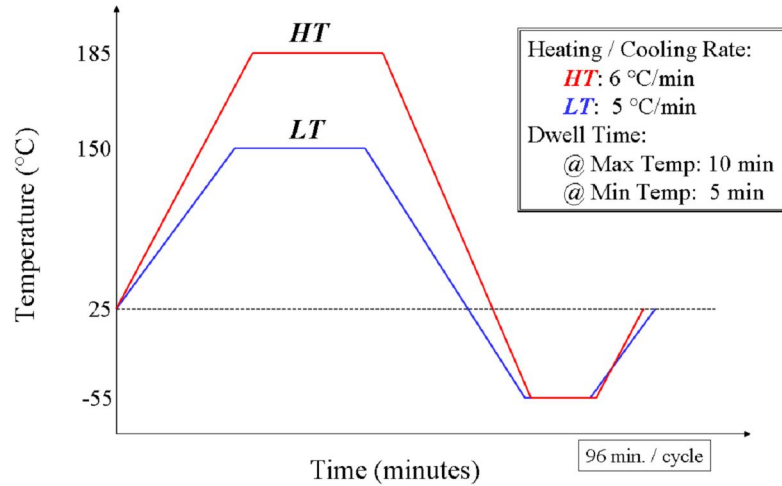


Figure 28. LT and HT profiles.

The controller programs implemented in order to carry out the above temperature profiles can be found in Table 7 below. It is important to note that the counting scheme of the for loop used in the LT and HT programs operates from 0,1,2...47,48,49 and immediately stops when $I0 = 50$. In this way it properly performs the desired 50 instead of what may appear to be 51 cycles.

Table 7. Sun Electronic Systems EC12 Controller LT and HT Programs.

LT Controller Program	HT Controller Program
For I0 = 0,50	For I0 = 0,50
Rate = 5	Rate = 6
Wait = 10	Wait = 10
Set = 150	Set = 185
Wait = 5	Wait = 5
Set = -55	Set = -55
Next I0	Next I0
End	End

As the above table suggests, passive thermal cycling was run within the EC12 chambers 50 cycles at a time. Practical implementation of cycling required this type of discrete testing schedule in order to make time for pull testing and microstructure sampling. Each 50-cycle period required 80 hours (3 days 8 hrs) within the chambers to complete. As a result, an average of 50 cycles per week was completed when accounting for the time required for testing outside of the chambers. Experimental samples were arranged inside the LT and HT chambers on a vertical, multi-leveled rack. Shelving for the racks was fabricated from aluminum, coarse mesh sheets to avoid from disturbing airflow within the chambers and skewing the internal temperature distribution.

4.3.2 In-situ Electrical Testing

Failure of the experimental solder joints was based upon their electrical behavior over the duration of this assessment. Electrical behavior of the joints was monitored through the collection and analysis of resistance data during cycling. Out of the three monitoring schemes planned for this investigation, electrical testing was the only one that could be conducted while the SAC305, eutectic Au-Sn, and Ag-In TLPS samples were under test in the temperature cycling chambers. This was a significant benefit over the other planned testing because it meant that the electrical test could capture the immediate response of the solder joints and detect a failure if it was in response to the temperature extremes experienced during cycling. As previously mentioned, each CQFP featured an electrical chain dedicated to monitoring one of the 8 corner solder joints that exist within the package. In accordance with IPC-SM-785 [44], 32 corner

solder joints were monitored per solder, per strain energy density condition for a total 384 resistances to be monitored during the experiment. This sample size recommendation was a statistical consideration because approximately 20 to 30 data points are required for properly determining the appropriate statistical fit to the failure data [45]. Further discussion of the stressing conditions for each of the solder materials will occur in the results and discussions portion of this work. In order to generate a data pool of 32 corner solder joints per solder per condition, 4 polyimide boards with their associated CQFPs were used to fabricate samples. Because 3 solder materials were the subject of this reliability study, a total of 12 boards were dedicated to electrical testing to satisfy the suggested sample size. Two boards of each solder material were cycled within each chamber for a total of 6 electrical boards within the LT chamber and another 6 in the HT chamber. In order to collect the resistance data from these boards, edge card connectors capable of withstanding temperatures up to 200°C were connected to the boards and wired to Agilent 40-channel multiplexer modules using the screw terminals provided. The interconnect wire used during this investigation also needed to withstand the temperatures within the HT and LT chambers. In recognition of this, Weico wire no. 2324 with a temperature rating of -60 to 200°C was used. The wired modules were then plugged into Agilent 34970A data acquisition switch units that were responsible for monitoring the 384 channels and logging the data in a useable format for analysis. An illustration of this setup can be seen in Figure 29.

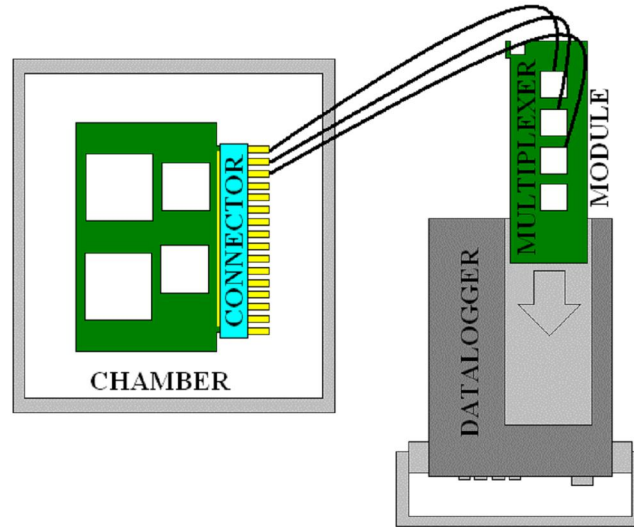


Figure 29. Electrical testing wiring.

In accordance with IPC-9701, a scan interval duration of one minute or less was observed while monitoring the resistance of these chains [1]. As per the specifications of the Agilent equipment, a 1 mA test current was applied to each electrical path during the measurement period. It is important to note that the operation of the 40-channel multiplexer modules ensures that only a single channel is connected at any time during the scanning process. When the measurement of a given electrical path is finished, the path is opened and a subsequent path closed for measurement. The failure definition of the solder joints will adhere to the suggested definition as provided by [1]: joints will be ruled failures when a 20 percent increase in nominal resistance is observed.

4.3.3 Mechanical Pull Testing

In addition to in-situ electrical monitoring of the solder joints, monitoring of the mechanical health of the assemblies was performed in order to correlate electrical behavior to another quantifiable metric. In order to accomplish this, a number of

assemblies equal to those used in electrical testing were fabricated for the sole purpose of mechanical testing during passive thermal cycling. Mechanical testing of the assemblies was performed through pull testing of the CQFP corner solder joints. Pull test samples were fixed in accordance with the published IEC standard for surface mount pull testing [46]. The standard stipulates that the plane of the substrate must be oriented 45° from the vertical of the pull test hook. This sample orientation is illustrated Figure 30.

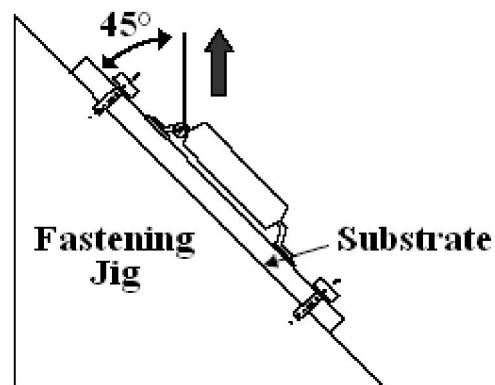


Figure 30. 45° pull test sample orientation [46].

Pull tests were conducted using the Dage 4000 series pull tester with a 10 kg load cell and test speed of $5 \mu\text{m/s}$. The test speed selected was the slowest available on the Dage 4000 and was chosen in order to maximize the probability that yield of the solder joint would occur during testing. Baseline, as-built pull strengths were collected for all three solders prior to passive thermal cycling. Changes in these pull strength values were expected to be indicators of cracking within the solder joints tested. To facilitate removal of the packages for testing, pre-cuts were made in the polyimide boards prior to fabrication of the assemblies marked for mechanical testing. As Figure 31 shows, the pre-cut locations within the test boards enabled the

removal of any of the 4 CQFPs by cutting away a small amount of material identified by the rings in the image. Implementation of the pre-cuts minimized required cutting when the packages needed to be removed for testing while still allowing the mechanical boards to be printed and processed in the same way as the electrical boards.

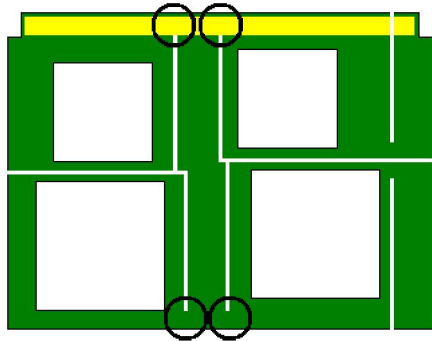


Figure 31. Pre-cut locations on polyimide test board.

4.3.4 Cross Sectional Sampling

The last of the three methods of monitoring the solder joints under test was cross sectional sampling. As previously mentioned, observation of the solder joint microstructure allows one to determine what is physically occurring to the sample, which can then be tied to changes in indicators such as joint resistance or pull strength. For this investigation baseline cross sectional images were collected from the corner joints of SAC305, eutectic Au-Sn and Ag-In TLPS samples. Following a desired number of temperature cycles, microstructures were again collected from these solders for comparison to the baseline. All stressing conditions were accounted for during this sampling as cross-sections from large and small CQFP packages were prepared each time data was gathered. Standard sample preparation using the

following progression in grinding paper grit was observed: 240→ 400→ 600→ 800→ 1200. When required, 1 micron alumina powder was used to polish the sample face. All samples were imaged using the Environmental Scanning Electron Microscope (ESEM) or light microscope.

Chapter 5: Reliability Assessment Results and Discussion

In order to assess the reliability of the solder materials during passive thermal cycling, the mechanical, electrical, and cross sectional data collected throughout this investigation were analyzed. Analysis of the data not only focused on trends observed within the particular sampling method, but how they related to the trends of other methods as well. For example, changes in microstructure during this investigation were closely tied to those in mechanical pull strength and vice versa. Discussion of the resulting data is divided among the solder joint sampling methods, however, relationships between the trends are identified when necessary. The corner solder joints of surface mount packages are expected to be the first to fail because they are subject to the highest strain energy densities that result from their location with respect to the neutral axis of the surface mount package. Mechanical, electrical, and cross sectional sampling were targeted for monitoring these corner solder joints. The combination of two temperature profiles with two package sizes ensured that 4 distinct solder strain energy densities existed within the various corner solder joints of the test assemblies. As a result, it is expected that the electrical, mechanical, and microstructural trends observed during this investigation will reflect this staggered damage scheme. In order to quantify these strain energy densities, material and geometry data was collected from the assemblies. These values were used as inputs in an equation for calculating the strain energy density of surface mount solder joints. The form of this equation is provided in the subsequent discussion along with the collection and estimation of the necessary parameters. Following this strain energy

density estimation, the results of the electrical, mechanical, and cross sectional sampling methods will be presented.

5.1 Solder Joint Strain Energy Density Estimation

As previously mentioned, when the test assemblies are subjected to one of the two selected thermal profiles, damage to the joints will occur as a result of the global CTE mismatch between the component and the substrate. The corner solder joints are said to experience the largest overall deformation or damage because they lie farthest from the package's neutral axis or center. The imposed cyclic damage within these joints can be quantified as the strain energy density, which is represented by the area within the shear stress-shear strain hysteresis loop. For surface mount, leaded components, the maximum cyclic strain energy density (ΔW) experienced by the solder joint can be estimated [47] by

$$\Delta W = \frac{K_d (L\Delta\alpha\Delta T)^2}{Ah} . \quad (5)$$

The variables from the equation are as follows: K_d – diagonal lead stiffness, A – minimum load bearing area of the solder joint, h – characteristic solder joint thickness, L – distance from package's neutral axis to the center of the corner joint, $\Delta\alpha$ – global CTE mismatch between component and substrate, and ΔT – magnitude of temperature change during thermal cycling. From this list it is clear that many of these variables are easily measured from the characteristics of the test assembly (A , h , L , $\Delta\alpha$) or have been predefined by the passive thermal cycling test set-up (ΔT). The

diagonal lead stiffness, K_d , is the one variable that requires more sophisticated estimation techniques to provide an input value for calculating ΔW .

5.1.1 Diagonal Lead Stiffness

As demonstrated above, the diagonal lead stiffness is a value that is critical in estimating the strain energy density experienced by solder joints during passive thermal cycling. The parameter itself is exclusively dependent upon the material and geometry of the surface mount lead and therefore completely independent of any material or geometrical considerations of the solder joint itself. Leads that are characterized as more compliant feature lower lead stiffness values while those that are less compliant have higher stiffness values. Lead stiffness of a surface mount package is an important characteristic that must balance two considerations. On the one hand, the surface mount leads must be compliant enough to absorb a significant share of the strain energy during cycling to protect the less compliant solder joints from early fatigue, while on the other, they must be stiff enough to tolerate the manufacturing process and maintain their form to ensure consistent solder joint formation. Computation of the stiffness values of a number of surface mount lead designs has been performed in prior works [48][49][50]. The generalized equations developed within these papers are extremely useful as a means of comparing the relative compliances of differing lead geometries in design for reliability exercises. For this particular investigation the equations developed for the inclined gull wing configuration described in [49] were used to estimate the diagonal lead stiffness of the corner leads on the 64-lead and 44-lead CQFP packages. All equations developed

within the aforementioned papers were based on classical elastic strain energy methods. The elastic loading assumption is one commonly made for lead frame materials whereas non-elastic assumptions regarding solder materials during passive thermal cycling are often required for accurate modeling of joint behavior. According to the authors, independent computation of lead stiffness values for the various surface mount lead designs in [48][49][50] was conducted using finite element structural modeling for validation purposes. With respect to the general equations developed in [49], six degrees of freedom that included translation along as well as rotation about the x, y, and z-axis were assumed to govern motion of the leads. For each of these possible motions, the lead was assumed to feature an independent flexural spring constant responsible for governing how it would respond. Due to limitations of the loading experienced during passive thermal cycling, the authors identified translation along the x and y axes, which together form a plane parallel to the surface of the circuit board, as the expected modes of lead motion during testing. It is important to note that such an assumption implies that negligible substrate warping occurs during passive thermal cycling of the test assemblies. The simplification regarding the expected loading during passive thermal cycling allowed the authors to compute two (of the six) flexural spring constants, K_x and K_y , to determine the operative stiffness of the corner gull wing lead. For this particular investigation, the equations to calculate K_x and K_y from [49] were implemented in MATLAB for the 44-lead and 64-lead CQFP packages and can be found in Appendix A. As the code shows, there are a number of geometry parameters that must be quantified in order to estimate the lead spring constants in the x and y directions.

Reproduction of spring constant values provided in [49] for a particular inclined gull-wing configuration served as a check of the aforementioned code. An illustration [49] demonstrates where these values are assessed on the inclined gull-wing lead.

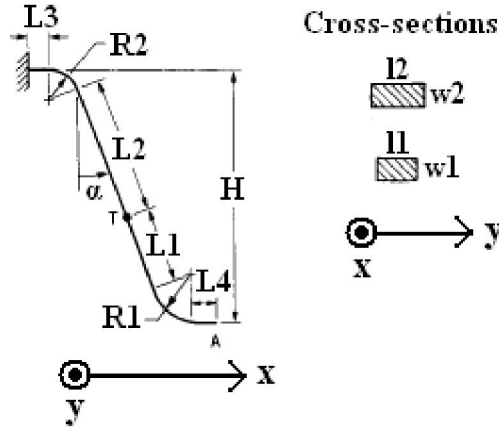


Figure 32. Structural model for inclined gull-wing [49].

As Figure 32 shows, the length values include $L1$, $L2$, $L3$, and $L4$ while $R1$ and $R2$ quantify the radius of curvature at the bends within the gull-wing structure. The angle, α , is the value, in radians, that defines the incline of the lead from the vertical. If there is a transition in the cross section of the lead, this location can be described in the model with point T , having a cross-section defined by $l2$ and $w2$ above this point and $l1$ and $w1$ below this point. For this particular investigation, there was no such transition within the cross section of the lead. For this reason, the value for $L1$ was defined as the entire length between the two radii of curvature and $L2$ was set to zero. Additionally, this lack of transition meant that $l2 = l1$ and $w2 = w1$ throughout the entire lead length. It is important to note that all previously mentioned geometries from the inclined gull-wing model are independent of one another. The last geometric variable defined in Figure 32 is that of the overall lead height, H . This

particular variable a function of L1, L2, R1, R2, and α and can therefore be computed from these values.

In order to quantify the average angle of inclination for each of the packages, 16 64-lead CQFP and 16 44-lead CQFP lead samples were measured. As was the case in the densification study, ImageJ was used to make measurements necessary in determining the inclination angle α . In order to facilitate discussion of the lead angle measurements, Figure 33 has been provided for reference.

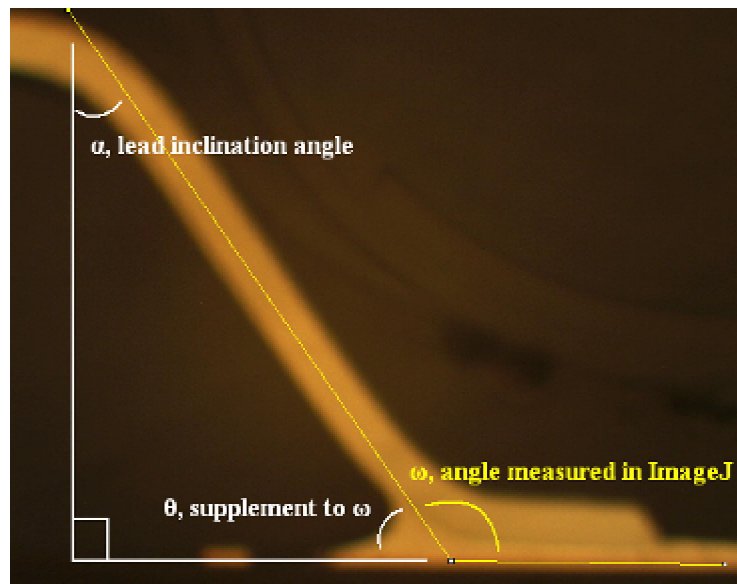


Figure 33. Lead angle definitions.

Within the ImageJ software there is an angle tool available for performing such measurements. The tool allows for the overlay of two vectors on top of the selected image. To ensure the most accurate angle measurements, one vector was placed along the centerline of the lead leg between the two radii of curvature and the other placed along the horizontal provided by the surface mount pad of the polyimide board. This angle was measured in favor of directly measuring α because there were

more visual cues afforded in measuring ω . Using trigonometric relations, the lead inclination angle, α , could be related to the angle measured in ImageJ, ω , through

$$\alpha = \omega - 90^\circ . \quad (6)$$

Using the 16 measurements of ω for each of the package sizes an average inclination angle was computed for leads of the 64-lead and 44-lead CQFPs. Independent averages were computed for the two package sizes because although the same tool was used to bend the leads to the geometries specified in Figure 16, the differing lead cross sections of the packages significantly influenced the final lead geometry following the trim and form process. As Table 8 demonstrates, there is a noticeable difference between the average inclination angles of the two different surface mount packages. Sample standard deviations, s , on the mean values have been provided for convenience.

Table 8. Average lead angles from 44-lead and 64-lead CQFPs.

	ω (degree)	α (degree)	s (degree)	α (radian)	s (radian)
44-lead CQFP	130.6	40.6	2.7	.71	0.048
64-lead CQFP	125.5	35.5	1.8	.62	0.03

These computed averages were then used in subsequent geometry calculations and ultimately for the estimation of the diagonal stiffness calculations.

With the average lead inclination angle of the two package sizes, further calculation of the lead geometry could be performed. The parameters, R1, R2, L1, L2, L3, and L4 were then the next to be quantified. In order to measure these variables of the inclined gull-wing structural model, simple geometric forms were overlaid on cross section images to trace the centerline of the gull-wing leads; the radii of curvature

were estimated using perfect circles while the linear variables were estimated using straight lines. The size of these geometric forms therefore served as estimations of the aforementioned parameters. A representative overlay of these shapes on a given cross section can be viewed in Figure 34.

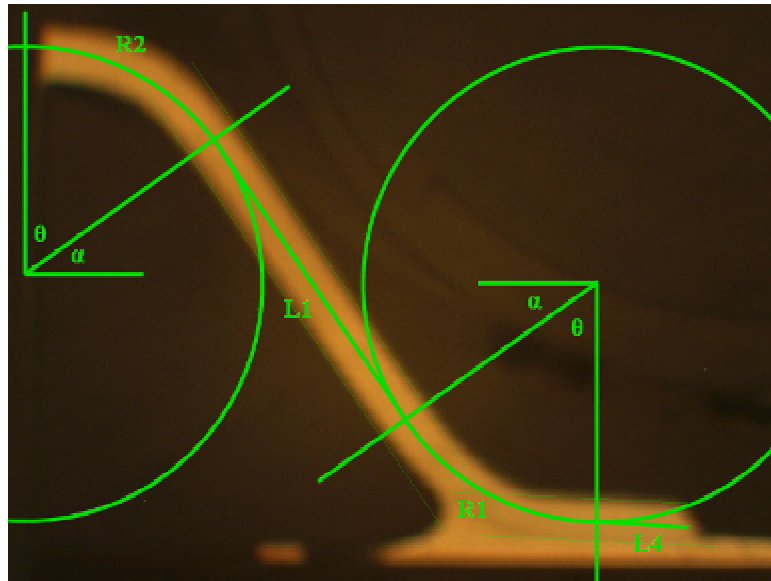


Figure 34. Geometric overlay of cross section images to estimate gull-wing structure.

Because of the cross section preparation process, the length associated with L3 was consistently destroyed by the band saw during removal of the leads from their respective packages. This characteristic of the cross section samples is clear from the representative image provided in Figure 34. In an effort to quantify this length, a measurement of the average cut width from the diamond band saw was performed. This measurement was then used in place of a direct measurement of L3. Due to the time intensive nature of the overlay estimation method, a total of 8 cross sections were analyzed between the two package sizes. The resulting averages computed from these samples are displayed, by package size, in Table 9 below.

Table 9. Estimated parameters of the inclined gull-wing structural model.

	R1 (mm)	R2 (mm)	L1 (mm)	L2 (mm)	L3 (mm)	L4 (mm)
44-lead CQFP	1.20	1.20	1.75	0	0.9	0.61
64-lead CQFP	1.15	1.15	1.70	0	0.9	0.52

As Table 9 shows, the radii of curvature for each package size were assumed to be equal due to observations made during the initial investigation regarding estimation of the above parameters. The overlay in Figure 34 serves to validate this assumption, as $R_1 = R_2$, while providing a good estimation to the centerline of the lead geometry. In order to check the averages provided in Table 9, the total curvilinear length provided by the estimates was calculated using

$$C = L_1 + L_2 + L_3 + L_4 + (R_1 + R_2)(1.5708 - \alpha), \quad (7)$$

from Kotlowitz and Taylor [49], where α is in radians. This equation can be easily established through inspection of the structural model in Figure 32 and implementation of trigonometric relations. The curvilinear lengths calculated using the above estimates were shown to be within 5 percent of the total 220 mil (5.6 mm) length denoted by the original gull-wing specification as shown in Figure 16.

Having determined values for all the parameters requiring estimation, the final values required for the code in Appendix A were those of the lead cross sections and material properties of the leads themselves. This information was readily available through specifications and drawings provided by the CQFP manufacturer. Leads of the 64-lead CQFP featured cross sectional lengths of 18 mil (0.46 mm) and widths of 8 mil (0.2 mm) while those of the 44-lead CQFP featured cross sectional lengths of 10 mil (0.25 mm) and widths of 11 mil (0.28 mm). The orientation of these measurements can be referenced to the gull-wing structural model provided in Figure

32. As mentioned previously in the experimental procedures section of this work, the leads of the CQFP packages were composed of alloy 42 with the appropriate surface coatings of nickel and then gold. From Brown et. al. [15], the elastic modulus of alloy 42 is 20.6×10^6 psi (142 GPa). In order to estimate the shear modulus of the material using

$$E = 2G(1+\nu) \quad (8)$$

from Timoshenko [51], Poisson's ratio, ν , of the material was necessary. This ratio was estimated as ~ 0.3 from the properties of Ni and Fe [52] using a simple rule of mixtures. This value in conjunction with $E = 20.6 \times 10^6$ psi (142 GPa) yielded a shear modulus, G , of 7.92×10^6 psi (54.6 GPa) using equation (8).

Having provided all necessary inputs to the generalized equations for computing K_x and K_y of the CQFP leads, the final estimation of these spring constants could be made. With these values for K_x and K_y , it was then possible to compute the diagonal lead stiffness of the corner leads using

$$(K_d)_{r=1} = 1.414 \frac{K_x K_y}{\sqrt{K_x^2 + K_y^2}} \text{ from Kotlowitz [48].} \quad (9)$$

The above equation for K_d is given for a square package featuring an aspect ratio of $r = 1$ only. It results from a simplification of other equations [48] suitable for rectangular packages with aspect ratios other than unity. The 44-lead and 64-lead CQFPs were both square packages, with side lengths of 0.65 inches (16.5 mm) and 0.9 inches (22.9 mm), respectively. The resulting K_d for both package sizes along with K_x and K_y are displayed below in Table 10.

Table 10. Inclined gull-wing lead spring constants.

	K_x (lb/in)	K_y (lb/in)	K_d (lb/in)	K_d (N/m)
44-lead CQFP	34.10	6.55	9.10	1595
64-lead CQFP	20.15	18.18	19.09	3345

The trend of the results above is expected for a number of reasons. With respect to the K_x values, the leads of the 44-lead CQFP should be, and are, stiffer than those of the 64-lead CQFP in this direction for two major reasons. Earlier mention was made of the larger lead inclination angle of the 44-lead CQFP when compared to that of the 64-lead CQFP. As the inclination angle of the lead is increased, the K_x and K_y spring constants increase accordingly. The gull-wing model provided in [49] predicts this stiffness value behavior with respect to inclination angle. In addition to a higher lead inclination angle, the leads of the 44-lead CQFP feature a larger cross sectional width, 11 mil (0.28 mm), than those of the 64-lead CQFPs, 8 mil (0.2 mm). This translates into a higher moment of inertia that resists bending caused by forces imparted to the lead along the x-axis. Table 10 reflects this reasoning as K_x for leads of the 44-lead CQFP is close to double that of leads from the alternative package. With respect to those values of K_y , the difference can be attributed to the significant disparity between packages in the material available to resist bending when the lead is acted upon by a force along the y-axis. As mentioned earlier, the leads of the 64-lead CQFP were 18 mil (0.46 mm) in cross sectional length while those of the 44-lead CQFP were only 10 mil (0.25 mm). It is because of this difference in cross sectional lengths that the K_y spring constant for leads of the 64-lead CQFP is close to triple that of leads from the alternative package. Sensitivity analysis on the x and y-direction stiffness values demonstrated that the cross sectional geometries of the package leads

were significantly more influential than the given difference in lead inclination angles. This behavior provides an explanation as to why the value of K_y for the 64-lead CQFP is approximately three times that of the 44-lead CQFP while consideration of the lead inclination angles would suggest the relationship should be otherwise.

As a check on how reasonable the results from Table 10 are, x and y direction lead spring constants of commercially available packages were sought out and located [53]. Leads on common Intel CQFP packages were cited as featuring K_x and K_y values of 9.05 lb/in (1585 N/m) and 23.0 lb/in (4030 N/m), respectively, while plastic quadflat packages (PQFP) featured K_x and K_y values of 39.8 lb/in (6970 N/m) and 85.9 lb/in (15050 N/m), respectively. Although the specific geometries of the leads on these packages are not known, it is beneficial to know that common surface mount packages feature leads with directional spring constants comparable to those calculated for this investigation.

5.1.2 Diagonal Length, CTE Mismatch, and ΔT

Having appropriately estimated the diagonal lead stiffness for leads of the 44 and 64-lead CQFPs, there is one remaining term in the numerator of the strain energy density calculation that requires quantifying. This term, $(L\Delta\alpha\Delta T)^2$, is defined by the half component diagonal, L , the global CTE mismatch between the polyimide board and ceramic body of the CQFP, $\Delta\alpha$, and the temperature swing, ΔT . As defined by the specifications and drawings of the CQFPs, the 64-lead CQFP features a square body 0.9 inches (22.9 mm) along a side while the 44-lead CQFP features a square body 0.65 inches (16.5 mm) along a side. These dimensions translate into half component

diagonals of $L_{64\text{-lead CQFP}} = 0.64$ inches (16.25 mm) and $L_{44\text{-lead CQFP}} = 0.46$ inches (11.7 mm). With respect to the global mismatch, this variable has already been defined many times as $5 \text{ ppm}/^\circ\text{C}$ ($\alpha_{\text{polyimide}} = 12 \text{ ppm}/^\circ\text{C}$, $\alpha_{\text{alumina}} = 7 \text{ ppm}/^\circ\text{C}$). The temperature swings have also been previously defined and identified by the HT cycle, where $\Delta T = 240^\circ\text{C}$, and the LT cycle, where $\Delta T = 205^\circ\text{C}$. With the entire numerator of the strain energy density equation defined and quantified, it is now appropriate to complete the estimation by quantifying the denominator.

5.1.3 Minimum Load Bearing Area and Characteristic Solder Joint Height

As defined [47], the minimum load bearing area of the solder joint, A , can be quantified as two-thirds the solder wetted lead area projected to the surface mount pad. The characteristic solder joint height, h , is typically defined as half of the solder paste stencil thickness, but because of the available experimental samples and ease of estimation using the ImageJ software, it was decided that this height should be gathered from the solder cross sections as well. In order to estimate h , an average solder joint height was calculated from the given samples by computing the cross sectional solder joint area directly beneath the wetted lead length and dividing it by the wetted lead length projected to the surface mount pad. This calculation therefore yielded an estimate of the average solder joint height, h , which would provide an equivalent cross sectional area when multiplied by the wetted lead length projected to the surface mount pad. An illustration of these values can be seen below in Figure 35.

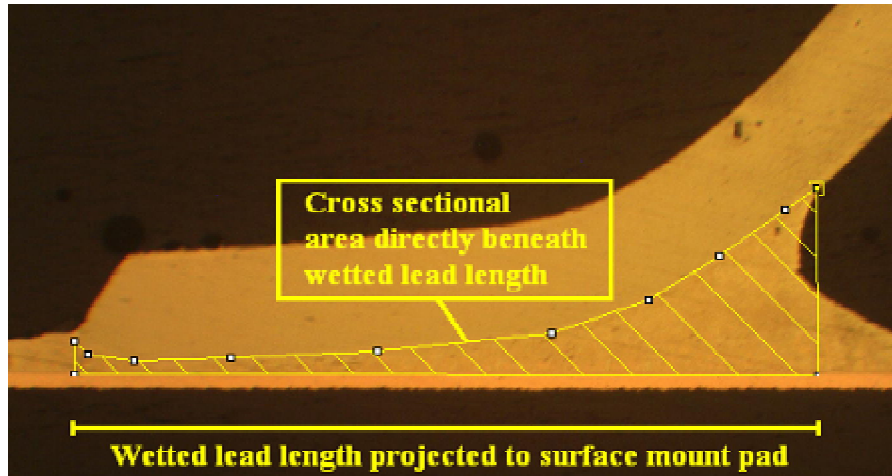


Figure 35. Measurement definitions in estimating characteristic solder joint height.

In order to estimate the minimum load bearing area of the solder joint, the wetted lead lengths projected to the surface mount pad were multiplied by the cross sectional lead lengths (identified in Figure 32) and finally by a factor of $2/3$ as called for in the definition. As previously discussed during the estimation of the lead diagonal stiffness, these cross sectional lead lengths were defined as 18 mil (0.46 mm) for the 64-lead CQFP and 10 mil (0.25 mm) for the 44-lead CQFP from the available manufacturer specifications. For the eutectic Au-Sn and SAC305 samples printed with the 8-mil (200 μm) thick stencil, averages for the characteristic solder joint height and minimum load bearing area were estimated from a total of 16 samples for each component size. The Ag-In TLPS samples fabricated from printing with a 6-mil (150 μm) thick stencil were initially assessed differently due to the fact that a smaller characteristic solder joint height was expected due to the thinner stencil, however, it was demonstrated that the average height and minimum load bearing areas were very similar to those computed for Au-Sn and SAC305. As a result, the average solder joint height and minimum load bearing area for each of the component sizes were computed independent of the solder joint materials for ease of discussion in

subsequent sections. The values resulting from these computations can be found in Table 11.

Table 11. Characteristic solder joint heights and minimum load bearing areas.

	h (mil)	h (μm)	A (sq. mil)	A (μm^2)
44-lead CQFP	4.0	101.6	368	237420
64-lead CQFP	4.6	116.8	671	432900

With respect to the values shown above, it is clear that the estimate of half of the stencil thickness serves as a good indicator of the characteristic solder joint height when traditional solders are used. In the case of the Ag-In TLPS material where full melting does not occur, blindly using such an estimate would have predicted a solder joint height of ~3 mil (76 μm) while the true characteristic solder joint heights were as much as 1 to 1.5 mil (25 to 38 μm) greater than this value. This behavior is likely a result of the porosity of the joints. Having quantified all values associated with the estimation of the strain energy density within a surface mount solder joint, the various strain energy densities resulting from the different package size / temperature swing interactions can be computed.

5.1.4 Strain Energy Densities

By design, this investigation was intended to feature four distinct strain energy densities that could be used to quantify the difference in damages experienced by the surface mount solder joints during passive thermal cycling. The successful estimation of all parameters related to strain energy density through equation (5), as previously described, allowed for computation of these distinct strain energy densities as a

function of package size and cyclic temperature swing. These values are provided in Table 12 and will be used to simplify subsequent reliability testing related discussion.

Table 12. Strain energy densities.

		ΔW (lb/in ²)	ΔW (N/m ²)
44-lead CQFP	LT	1.4	9650
	HT	1.9	13100
64-lead CQFP	LT	2.7	18615
	HT	3.6	24820

For convenience, the strains, $\Delta\gamma$, experienced by the solder joints under test were estimated as well. These strain estimations are inherent within the calculation of the strain energy densities from equation (5) as $\Delta W = S\Delta\gamma$, where S represents the maximum stress and $\Delta\gamma$ represents the strain range within the solder joints during passive thermal cycling [47]. The strain range estimations are provided in Table 13.

Table 13. Strain range estimations.

		$\Delta\gamma$
44-lead CQFP	LT	0.119
	HT	0.140
64-lead CQFP	LT	0.142
	HT	0.167

5.2 Electrical Data Trends and Discussion

As was discussed in the experimental procedure section of this work, a total of 384 chain resistances were monitored during passive thermal cycling. Following every 50 cycles, the data files generated from the resistance readings were removed from the computer linked to the data logger array. At a sampling rate of one reading every minute, each 50 cycle duration generated ~1.85 million resistance values across all samples. In order to manage such a vast amount of data, a number of MATLAB

programs were created to aid in the tagging and analysis process. These codes can be found in Appendix B and will be discussed later.

From the baseline resistance testing conducted prior to passive thermal cycling, it was observed that the resistances of the surface mount solder joints were negligible when compared to the resistances of the daisy chains of which they were a part. This observation held true for the SAC305, eutectic Au-Sn, and Ag-In TLPS test assemblies. A significant fraction of the monitored resistance was attributed to the inclined gull wings and internal wirebonds connecting these leads together in packages of both sizes. In order to confirm this, unsoldered packages were sampled for the resistance of electrically connected lead pairs. The schematic of which lead pairs were electrically connected to one another can be observed in the wirebond schemes provided in Figure 14 and Figure 15. With respect to the 64-lead CQFPs, this lead pair resistance was found to be $\sim 0.33 \Omega$ having removed all contributions from contact resistance. In the 64-lead CQFPs, the daisy-chain pattern designed for this investigation featured four of these lead pairs per chain monitoring the solder joints on each corner. As a result, the total resistance contribution from the electrically connected lead pairs was estimated to be $\sim 1.32 \Omega$. When baseline data collected from 64-lead CQFP daisy chains were corrected to eliminate resistance due to PWB trace lengths, connector contact resistance, and interconnect wire lengths the average resistance value of just the joints plus the lead pair resistances was found to be $\sim 1.36 \Omega$. Correction values were generated from direct resistance measurements, resistance estimations from measured trace lengths, and manufacturer provided data. These correction values were subtracted from the raw resistance data to arrive at the

corrected resistance values. It is clear that the resistances of the gull wing leads and wirebonds within the 64-lead CQFP heavily influence the corrected daisy chain resistance of 1.36Ω as they account for close to 97% of this value. Similarly large resistance fractions were noted for 44-lead CQFPs as well. Corrected daisy chain resistances for the 44-lead CQFPs were found to be ~ 0.83 and $\sim 0.6 \Omega$ for those chains featuring three and two electrically connected lead pairs, respectively. The total resistance contributions from the lead pairs in the 44-lead CQFPs were measured as ~ 0.6 and $\sim 0.4 \Omega$ for those chains featuring three and two lead pairs for an average contribution of 70% of the corrected resistance values. Although these corrected values were useful in identifying the fraction of the resistance contributed from sources other than the solder joints themselves, the raw resistance values were used as the nominal values for analysis and failure definition instead. This decision was made following observations of the raw data subjected to passive thermal cycling. As one would expect, it was shown that the temperature within the chambers significantly affected the raw resistances of the monitored daisy chains. Because the aforementioned correction values could not be independently characterized as a function of temperature, it was decided that use of the raw data would be less prone to error and therefore a more accurate metric for defining failure. A discussion of the observed raw resistance temperature dependence and its impact on the assumed failure definition will follow.

Prior to passive thermal cycling of the test assemblies, the experimental procedure called for a failure definition of a 20 percent increase in the nominal resistance of the monitored chain, as given in [1]. However, data collected from initial cycling

revealed that the raw resistance of daisy chains surpassed this criterion during every heating stage of both thermal profiles. An example of this temperature dependent resistance behavior is displayed for a 64-lead CQFP, Au-Sn chain in Figure 36. As the temperature trend on this plot shows, the chain was subjected to the LT profile. It is clear from the resistance trend that the 20% threshold is easily surpassed during a typical LT cycle. In fact, the maximum chain resistance was found to be ~40% higher than the nominal resistance registered at room temperature.

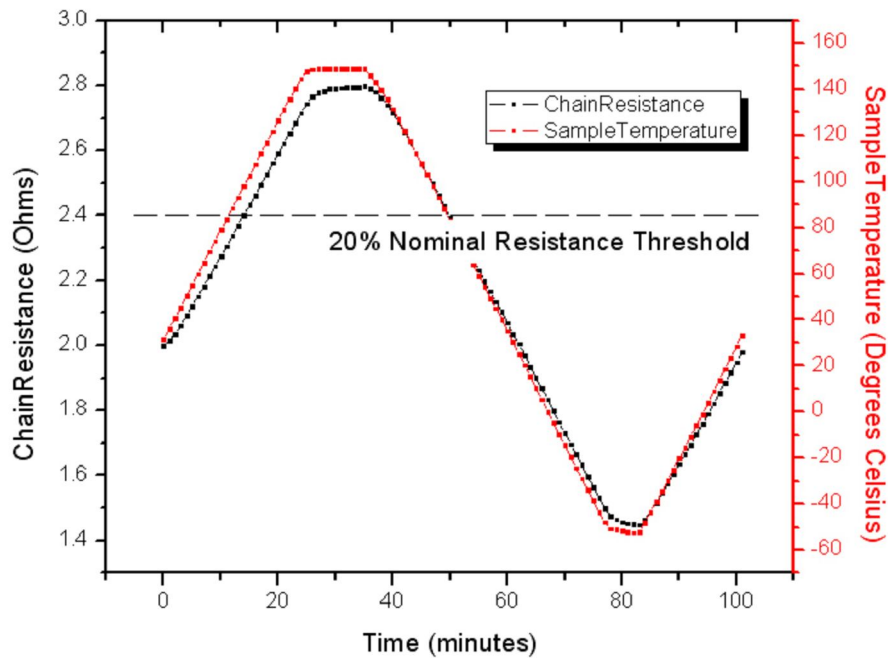


Figure 36. Au-Sn chain resistance and temperature as a function of passive thermal cycling time.

All test assemblies monitored for raw chain resistance were observed to surpass this prior established threshold for defining electrical failure. For all solder materials, those chains of 64-lead CQFPs were found to have maximum resistances of ~70% and 40% above their nominal values when subjected to HT and LT profiles, respectively. Those chains of 44-lead CQFPs were found to have maximum

resistances of ~55% and 40% above their nominal values when subjected to HT and LT profiles, respectively. Because of this behavior, it is necessary to consider an alternative definition of electrical failure. Although industry standards [1] provide useful information for setting up and conducting testing, it is important to always consider the behavior of the samples under test prior to accepting any generic failure definitions provided by the literature. Similar conclusions regarding the selection and acceptance of failure criteria from accepted industry standards without consideration of sample characteristics were reflected in other works [54]. In order to ensure that resistance signals interpreted as electrical failures were indeed indicative of some type of crack or delamination within the solder joint, redefinition of failure was reserved until cross section images could be used to confirm out-of-the-ordinary resistance behavior.

In an effort to characterize the signatures of healthy solder joints to use as reference for subsequent failure definition, plots were generated from data gathered during the first 50 thermal cycles for all materials and strain energy densities. As previously discussed, the large amount of data collected on a weekly basis required a minimum level of automation in order for the data analysis to be manageable. In order to automate the plotting of chain resistance data, a MATLAB program was created. This automatic plotting program can be found in Appendix B. Prior to execution, the program required the user to specify the location of the data to be plotted and to what destination the generated plots were to be saved. After this, the program would then automatically plot and save the graphs in a series of labeled bitmap files. These plots could then be observed in order to identify trends in the resistance behavior. At the

beginning of experimentation, these plots served as the baseline resistance signatures of healthy test assemblies against which subsequent signatures would be compared. A sample plot generated from the program for a 44-lead CQFP, SAC305 daisy chain can be viewed in Figure 37 below. This particular chain from the plot below was subjected to its first 50 HT cycles and therefore representative of the chain when all joints were healthy and relatively undamaged.

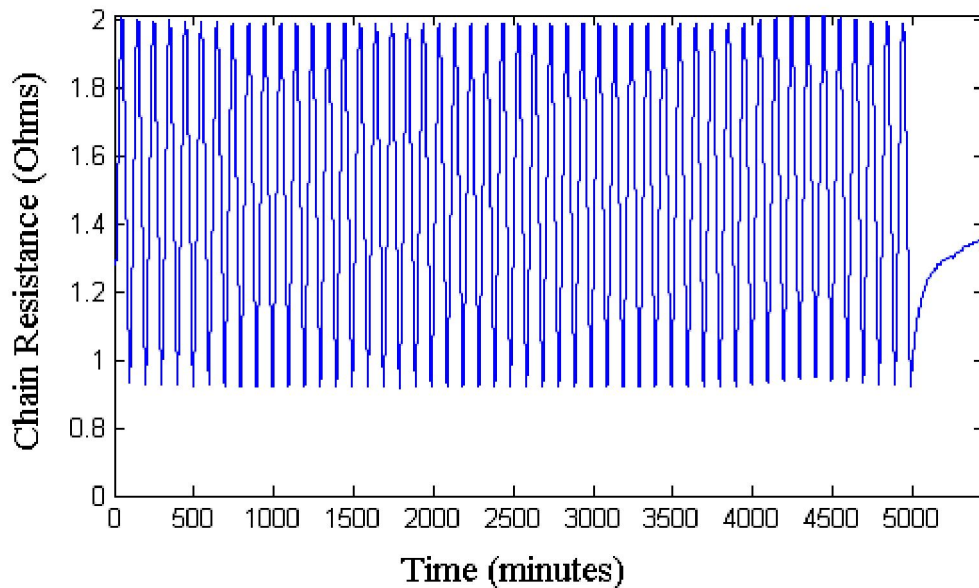


Figure 37. Representative baseline resistance signature of a 44-lead CQFP, SAC305 daisy chain.

As Figure 37 shows, the trend of the chain resistance is highly repeatable as one might expect. The cyclic variations are, of course, directly related to the change in temperature during passive thermal cycling. The correlation of chain resistance to sample temperature is clearly displayed in Figure 36. For this particular chain, the resistance varied from ~2 ohms at 185°C to ~.95 ohms at -55°C. Although other chains did not adhere to these absolute limits, the forms of their automatically generated resistance plots were very similar to that displayed above. Those chain

resistance plots that varied in any way from their established baselines were subsequently investigated as potential corner joint failures.

Over the course of passive thermal cycling, a number of chain resistance signatures began showing signs of what were initially interpreted as corner solder joint failures. Generally speaking, these “failed joint” signatures were spread evenly among the solder materials used to fabricate the test assemblies. The abnormal resistance plots were first recognized in the population of SAC305 test assemblies around 250 to 300 passive thermal cycles. Many times small instabilities were evident in the early stages of cycling that subsequently grew into larger inconsistencies with an increasing number of thermal cycles. This progressive deterioration of some of the chain resistance trends suggested the gradual weakening and eventual destruction of the surface mount solder joints in question. With respect to the SAC305 test assemblies, cross sections of selected samples at 400 passive thermal cycles seemed to confirm the possible electrical deterioration as significant cracking was observed in corner joints of both package sizes subjected to HT cycling. Although this offered a convincing correlation, investigation of the other materials within the study soon called this agreement into doubt. During this investigation, samples fabricated from eutectic Au-Sn were found to be extremely reliable under the environmental conditions as cracks were not detected in any of the cross sections prepared nor did the mechanical strength data collected suggest significant degradation of the corner solder joint. However, some Au-Sn chain resistance signatures were found to degrade in a fashion similar to those from the SAC305 and Ag-In TLPS populations.

A chain resistance representative of the degradation observed across samples can be seen below for a 64-lead CQFP, Au-Sn chain subjected to HT cycling.

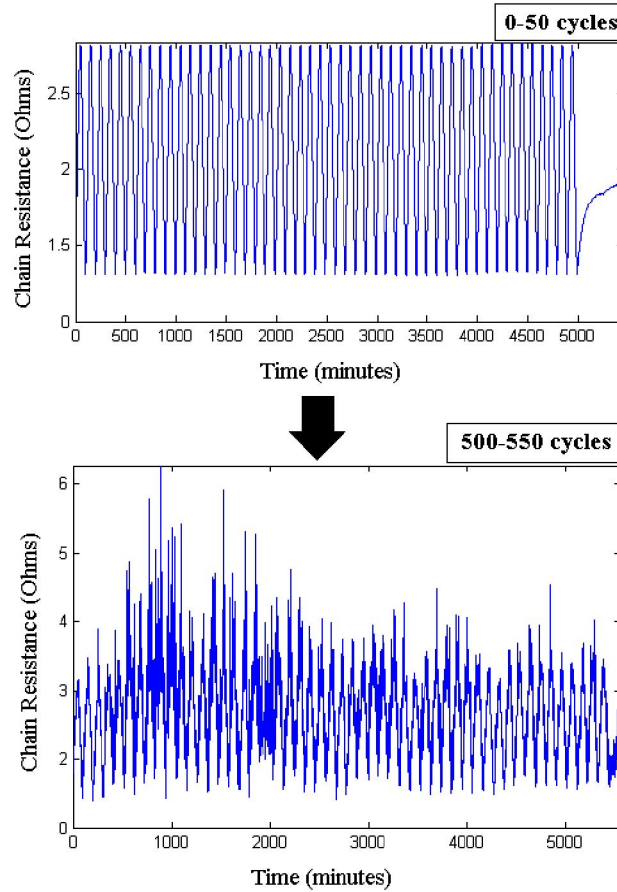


Figure 38. Chain resistance degradation as a function of passive thermal cycles.

As Figure 38 shows, by 500 thermal cycles the daisy chain characterized by these signatures looks to have changed in a way that has caused the 500 to 550 cycles plot to become significantly more irregular than that of the baseline. At various points in the latter of the two plots, the chain resistance more than doubles the resistance readings of the baseline. As previously mentioned, all mechanical and cross sectional data collected for the Au-Sn samples showed no indication of joint failures during cycling. This discord between the electrical, mechanical, and cross sectional data

prompted an investigation into the causes behind the degrading electrical behavior of some chains in the Au-Sn, SAC305, and Ag-In TLPS test assemblies.

Due to the nature of the electrical testing performed during this investigation there existed a number of failure points within the wiring route that might explain why the chain resistance signature behaved as it did for the Au-Sn daisy chain displayed in Figure 38. As previously mentioned, in order for the data logger array to monitor the chains within the test assemblies, a continuous path from the positive to negative terminal of the multimeter within the data logger was required. This continuous path was described in the experimental procedure section above and illustrated in Figure 29 from earlier. Figure 39 below highlights a total of 7 possible locations in the wiring scheme where the electrical signal could be affected by degradation or faulty connections. These locations include the following:

1. the solder joints within the daisy chain of the surface mount package,
2. the PWB traces running to and from the package daisy chain,
3. the press-fit connection at the edge card connector / PWB interface,
4. the solder joint connecting the hook-up wire to the edge card connector,
5. the hook-up wire itself,
6. the screw terminal between the hook-up wire and multiplexer module, and
7. the press-fit connection at the multiplexer module / data logger interface.

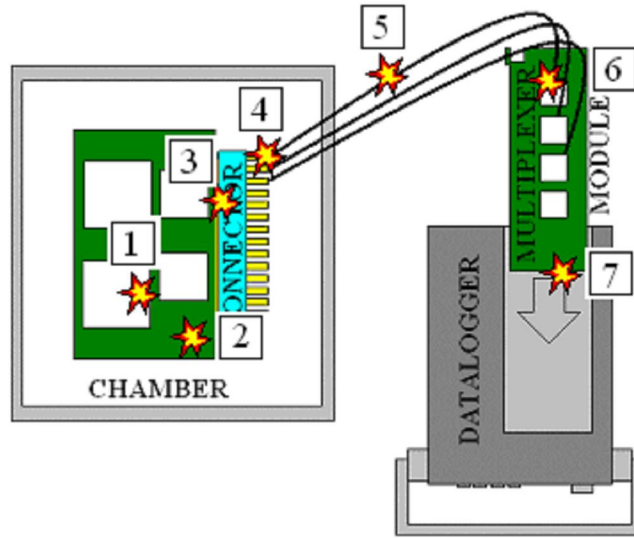


Figure 39. Potential failure sites within electrical wiring.

In order to determine if any of these possible failure sites was causing the inconsistencies, a diagnostic approach was taken. As a preliminary measure, those chains that exhibited the erratic chain resistance signature displayed in Figure 38 were tested at room temperature with a hand-held ohmmeter. When all chains in question were checked, the probe points of contact were shifted throughout the remaining wiring levels to determine whether any additional resistances above the baseline signatures could be detected. This room temperature probing failed to confirm any electrical issues at the potential sites already identified, however, this result was not unexpected as many times electrical failures during passive thermal cycling occur only during periods of actively changing temperature. In an effort to identify the failure site location under passive thermal cycling, dummy PWBs were fabricated from 62 mil (1.6 mm) thick aluminum cut to the appropriate size for insertion into all edge card connectors under test. These aluminum inserts provided the means to test potential failure sites 3 through 7 when subjected to passive thermal cycling. By

moving to this step in the diagnostic process it was assumed that failures were not located within the surface mount solder joints or any connective wiring on the PWB. This assumption was made because of the evidence provided by the healthy eutectic Au-Sn samples in addition to the fact that testing these sites under passive thermal cycling without the data logger array would have required an additional monitoring set-up. Provided that failure could not be detected with this new diagnostic set-up, it would have suggested that the boards or solder joints were, in fact, the failure sites of interest.

The chain resistance signature provided in Figure 40 is from the same Au-Sn chain as discussed in Figure 38, save for the fact that the dummy aluminum PWB was inserted in place of the true PWB. It is clear from the image that this waveform is irregular as well. In contrast to this behavior, those chains that exhibited predictable, cyclic behavior as shown in Figure 37 continued to behave as such when the dummy aluminum PWBs were tested. When the data collected from passive thermal cycling with the Al inserts was cross-checked with the earlier sample data, it was observed that every degrading electrical signal was again observed in the dummy tests. This result suggested that failures existed between the data logger array and edge card connectors and were not a function of damage in any surface mount solder joints.

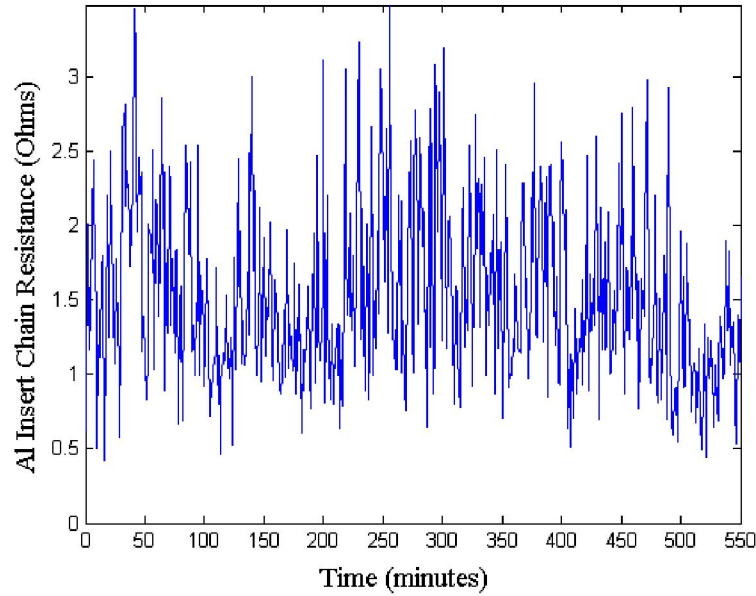


Figure 40. Resistance trend of a chain completed by an aluminum insert.

In response to the feedback indicating that some type of failure between the edge card connector and data logger array was responsible for the erratic behavior, repairs were immediately made to solder joints connecting the hook-up wire to the edge card connector. These repairs were performed by applying additional high-lead solder to each of the eyelets connected to channels on the multiplexer module by way of hook-up wire. Additionally, hook-up wires were inspected for cuts or imperfections caused by temperature cycling and screw terminals of the multiplexer modules were tightened when necessary to ensure ideal electrical contact. Spring contacts of the edge card connectors were also checked to ensure that stress relief of these parts was not causing the irregular signatures. Subsequent testing of the connectors was again conducted with the Al inserts to check if the repairs had corrected the erratic resistance signatures. Following this second session of testing with the dummy aluminum PWBs, the erratic resistance signatures were still observed, therefore suggesting that the source of these variations came from the multiplexer modules

themselves or their connections to the data logger array. Final adjustments were made by switching connectors among multiplexer modules to observe whether the erratic chains traveled with the connectors or whether they were characteristic of the multiplexer module in question. When sample data from an old connector on a multiplexer module was compared with data collected on the same module with a new connector, the chain signature remained much the same. Those modules that behaved predictably as a function of temperature on the old connectors did so on the new connectors and those modules that exhibited a chain signature that behaved erratically on the old connectors were shown to do the same on the new connectors. An example of this behavior is demonstrated in Figure 41 in which a given multiplexer module recorded SAC305 resistance data using edge connector B while during later dummy testing it was used to record aluminum insert data using an entirely different edge connector L. The selected chain presented in the figure demonstrates how similar the resistance signatures are even though the only common thread between the two is the module used during the resistance monitoring process.

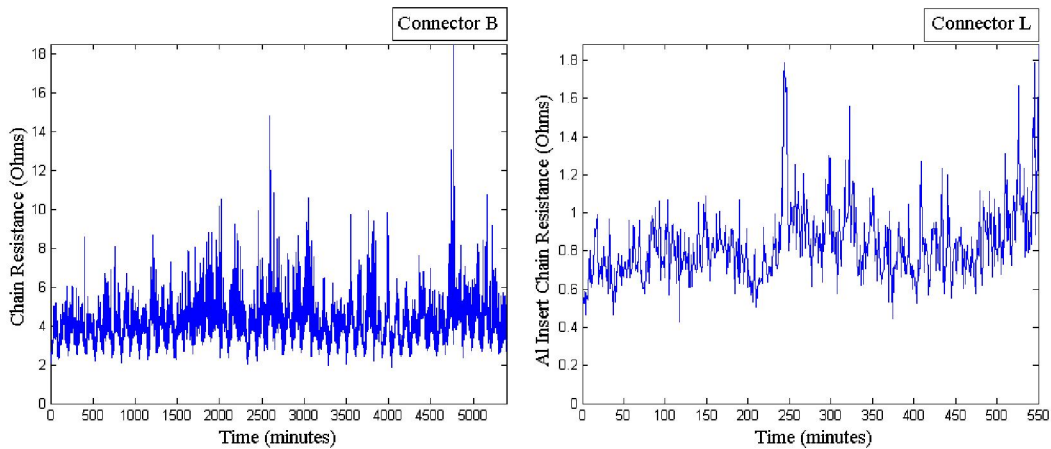


Figure 41. Observed chain similarities across varying samples and connectors.

The resulting conclusion gathered from the diagnostic work performed during electrical testing was that as passive thermal cycling carried on, select channels of the multiplexer modules became corrupted and began recording distorted resistance data. Although it is not known what caused this corruption, or how to avoid it, steps were taken to mitigate its effects on the sample populations. In other words, all corrupted channels on the multiplexer modules in question were identified so that the appropriate sample swapping among modules could take place to maximize the number of uncorrupted readings during electrical testing. Within solder materials, those multiplexer modules that showed no channel corruption were switched with those that showed a significant amount of corruption, up to ~30% of channels on the module in some cases. This approach in preserving the validity of the electrical data was necessitated by the limited number of multiplexer modules available. Subsequent sample swapping was extremely effective in mitigating the effects of the corrupted channels on the breadth of electrical data; however, it was not able to eliminate them altogether. As mentioned earlier, the sample population for electrical testing was designed to feature 32 corner solder joints per solder material per strain energy condition. Some of these original sample populations, P_0 , were modified when the corrupted channel effects could not be removed. These adjusted populations, P_{adjusted} , are displayed in Table 14.

Table 14. Adjusted Electrical Sample Populations.

	Chamber	Package	ΔW (N/m ²)	P ₀	P _{adjusted}
Ag-In TLPS	LT	44-lead CQFP	9650	32	27
-	HT	-	13100	32	28
-	LT	64-lead CQFP	18615	32	32
-	HT	-	24820	32	28
Au-Sn	LT	44-lead CQFP	9650	32	32
-	HT	-	13100	32	28
-	LT	64-lead CQFP	18615	32	32
-	HT	-	24820	32	30
SAC305	LT	44-lead CQFP	9650	32	32
-	HT	-	13100	32	29
-	LT	64-lead CQFP	18615	32	32
-	HT	-	24820	32	31

At the conclusion of thermal cycling and testing, the Au-Sn and SAC305 samples had accrued 800 cycles while the Ag-In TLPS samples had been subjected to 400 cycles.

The decision to conclude testing was arrived upon in response to cracking observed in sample cross sections in addition to the behavior of sample mechanical strengths.

These other considerations will be discussed in more detail within subsequent sections. Although significant cracking within the Ag-In TLPS and SAC305 joints was observed in samples taken from the cycled population, the resistance signatures at the conclusion of passive thermal cycling did not reflect these observations. In fact, all corner solder joints from the adjusted populations featured final resistance signatures characteristic of their original baselines. This was an expected outcome for the Au-Sn samples as cross sectional and mechanical data suggested the joints had not suffered significant, permanent damage during passive thermal cycling, however, it warrants discussion with respect to the Ag-In TLPS and SAC305 samples. For these samples, it is hypothesized that the resistance sampling rate in conjunction with the number of solder joints within each daisy chain may be responsible for this

behavior. Although significant cracking was observed in the Ag-In TLPS and SAC305 corner solder joints, it is reasonable to suggest that compressive forces from adjacent joints were responsible for holding any fractured surfaces in sufficiently good contact with one another. If the cracking had occurred through the entire joint, subsequent thermal cycling would have caused these surfaces to slide relative to one another, therefore causing transient resistance changes that can be recorded by continuously monitoring event detectors or oscilloscope setups. Although the resistance data failed to characterize this cracking within the corner solder joints, the mechanical data collected during this investigation did correlate with these physical observations.

5.3 Mechanical Data Trends and Discussion

In contrast to the in situ measurements possible with electrical testing, the mechanical testing portion of this investigation required careful sample planning in order to balance the resolution and absolute range of the assessment. Because the mechanical testing was destructive in nature, the finite number of mechanical samples prepared for testing needed to be carefully distributed among the planned test points during cycling. Without knowledge of how the samples would behave in response to passive thermal cycling, mechanical sampling points were placed closely to one another during the initial stages of cycling. This high resolution was planned in order to capture any short-term changes to the solder joints that would have affected pull strength. The number of cycles between mechanical test points was then gradually increased in order to preserve sample quantities for longer than planned passive

thermal cycling or unexpected changes in mechanical strength during the later stages of testing that may have required additional resolution. The resulting sampling schedule when taking all of these considerations into account was as follows: 0, 50, 100, 200, 400, 600, and 800 passive thermal cycles. During testing, SAC305 remained on schedule while mechanical samples were collected from Au-Sn mechanical assemblies at 700 instead of 600 passive thermal cycles and from Ag-In TLPS samples at 250 instead of 200 passive thermal cycles. This deviation from the planned sampling schedule was driven by concerns about sample populations. A summary of the true sampling periods and populations observed during this investigation can be seen below in Table 15.

Table 15. Observed mechanical testing periods and samples.

	Passive Thermal Cycles								
	0	50	100	200	250	400	600	700	800
Ag-In TLPS	7	4	3	-	4	7	-	-	-
Au-Sn	7	4	3	4	-	3	-	4	7
SAC305	7	4	3	4	-	3	4	-	7

The number of corner solder joints tested at each of the sampling periods can be seen above in Table 15. Larger sample populations were collected at the beginning and end of mechanical testing in an effort to reduce data variation at these points. This reduction in variation enabled conclusions regarding trends in the pull strength data to be made with higher confidence. Many of the sample populations cited in Table 15 are odd in number because at these intervals, single samples were set aside for cross sectioning. Proper discussion of the data collected through cross sectioning will occur in the sections to follow.

5.3.1 SAC305 Mechanical Results

Presentation and discussion of the mechanical testing results will be divided among solder materials in order to identify failure modes and mechanical strength trends specific to the individual solders prior to making any general comparisons between them. The first of the solder materials to be discussed is SAC305. Pull testing of these samples yielded consistent interfacial failures between the bottom of the surface mount lead and top of the solder joint as described in [46]. The location of these failures with respect to the surface mount assembly is illustrated in Figure 42 below.

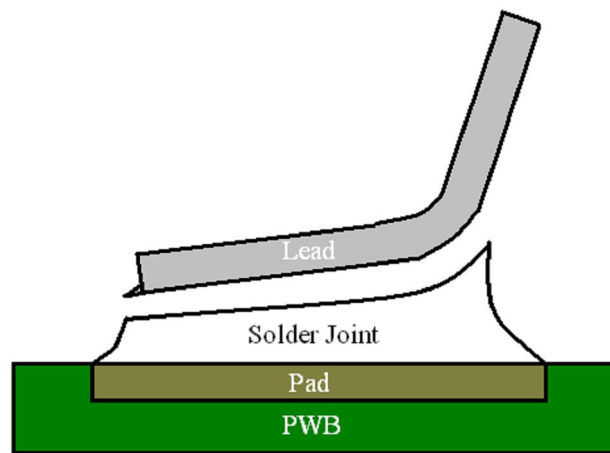


Figure 42. Interfacial failure between component lead and solder joint during pull strength testing.

This failure mode was observed throughout mechanical testing of SAC305 samples for both package sizes and temperature cycling conditions. Cross sections of SAC305 joints demonstrated that a significant intermetallic layer existed between the surface mount lead the solder joint itself. This intermetallic was likely the location of failure as cracking along this feature in HT SAC305 samples correlated with a decrease in recorded pull strengths during mechanical testing. In order to provide the

mechanical data in a presentable format, sample means and variances were calculated using the following equations, respectively:

$$\bar{X} = \frac{1}{n}(X_1 + X_2 + X_3 + \dots + X_n) \quad (10)$$

and

$$S^2 = \frac{1}{n-1} \sum_{j=1}^n (X_j - \bar{X})^2 \text{ from Kreyszig [55]}. \quad (11)$$

The normal distribution was assumed to govern the shape of all mechanical sample probability density functions. Although sample standard deviations were computed to characterize the calculated means, they were not used directly to present the pull test data. Rather, these values were used to calculate 90% confidence intervals (CIs) on the established means; these CIs were then used in subsequent presentations of the pull strength trends.

With respect to the strength trends observed within the SAC305 population, there was a distinct difference based upon passive thermal cycling condition, with HT samples deteriorating at a faster rate than those subjected to the LT profile. This deterioration of HT SAC samples is evident in Figure 43 as significant weakening between 200 and 800 cycles. LT SAC samples from this plot do not undergo any significant strengthening or weakening trends and are shown to maintain relatively constant pull strength values over the duration of cycling. Cross sectional data gathered during passive thermal cycling indicated the growth of a very thick intermetallic layer at the surface mount lead / solder interface on HT samples between 0 and 100 cycles. Significant cracking between this intermetallic layer and the bulk solder joint was

observed in a subsequent cross section collected at 400 cycles. LT SAC samples did not mirror this intermetallic behavior and subsequently, did not crack during cycling. It is this disparity in SAC solder joint intermetallic growth and insipient cracking that is believed to have contributed significantly to the trend of the SAC pull strength data provided in Figure 43 and Figure 44.

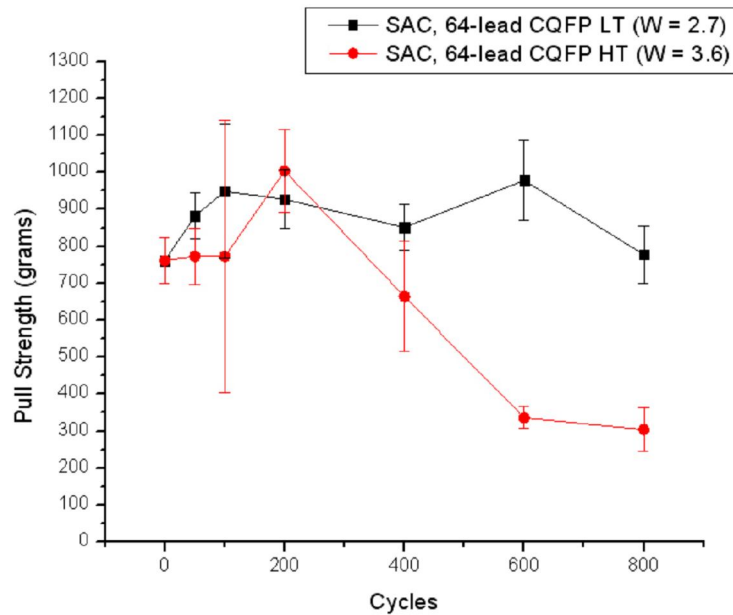


Figure 43. Pull strength trends of SAC, 64-lead CQFP samples.

The trend of 44-lead CQFP SAC samples provided in Figure 44 mirrors that of Figure 43 in that the pull strength of small package HT joints drops sharply to approximately half its original value within 200 cycles and then continues to decrease to almost one third of the baseline strength by the end of cycling. In both package sizes, the LT SAC samples are seen to be appreciably stronger than their HT counterparts at the conclusion of mechanical testing. This behavior correlates well with the physical cracking in HT SAC joints and the lack thereof in the LT SAC samples. It is also worth noting that the behavior of HT SAC pull strength appears to become

asymptotic at 600 cycles for the 64-lead CQFP and 400 cycles for the 44-lead CQFP. This trend suggests that intermetallic formation, which is self-limiting, had reached a point at which little additional intermetallic was forming with time at temperature. As such, the joints were no longer becoming increasingly brittle, which would then explain the decreasing rate of pull strength degradation observed in Figure 43 and Figure 44. Additionally, it is believed that severe cracking of the HT joints may have led to increased compliancy and resulted in an effective reduction in imposed strain energy density. It is possible that the asymptotic behavior observed is a combination of these two considerations occurring simultaneously.

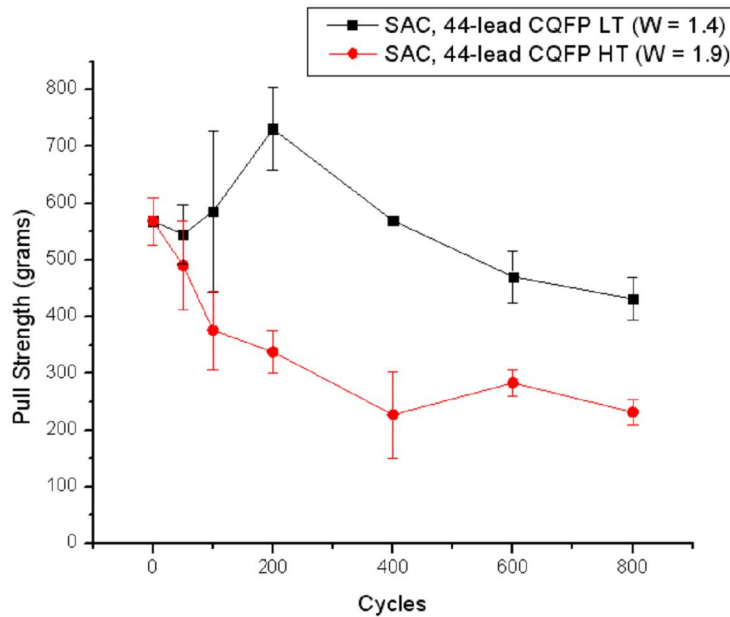


Figure 44. Pull strength trends of SAC, 44-lead CQFP samples.

In order to confirm the observed trends within the data using statistical methods, a one-way analysis of variance (ANOVA) was performed between the baseline and 800-cycle pull strengths for each of the estimated strain energy densities. This statistical test was intended to determine whether the solder joints mechanically tested

at the conclusion of passive thermal cycling were of a different population than those that were pull tested from the as-manufactured samples. The ANOVA was performed using the MATLAB function, `anova1`. Pull strength values of the baseline and 800-cycle solder joints were organized in separate columns of a matrix as required by the `anova1` function. The resulting MATLAB analysis output a p-value that indicated whether or not the two columns of data were of distinct populations based on the comparison of their means and variances; a p-value close to zero indicated that the means of the two data columns were significantly different than one another. Significantly differing means suggested that pull strength degradation due to cracking and/or intermetallic formation had occurred within the sample solder joints during passive thermal cycling. A common critical p-value of 0.01 was selected for the ANOVA of all solder materials; p-values lower than this threshold indicated that the sample means were significantly different while p-values higher than the critical value indicated similar sample means. The results of the ANOVA for the SAC305 samples are provided in Table 16. As the table shows, SAC305 samples subjected to HT cycling were characterized by p-values equal to zero. This result statistically validates the observation that significant pull strength degradation occurred within these samples as the ANOVA p-values reported were below the critical p-value of 0.01. SAC305 solder joints of the 44-lead CQFPs subjected to LT passive thermal cycling also featured a p-value indicative of pull strength degradation, however, this value suggests that the degradation was not as severe as that of the HT samples because it is non-zero. ANOVA of the SAC305 64-lead CQFP LT pull strength data resulted in a p-value of ~ 0.75 , which was well above the critical value of 0.01,

meaning that pull strength degradation did not occur within these samples. The non-zero p-values reported for the SAC305 LT samples stood in contrast to the p-values of zero for the HT samples. This behavior reflects the possibility that a temperature related degradation mechanism is responsible for the SAC pull strength trends.

Table 16. SAC305 ANOVA results.

		ΔW (lb/in ²)	ΔW (N/m ²)	$\Delta\gamma$	p-value
44-lead CQFP	LT	1.4	9650	0.119	0.00052
	HT	1.9	13100	0.140	0.00000
64-lead CQFP	LT	2.7	18615	0.142	0.75460
	HT	3.6	24820	0.167	0.00000

5.3.2 Eutectic Au-Sn Mechanical Results

The next solder material to be discussed regarding mechanical testing is eutectic Au-Sn. Similar to the failure mode observed in SAC305 samples, Au-Sn samples subjected to mechanical testing often failed along the surface mount lead / solder joint interface depicted in Figure 42. Although this interfacial failure was the dominant mode observed during testing, an alternative failure mode commonly referred to as pulling off the land [46] or pad lift was occasionally observed in failure of 44-CQFP solder joints. An illustration of this failure mode is provided in Figure 45. Clearly, when this type of failure occurs the strength of the solder joint is greater than the bonding strength between the copper pad and the PWB. It is hypothesized that the majority of pad lifts occurred in the 44-CQFP solder joint population because the surface mount pads for these packages were characterized by a cross-sectional area two-thirds that of the surface mount pads for the 64-lead CQFPs. This comparatively smaller footprint led to higher stresses at the pad / PWB interface which at times were high enough to exceed the adhesive strength of the pad to the PWB. An additional

feature causing this failure mode in Au-Sn joints may have been the higher temperature to which the PWBs were subjected during reflow, resulting in thermal damage of the board.

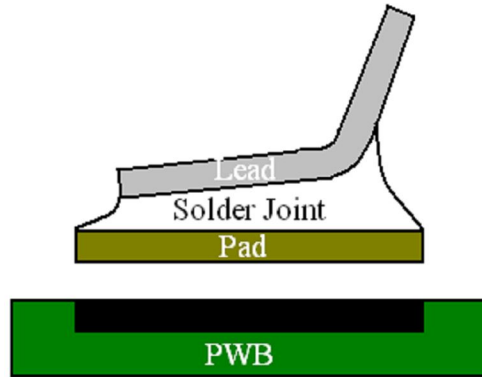


Figure 45. Pad lift failure mode during pull strength testing.

Those Au-Sn joints that failed through pad lift were removed from the population of mechanical test data. In particular, all Au-Sn joints on 44-lead CQFPs subjected to LT cycling sampled at 50 and 400 cycles failed through pad lift. It is for this reason that the discontinuity exists in Figure 46. As far as the trend of this plot is concerned, it is clear that the Au-Sn samples survived thermal cycling much better than the SAC samples from before. The plateaus formed by the pull strength trends of the 44-lead CQFP packages subject to either cycling condition are evidence that microstructure of the joints have stabilized and they remained largely undamaged up to the conclusion of testing. As expected, the joints subject to higher temperature and strain energy densities feature lower pull strengths than their counterparts, however, their final values remain very close to their baseline reading of ~800 grams force. It is likely that accelerated grain growth resulting from the additional temperature of the HT

cycle is responsible for the difference in final pull strengths. Further discussion of sample microstructure will be provided in the analysis of the cross section data.

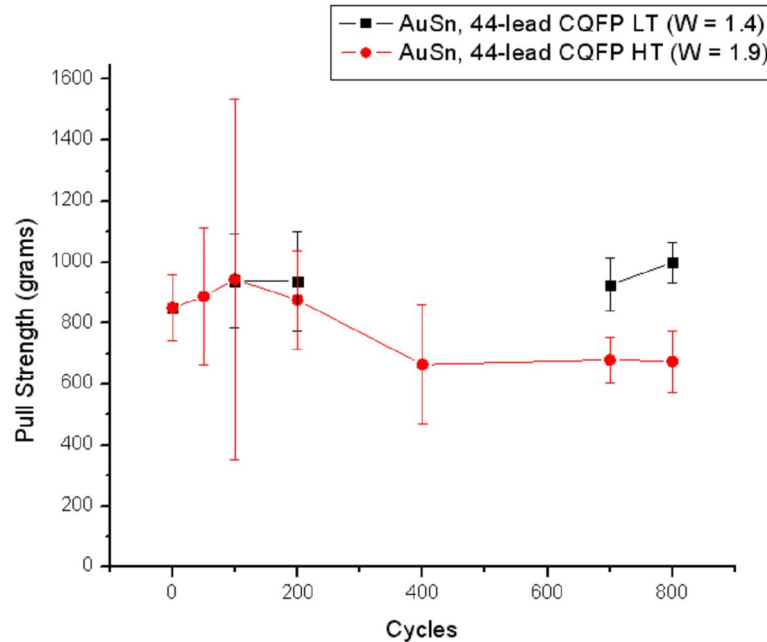


Figure 46. Pull strength trends of Au-Sn, 44-lead CQFP samples.

The pull strength trends of Au-Sn joints on 64-lead packages can be found in Figure 47 below. From the plot, it is clear that a significant readjustment occurs within the window of 0 to 50 cycles for samples subject to both cycling conditions. Following the readjustments experienced in the initial stages of cycling, both large package trends level out and achieve stable pull strengths over a span of 400 cycles prior to the conclusion of testing. This repeated plateau provides additional evidence of the material's excellent reliability with respect to the environmental testing performed during this investigation. This agreement of pull test data between package sizes suggests that evidence of solder joint fatigue will not be found during the cross sectional analysis of any of the Au-Sn joints. Furthermore, the nature of the alloy indicates there will be minimal interfacial intermetallic growth although

microstructural coarsening may be detected, as there is evidence of some initial change within solder joints sampled for the trends of Figure 47.

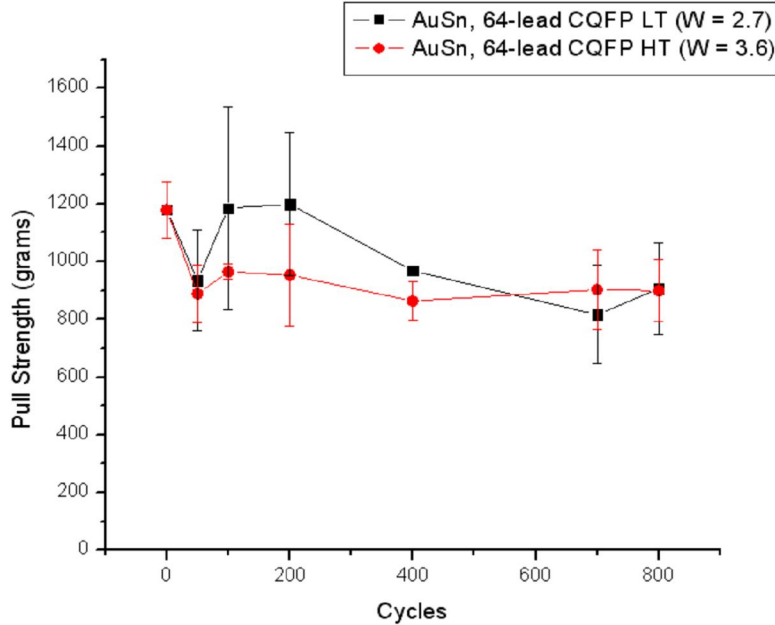


Figure 47. Pull strength trends of Au-Sn, 64-lead CQFP samples.

The ANOVA of the eutectic Au-Sn sample pull strength data was also performed as described by the prior SAC305 pull strength discussion. The p-values that resulted from the statistical analysis are provided in Table 17. As the table shows, all but one of the p-values were above the critical value of 0.01, therefore confirming the lack of pull strength degradation within the solder joints because the sample means of the as-manufactured and cycled joints were found to be statistically similar.

Table 17. Eutectic Au-Sn ANOVA results.

		ΔW (lb/in ²)	ΔW (N/m ²)	$\Delta\gamma$	p-value
44-lead CQFP	LT	1.4	9650	0.119	0.05740
	HT	1.9	13100	0.140	0.06040
64-lead CQFP	LT	2.7	18615	0.142	0.01640
	HT	3.6	24820	0.167	0.00580

5.3.3 Ag-In TLPS Mechanical Results

Having discussed testing of SAC305 and eutectic Au-Sn, the last of the solder materials to be treated within this section is Ag-In. Mechanical pull testing of Ag-In TLPS samples demonstrated that this material failed at the lead / solder joint interface, similar to joints from the SAC and Au-Sn populations. The location of the failure was likely due to the presence of brittle AuIn intermetallics formed at the interface by the reaction of the Au plating of the lead with In from the solder paste. However, at the moment of failure this material was observed to behave differently from the other solders. When samples from the SAC305 and eutectic Au-Sn populations failed, the solder joint remained intact and attached to the PWB as one might expect. In contrast to this behavior, when Ag-In TLPS joints failed, the toe of the solder joint would fracture and be ejected from the vicinity. This apparent brittle nature of the material may very well be characteristic of the compacts formed with TLPS, but it may also be related to the initial pull strength of the joints and/or the existence of cracking or delamination at the solder joint / surface mount pad interface.

The behavior of the pull strength trends in Figure 48 and Figure 49 are very similar to those discussed above. In both cases the solder joints subject to higher strain energy densities feature the lower of the two pull strengths at the conclusion of testing. Preliminary cross sections of the samples confirmed that cracking along the intermetallic layer formed at the interface between the solder joint and the lead existed within samples of all strain energy densities. It is hypothesized that this cracking is responsible for the pull strength trends below. At the conclusion of

mechanical testing at 400 thermal cycles, some Ag-In TLPS corner solder joints were severely cracked. It was for this reason in conjunction with sample quantity considerations that passive thermal cycling of the material was concluded at this point.

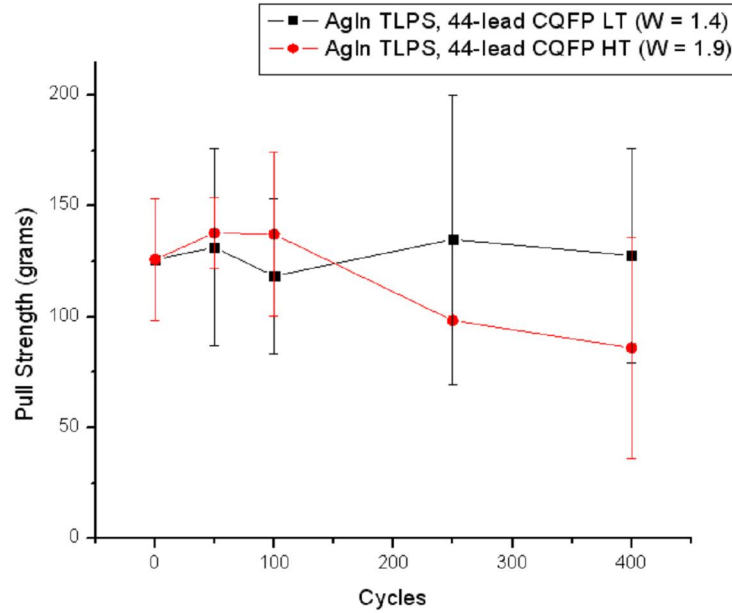


Figure 48. Pull strength trends of Ag-In TLPS, 44-lead CQFP samples.

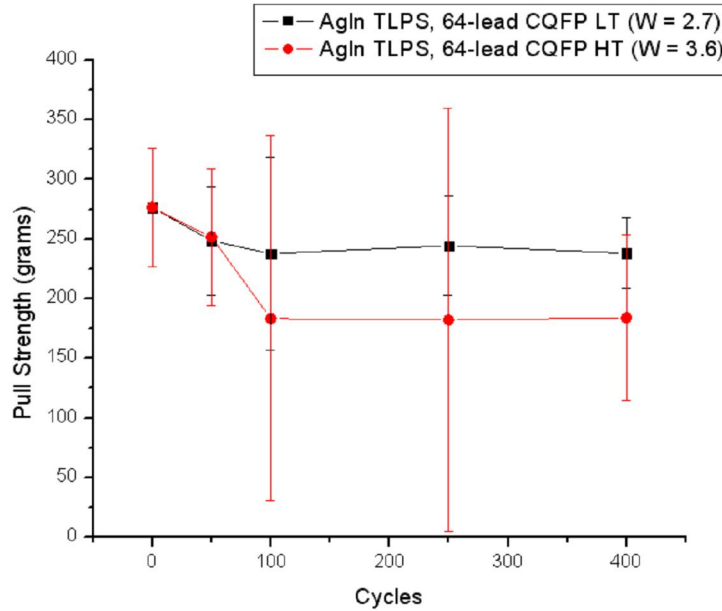


Figure 49. Pull strength trends of Ag-In TLPS, 64-lead CQFP samples.

As the pull strength trends of the Ag-In TLPS joints show, the variance of the mechanical data collected for this solder material is more significant than that of the SAC305 and Au-Sn solders due to smaller pull strength means. The ANOVA of the Ag-In TLPS was therefore an important tool in providing a quantitative assessment of any pull strength degradation. The results of this statistical analysis are displayed in Table 18. As the table shows, all p-values computed during the ANOVA are well above the critical value of 0.01. This result suggests the baseline and cycled pull strength samples for all strain energy densities are statistically similar, however, it is believed that the inherent variance of the pull strength data strongly influenced this outcome. This is most likely due to the fact that the site of crack initiation in the sample is the Au-In intermetallic, which is formed upon melting of the indium in the initial bonding step and does not grow with subsequent cycling because the Au is completely consumed in the initial bonding. This intermetallic formation results in a joint that is weak to start with, remains weak throughout, and features a wide variance in pull strength.

Table 18. Ag-In TLPS ANOVA results.

		ΔW (lb/in ²)	ΔW (N/m ²)	$\Delta\gamma$	p-value
44-lead CQFP	LT	1.4	9650	0.119	0.97880
	HT	1.9	13100	0.140	0.26560
64-lead CQFP	LT	2.7	18615	0.142	0.26590
	HT	3.6	24820	0.167	0.08360

In summary, mechanical pull strength testing of the various test assemblies provided valuable information regarding the health of the solder joints under passive thermal cycling. With respect to the SAC305 test assemblies, it was observed that HT cycling

led to significant losses in pull strength while samples subjected to LT cycling maintained noticeably higher strengths throughout the duration of the investigation. It has been proposed that intermetallic growth at the surface mount lead / solder joint interface under HT conditions is responsible for this behavior. Evidence of this intermetallic layer in addition to the localized cracking will be provided in the subsequent section. Although slight changes in the Au-Sn sample pull strength were observed, the material proved to maintain a high level of mechanical integrity and was regularly the strongest material for all strain energy density classifications. Provided that additional testing to these samples could be performed, it would be expected that well over 1000 thermal cycles would be required to weaken the joints to the levels observed for the SAC and Ag-In materials. In order to illustrate the relationship between the pull strengths of the various materials, Figure 50 has been prepared. As it shows, eutectic Au-Sn was consistently stronger than the other materials with SAC305 showing the greatest drop in strength with passive thermal cycling. The low strength of the Ag-In TLPS samples is believed to be due to the porosity of the material in conjunction with the presence of the brittle AuIn intermetallic layer at the lead / solder joint interface.

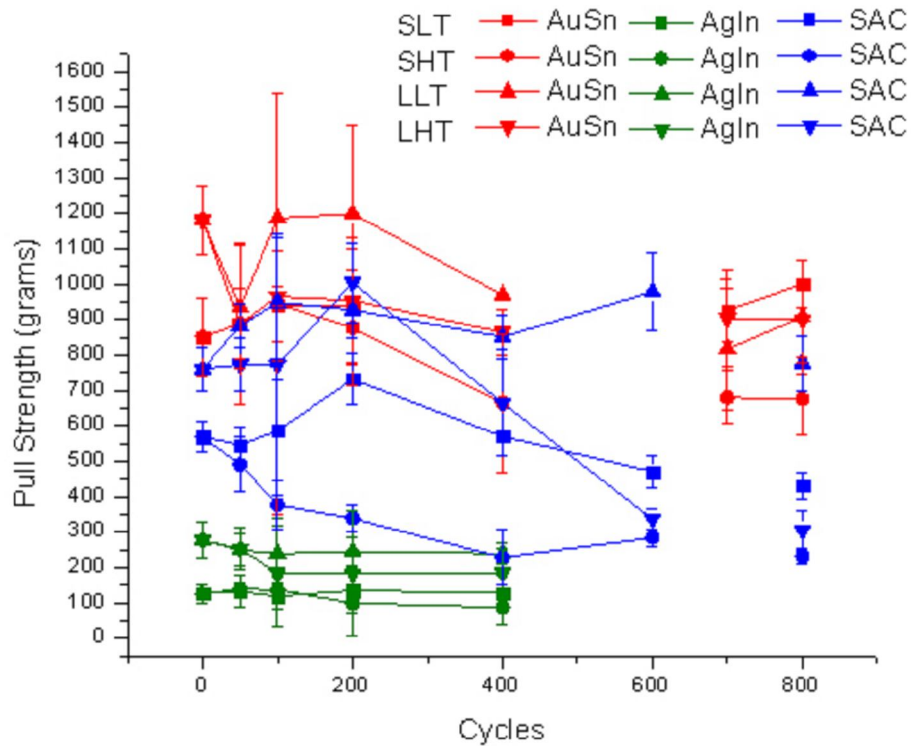


Figure 50. Comparison plot of solder material pull strengths.

5.4 Cross Sectional Data Trends and Discussions

Although monitoring the electrical continuity and mechanical strength trends of an electronics assembly is a common practice that yields valuable information about the health of the system, these methods still require microstructural data to correlate the observed behavior to physical phenomena. For this particular investigation, cross sections were collected from all test assemblies in an effort to provide qualitative microstructural data. As the corner solder joints of the surface mount packages were expected to be the first to fail, these were subjected to cross-sectioning and subsequent imaging. Due to the destructive nature of this data collection method, samples allotted for cross sectioning were designed into the mechanical testing

population. The sampling schedule for this investigation can be seen in Table 19 below.

Table 19. Observed cross section sampling schedule and sizes.

	Passive Thermal Cycles							
	0	50	100	200	400	600	700	800
Ag-In TLPS	1	-	1	-	5	-	-	-
Au-Sn	1	-	1	-	1	-	-	5
SAC305	1	-	1	-	1	-	-	5

As the table above shows, a single solder joint per solder per strain energy condition was collected until the final sampling period. The last sampling period for each solder material was supplemented with additional corner solder joints collected from the electrical test population for a total of 5 samples per solder per strain energy condition. These additional samples at the conclusion of thermal cycling were intended to ensure that physical observations were common to all sampled joints and therefore could be assumed to characterize the entire population. As expected, intermetallic layers at the lead / solder joint interface were found to relate to cracking in select SAC305 and Ag-In TLPS samples while those of Au-Sn remained largely unchanged by passive thermal cycling.

5.4.1 SAC305 Microstructural Results

With respect to the cross sections collected from SAC samples during this investigation, it was observed that for those test assemblies subjected to HT thermal cycling, a significant intermetallic layer rapidly formed between the lead and solder joint. However, SAC samples subjected to LT cycling did not exhibit such extreme intermetallic growth and therefore remained crack free for the duration of testing.

This behavior was predicted by the aforementioned mechanical data as HT joints were found to lose significant fractions of their baseline pull strengths while the LT joints maintained more consistent values. In the HT SAC samples the interface between the thick intermetallic and bulk solder joint then became the site of crack initiation and propagation. Figure 51 is an ESEM image of an as-built, 64-lead CQFP SAC solder joint. From inspection it is clear that the joint is healthy and any intermetallics at the two interfaces are not observable at the provided magnification.

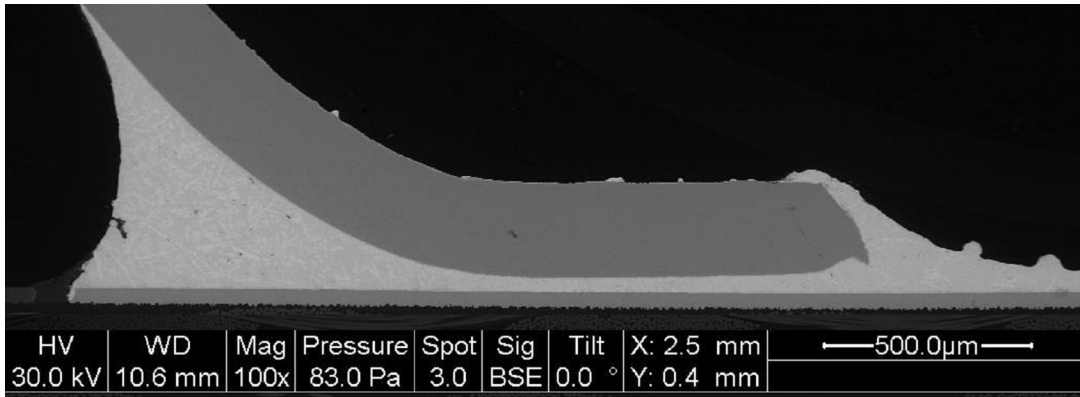


Figure 51. SAC305 64-lead CQFP joint subjected to 0 thermal cycles.

Figure 52 is the final sample collected from the SAC 64-lead CQFP population subjected to 800 LT thermal cycles. There is no evident deviation from the characteristics of the baseline sample shown in Figure 51. The joint is free from cracks and the intermetallic layers are thin and uniform. The image in Figure 53 of a SAC 64-lead CQFP joint subjected to 800 HT thermal cycles stands in contrast to the above observations. In this sample, cracking through the entire joint is easily seen in the ESEM image. In addition, it is clear that a thick, 2-phase intermetallic has formed between the lead and solder joint. The extent of this growth and characterization of the intermetallic will be discussed shortly. It is important to note that the

observations made for SAC joints of 64-lead CQFP packages were found to repeat in the 44-lead CQFP solder joints as well.

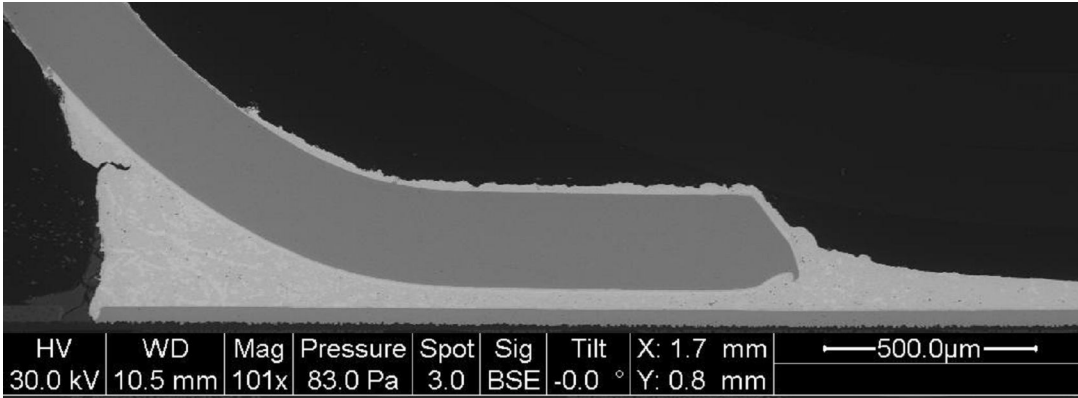


Figure 52. SAC305 64-lead CQFP joint subjected to 800 LT thermal cycles.

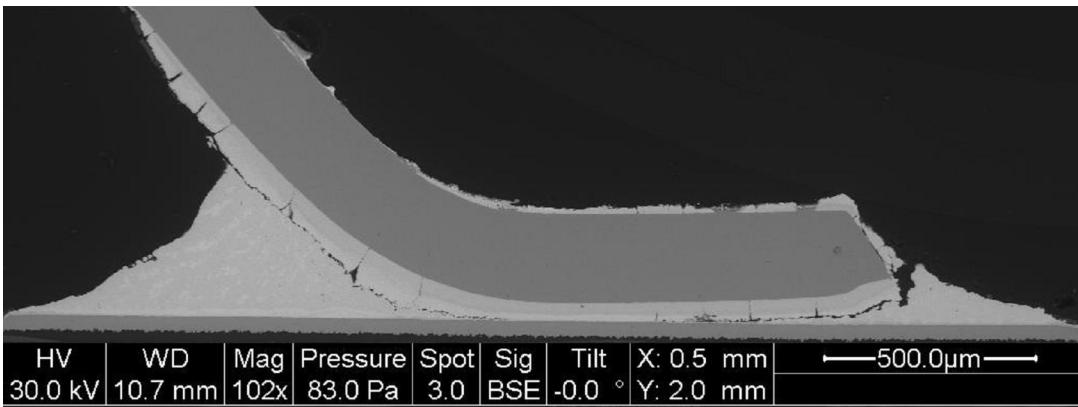


Figure 53. SAC305 64-lead CQFP joint subjected to 800 HT thermal cycles.

In both package sizes under HT conditions, growth of the intermetallic layer and subsequent cracking between it and the bulk solder were found to progress as a function of thermal cycling. At 100 cycles, the intermetallic layer was visible at ~100x magnification along with a number of cracks spanning the thickness of this layer (perpendicular to the surface of the lead). At 400 cycles, new cracks running parallel to the surface of the lead can be seen to begin splitting the intermetallic from the bulk solder. These parallel cracks can then be seen to complete run completely to

the edge of the solder heel and toe at the conclusion of testing (i.e. 800 cycles). It is important to note that while this cracking is occurring, the intermetallic layer is continually growing. An illustration of the previously described progression can be viewed in Figure 54 where the heels of 64-lead CQFP SAC joints subjected to HT cycling have been placed side-by-side to facilitate the comparison.

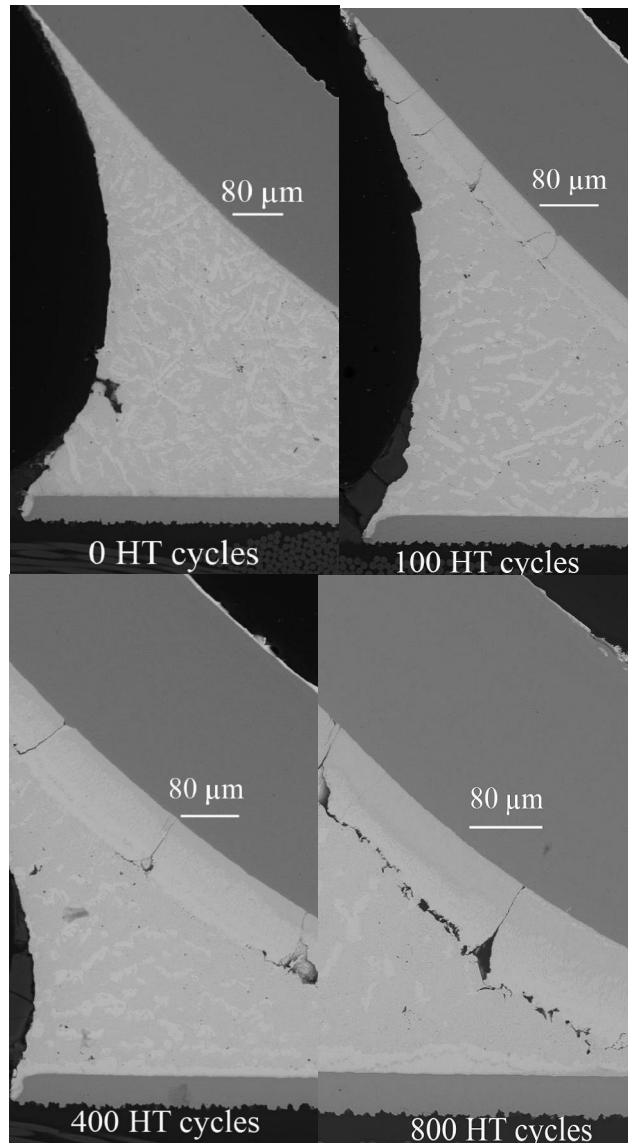


Figure 54. Intermetallic layer growth and crack progression in SAC 64-lead CQFP HT joints.

In an effort to characterize the apparent growth of the lead side intermetallic, its thickness was measured as a function of thermal cycles. Five independent measurements of the intermetallic thickness were collected per strain energy density per cycle count. These measurements were then averaged and plotted against the number of thermal cycles in Figure 55. As the plot clearly shows, the lead-side intermetallic layer grew monotonically with thermal cycles for all samples. It is of particular interest that the LT samples from both package sizes ended with intermetallic thicknesses of ~2.5 times their original value while HT samples from both package sizes showed an increase of ~10 times.

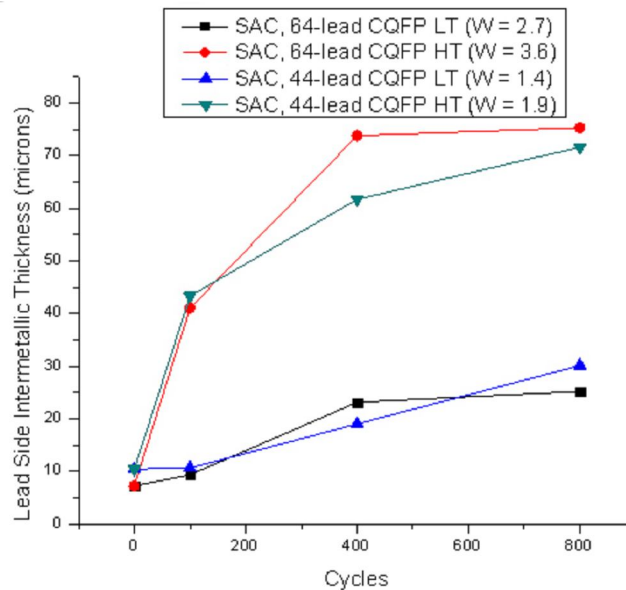


Figure 55. SAC lead side intermetallic thickness as a function of thermal cycles.

The trends from the above plot are consistent with the laws of diffusion as the higher temperature afforded by HT thermal cycling corresponds to thicker lead side intermetallics regardless of package size. In addition to tracking the growth of this intermetallic layer, efforts were made during this investigation to characterize its

composition as well. The layer was composed of two distinct compositions that contrast well under imaging with a standard light microscope. An image of a SAC 44-CQFP HT solder joint heel has been provided in Figure 56 in order to illustrate the difference between the layers. As it shows, a lighter composition can be found closest to the bulk solder joint while a distinctly different layer exists closer to the lead. In order to determine the compositional makeup of the two layers, the energy dispersive x-ray spectroscopy (EDS) function of the ESEM was required.

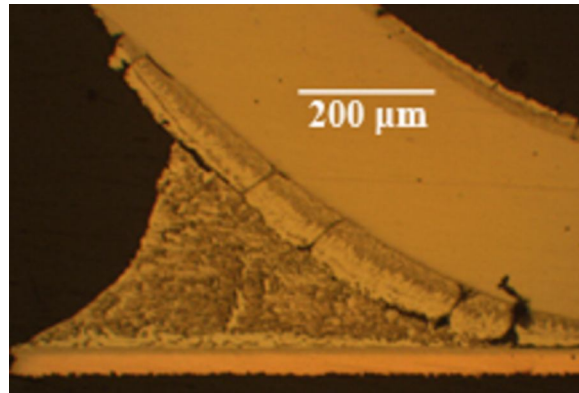


Figure 56. SAC305 44-lead CQFP HT solder joint heel imaged using light microscope.

An EDS map of the intermetallic layers demonstrated that they were composed largely of tin and nickel as shown by Figure 57. In this image the lead is located to the upper right while the solder can be found to the lower left of the intermetallic layer. These can be easily identified due to the increased levels of iron and nickel in the alloy 42 lead and increased levels of tin in the SAC solder. Next, an EDS point scan was conducted to quantify the ratios of the metallic constituents. The locations of the EDS point scans were targeted on two sites on either side of the compositional dividing line as shown in Figure 58.

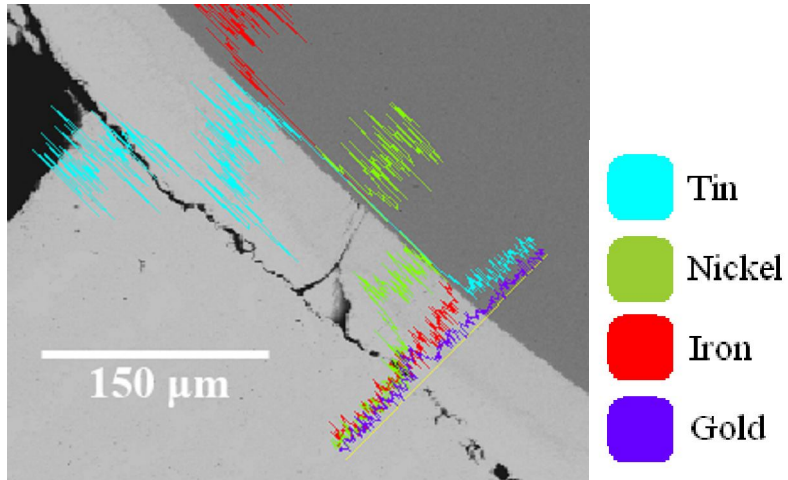


Figure 57. EDS Map of lead side intermetallic.

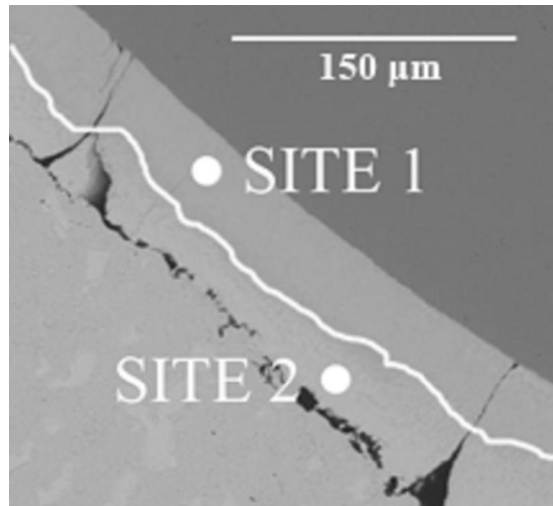


Figure 58. EDS Point Scan locations.

The resulting quantification of the metallic constituents at the scan sites above is provided in Table 20. As expected, the sample site located closer to the bulk solder is slightly more tin rich than that closer to the lead. Additionally, site 2 contains gold that was most likely dissolved from the lead plating during reflow. It is believed that the intermetallic represented by site 1 was the former location of the nickel metallization while the intermetallic of site 2 was the location of the immersion gold finish of the lead. The compositions of the intermetallics at site 1 and site 2 are believed to be NiSn_3 and $(\text{Ni,Au})\text{Sn}_3$, respectively.

Table 20. EDS point scan results of SAC intermetallic.

Metal	Site 1 (Atomic %)	Site 2 (Atomic %)
Tin (Sn)	68.41	75.8
Nickel (Ni)	25.11	11.9
Iron (Fe)	5.97	3.88
Gold (Au)	0.51	8.43

In summary, for those SAC305 test assemblies subjected to LT conditions, it was found that the solder joints survived testing without showing any signs of fatigue or excessive intermetallic growth. However, those SAC solders that experienced HT cycling rapidly developed thick intermetallic layers at the lead / solder interface that served as crack propagation sites in all samples that were observed. As previously described, the resulting cracks likely developed as perpendicular separations within the intermetallic that began to propagate along the bulk solder / intermetallic interface after initiation in a direction parallel to the bottom surface of the lead. Because of the swift formation of these intermetallics and their association with the observed damage to the SAC solder joints, it is recommended that this solder material be avoided for applications around 185°C and higher for similar test assembly material systems.

5.4.2 Eutectic Au-Sn Microstructural Results

In contrast to a number of changes observed within the SAC joints, those samples fabricated from eutectic Au-Sn were notably unaffected by the thermal cycling conducted for this investigation. Baseline Au-Sn solder joints were characterized by a lamellar structure consisting of a ζ - phase and δ - phase. Performing EDS on cross-sectioned samples in the ESEM quickly identified these compounds after cross-

referencing with a Au-Sn binary phase diagram. The results from the EDS point scan over the suspected phases are provided in Table 21 below.

Table 21. EDS point scan results of Au-Sn bulk solder.

	ζ' (Atomic %)	δ (Atomic %)
Gold (Au)	82.3	50.6
Tin (Sn)	17.7	49.4

The above atomic fractions reported from the EDS scan agree well with the data provided from the relevant portion of the Au-Sn binary phase diagram in Figure 59. As the diagram shows, the AuSn intermetallic, δ , lies at 50 at. % Sn while ζ' lies between 17 and 18 at. % Sn.

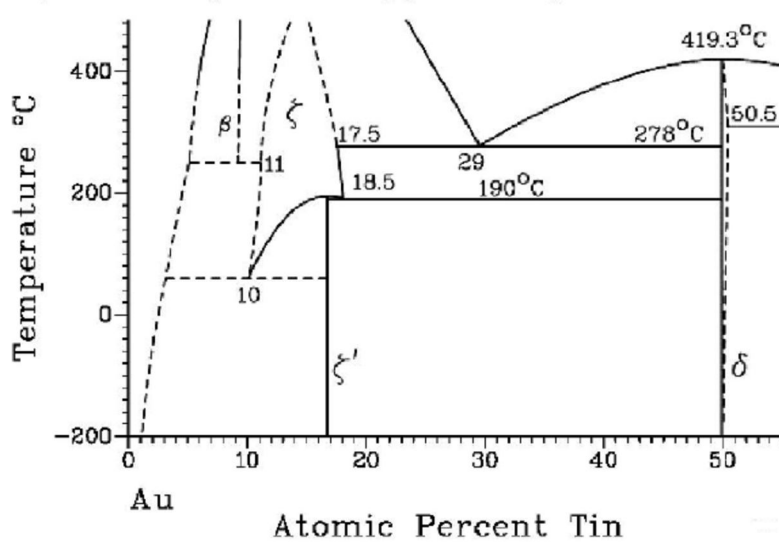


Figure 59. Truncated Au-Sn binary phase diagram [56].

The distributions of ζ' and δ can be viewed within an Au-Sn 64-lead CQFP LT solder joint in the image provided in Figure 60. The ζ' phase corresponds to the lighter shapes within the image due to its higher gold content that results in stronger backscatter signal within the ESEM. This particular microstructure is shown in the context of the solder joint in Figure 61. As this image demonstrates, the lamellar

structure dominates the bulk of the solder joint while larger areas of ζ' - phase are located along the lead and pad interfaces. Additionally, islands of the ζ' - phase were many times observed within the bulk of the Au-Sn solder joints, however, the distribution and concentration of these islands did not seem to form a pattern or trend over the cross-sectioned samples.

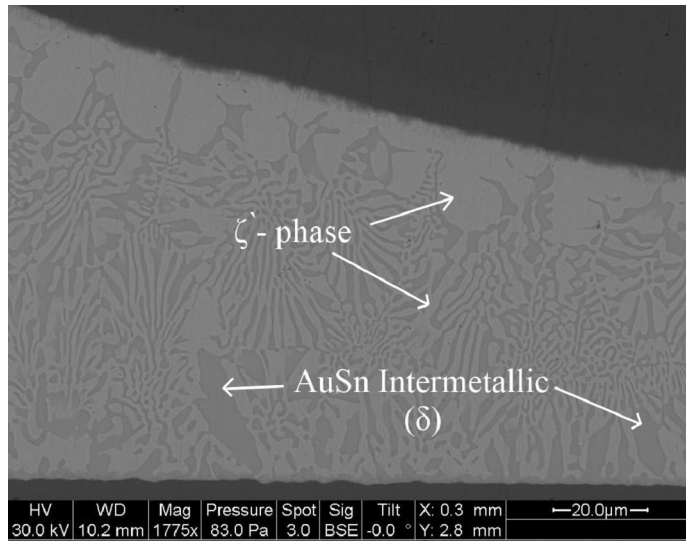


Figure 60. Phase distribution within eutectic Au-Sn solder joint.

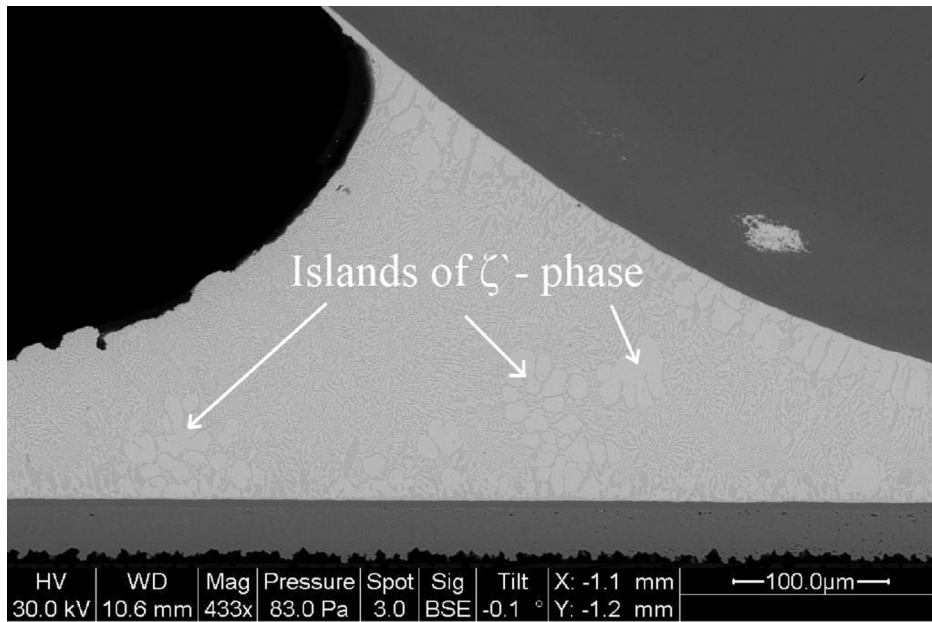


Figure 61. Solder joint heel of an Au-Sn 44-lead CQFP LT sample.

As previously mentioned, the microstructure observed in the as-built samples did not undergo any noticeable changes during passive thermal cycling. In addition, there was no evidence of crack initiation and propagation within any of the Au-Sn solder joints. In order to illustrate the exceptional health of these solder joints as a function of thermal cycling, the heels of the joints subjected to the highest strain energy density, those of the 64-lead CQFP HT test assemblies, are shown in Figure 62. As the series of images demonstrates, the Au-Sn solder joints remain free of cracks and any significant microstructural coarsening over the duration of passive thermal cycling. An additional feature from these images that warrants discussion is the existence of voiding within the Au-Sn solder joints. In order to quantify the frequency of voiding within the joints, the entire population of cross-section samples was assessed. During the assessment it was observed that approximately 50 percent of the Au-Sn solder joint population featured voiding. This voiding was distributed rather evenly over the population in that solder joints of large packages were just as likely or unlikely to be voided as those of small packages. Measurements of the void diameters showed that sizes ranged from the small 20 micron diameter voids typically located within the solder joint toe to very large 200 micron diameter voids located within the solder joint heel. Although voiding was found to affect a sizeable portion of the eutectic Au-Sn population, it was not observed to have had any influence on the reliability of the solder joints.

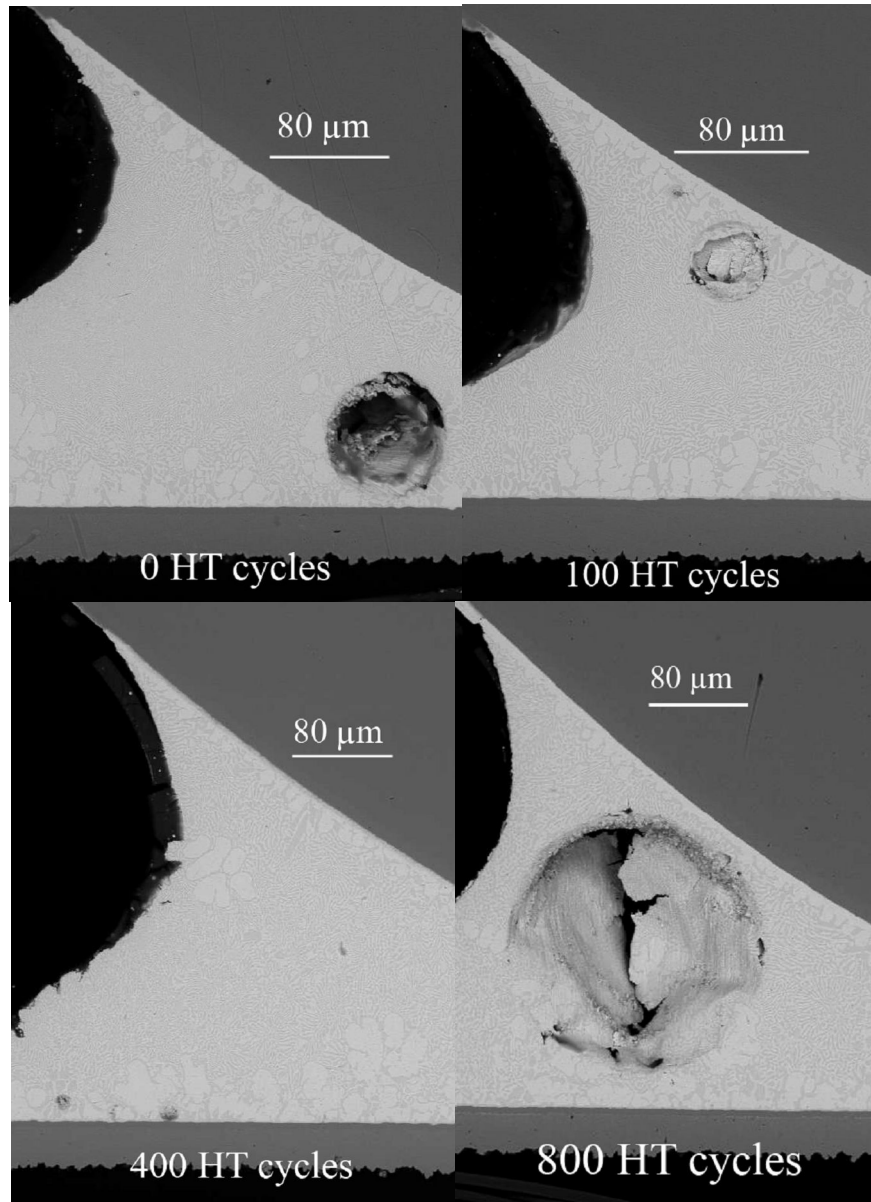


Figure 62. Lack of fatigue and microstructural coarsening in Au-Sn 64-lead CQFP HT solder joints.

Cross-sectional sampling of the eutectic Au-Sn solder joints demonstrated that the material is a highly desirable option for HT electronics as zero cracking was observed during passive thermal cycling. This high fatigue resistance coupled with its stable microstructure makes it an ideal choice when ENIG finished assemblies require a HT solder material. The observations made during the cross-sectional sampling correlate

well with the trends of the mechanical data in that both indicate few changes to the physical characteristics and behavior of the Au-Sn after 800 thermal cycles.

5.4.3 Ag-In TLPS Microstructural Results

With respect to the last of the three solder materials tested during this investigation, the Ag-In TLPS solder joints were found to form a lead-side intermetallic layer that later negatively influenced their reliabilities. This layer can be observed as the thin white line between the surface mount lead and the bulk solder joint within the as-built 64-lead CQFP Ag-In TLPS joint shown in Figure 63.

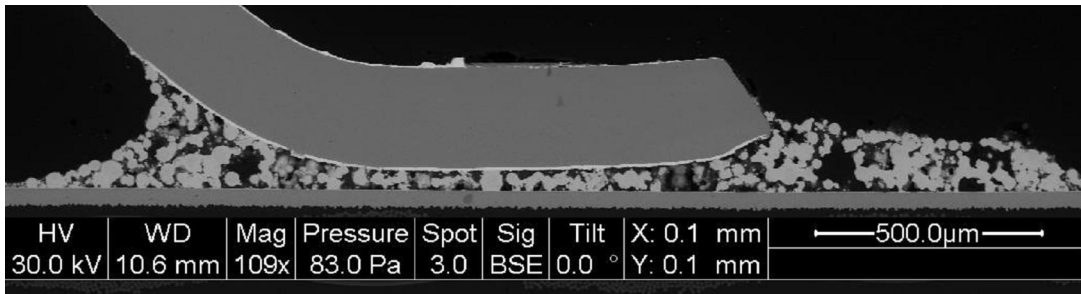


Figure 63. Ag-In TLPS 64-lead CQFP solder joint subjected to 0 thermal cycles.

In order to characterize the thickness of the intermetallic and its growth as a function of thermal cycling, the layer was monitored using the same approach previously described for SAC305: five thickness measurements were used to calculate an average thickness per strain energy per cycle count. These averages were then plotted as a function of cycle count in order to establish the growth trend. In the case of the Ag-In TLPS solder joint lead side intermetallic, the initial thickness formed during manufacturing of the joints remained largely unchanged during passive thermal cycling. This behavior can be observed from the plot in Figure 64 below.

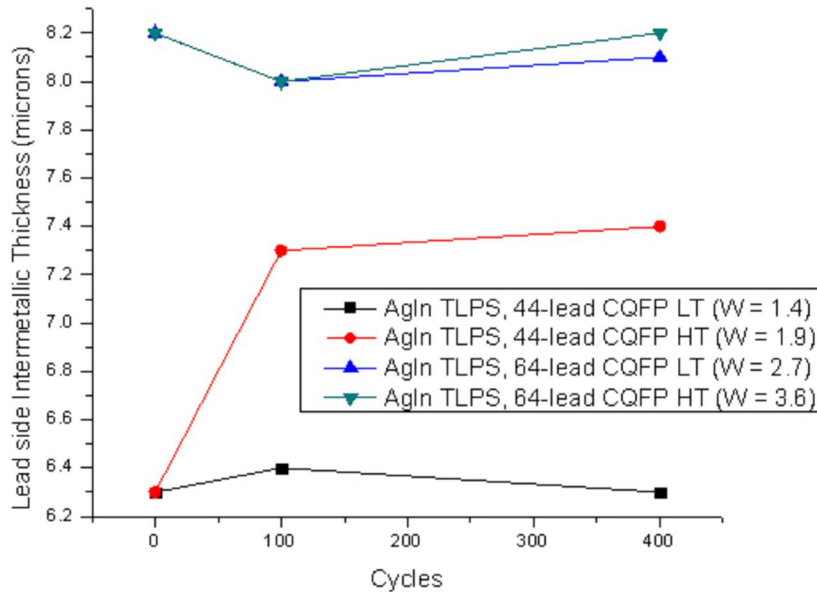


Figure 64. Ag-In TLPS lead side intermetallic thickness as a function of thermal cycles.

As the figure above shows, 3 of the 4 package size / cycling condition combinations remain constant while the Ag-In TLPS 44-lead CQFP HT solder joint intermetallic sees a small increase of ~1 micron or approximately 16 percent of its baseline thickness. The scale of these changes can be considered negligible when compared to those observed in the SAC samples: 1000% increase in baseline thickness for HT joints and a 250% increase for LT joints. In order to understand why the growth of the intermetallic occurs in this particular manner, it is helpful to know what metals compose the layer. EDS mapping and point scanning again determined the composition of the intermetallic layer, which was shown to contain the atomic composition of approximately 50 at. % Au and 50 at. % In. This composition corresponds to the AuIn intermetallic of the Au-In binary phase diagram displayed in Figure 65 below.

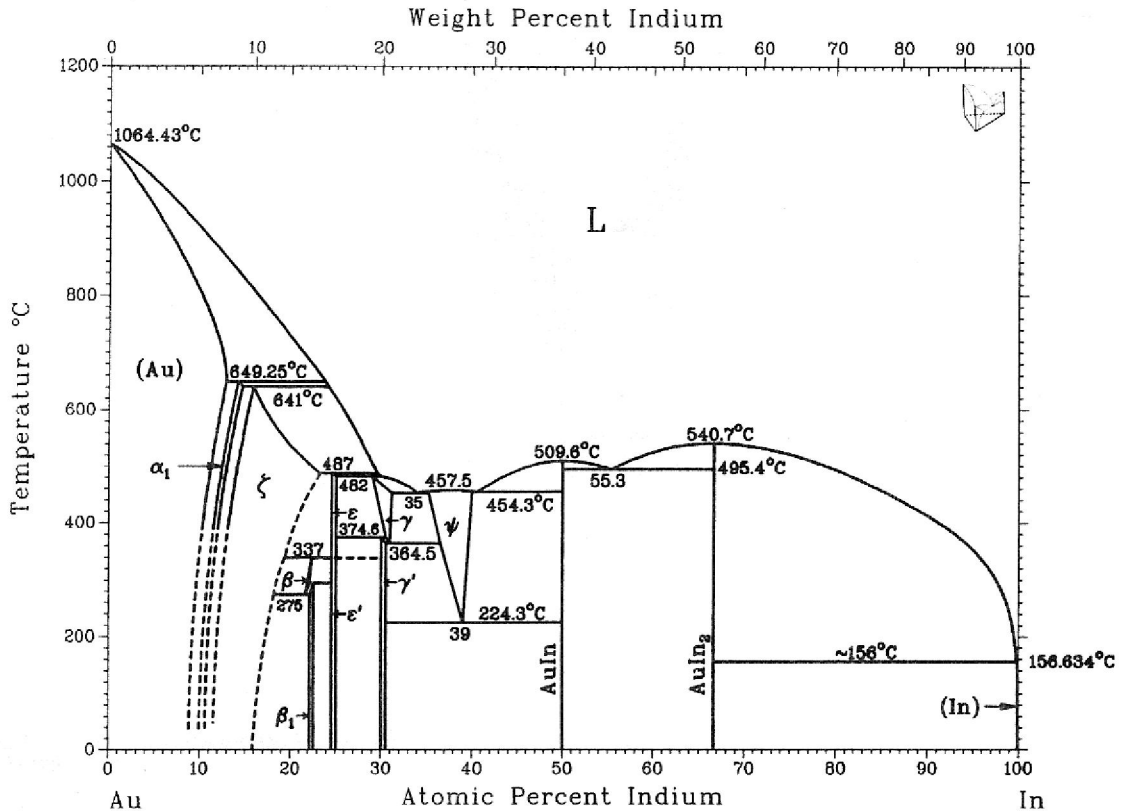


Figure 65. Au-In Binary Phase Diagram from [30].

With an understanding of the composition of the intermetallic layer at the lead side interface, the growth trends of this intermetallic can then be understood as a behavior limited by surrounding resources. In contrast to the intermetallics formed at the SAC305 lead side interface, those seen in the Ag-In TLPS can only be formed from the indium of the TLPS solder and the ~1.5 micron layer of gold coating the CQFP leads prior to processing. It is clear from the growth behavior displayed in Figure 64 that all available gold had been consumed and alloyed with indium during TLPS processing to form the AuIn intermetallic. Therefore, subsequent thermal cycling of the Ag-In TLPS test assemblies did not result in subsequent growth or decomposition of this layer.

As previously mentioned, passive thermal cycling of the Ag-In TLPS test assemblies resulted in cracking of the solder joints. For all strain energy densities, a significant portion of the cracking occurring in the joints was found along the interface between the AuIn intermetallic and the bulk solder joint composed of the Ag-In matrix. An illustration of this progressive cracking along the interface is provided in Figure 66.

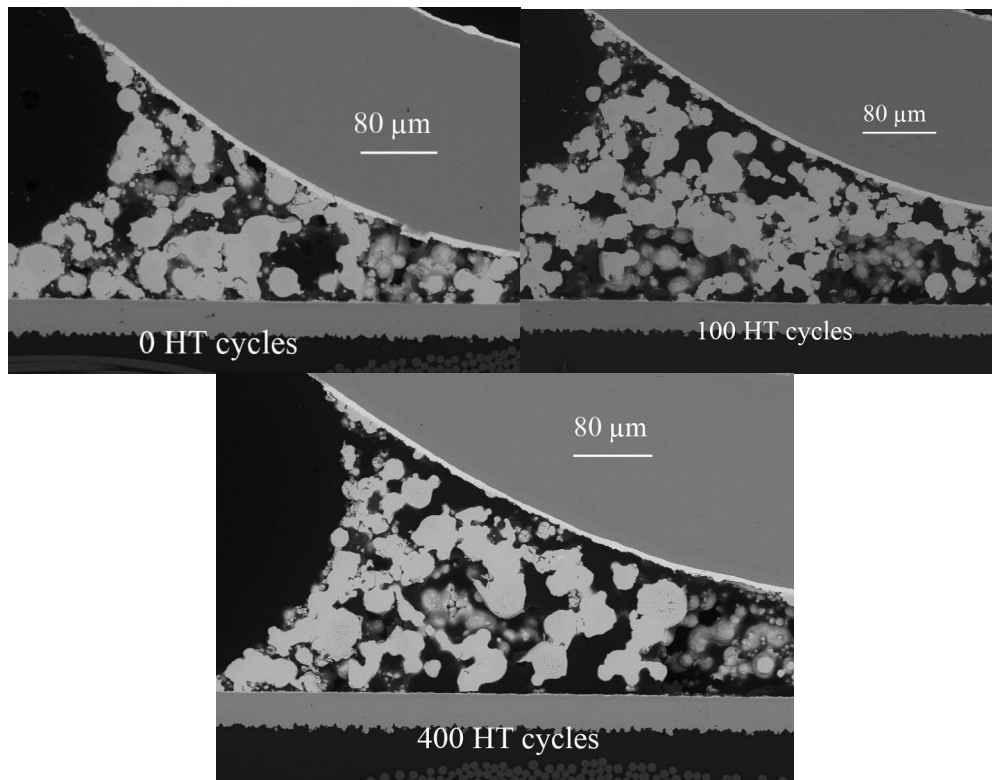


Figure 66. Crack progression in Ag-In TLPS 64-lead CQFP HT solder joints.

For this particular strain energy density, the heel of the solder joint has been completely removed from the lead at the conclusion of thermal cycling. Although cracks were largely located at the interface, they were seen moving into the bulk Ag-In matrix at times breaking the transient liquid sintered particles apart before returning to the interface between the intermetallic and the bulk matrix. This behavior is demonstrated by the selected image from an Ag-In TLPS 44-lead CQFP

HT solder joint (Figure 67) where the crack can be seen splitting through a small portion of the Ag-In bulk prior to reentering the intermetallic layer and terminating at the surface of the lead. This increasing crack length with cycling is believed to be the source of the observed mean pull strength degradation, although that degradation is not statistically significant owing to the already low force needed to cause cracking in as bonded samples.

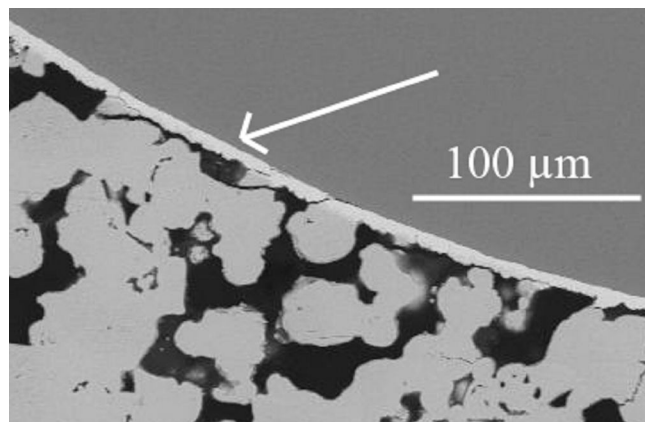


Figure 67. Cracking in Ag-In TLPS 44-lead CQFP HT solder joint subjected to 400 HT cycles.

In addition to the observed cracking of the Ag-In TLPS solder joints, passive thermal cycling of the test assemblies revealed interesting behavior regarding the cores of former silver particles within the Ag-In matrix. As passive thermal cycling progressed, the silver cores were seen becoming progressively roughened due to material loss resulting from the outward diffusion of silver into the Ag-In matrix. EDS maps were used to identify the former silver cores as seen in Figure 68. As the image shows, the Ag-In particles are characterized by a silver rich core while traveling out in a radial fashion results in an alloy increasing in indium content.

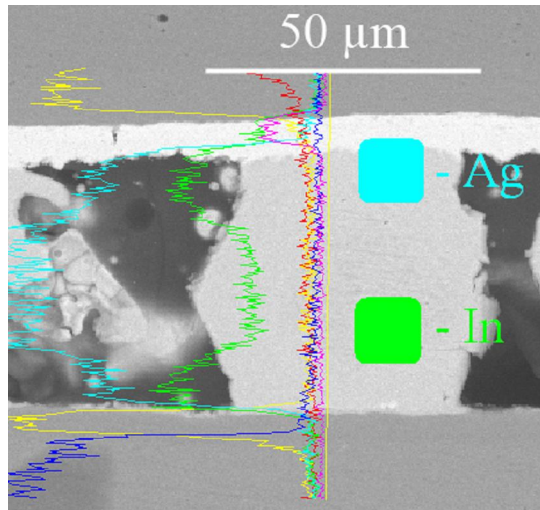


Figure 68. EDS map of Ag-In particle.

As previously mentioned, evidence of silver diffusion from the core of these Ag-In particles was observed as a function of passive thermal cycling. Figure 69 demonstrates this physical phenomenon through the pits that have formed at the center of the Ag-In particle subjected to 400 HT cycles.

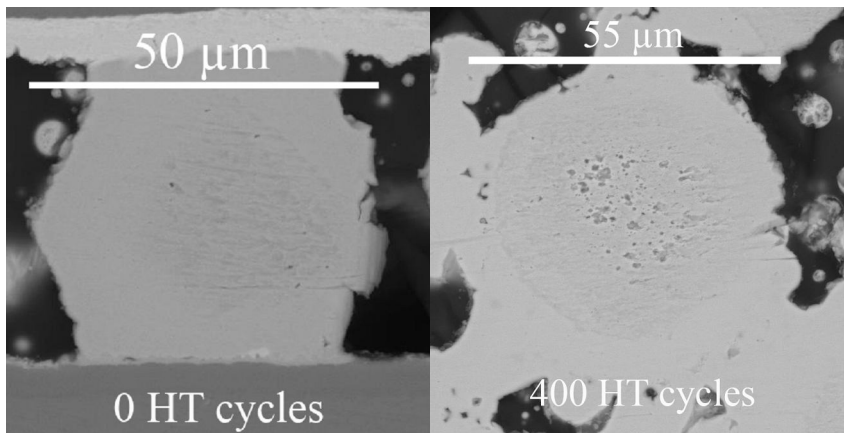


Figure 69. Evidence of silver diffusion from Ag-In particles within Ag-In TLPS matrix.

In summary, although cracking to the same extent as observed in the HT SAC samples did not occur within the Ag-In TLPS samples, the drop in already poor mechanical pull strength due to the aforementioned cracking within the heels for all package sizes combined with the material's brittle nature suggest that further work

with the potential HT solder and the best corresponding lead / board finishes is required to improve its reliability.

Chapter 6: Conclusions, Contributions, and Future Work

6.1 Conclusions

This thesis presents the relative reliabilities of SAC305, eutectic Au-Sn, and Ag-In TLPS solder joints subjected to HT passive thermal cycling. These solder materials were monitored for electrical resistance, mechanical pull strength, and microstructural changes as a function of thermal cycles.

In order to provide assemblies for testing, each of the solder materials was used as a part of a typical surface mount manufacturing process. SAC305 and eutectic Au-Sn manufacturing parameters were gleaned from the appropriate sources while fabrication with Ag-In TLPS required significantly more investigation and development. During development of the Ag-In TLPS paste, it was demonstrated that reducing the additive (indium) particle size led to statistically significant improvements in the volume fraction of the joints. Successful attachment of CQFPs to the PWB using Ag-In TLPS also demonstrated that surface mount joints with mechanical and electrical integrity could be manufactured from the material.

Subsequent testing of all solder samples demonstrated that for the given test vehicle metallization and cycling conditions, eutectic Au-Sn was the most reliable solder of the three. This solder material consistently exhibited the highest pull strength values at all strain energy densities over the duration of testing. Additionally, the stable microstructure of the Au-Sn joints as well as the lack of any cracking in them indicates that the solder material is the best suited for the HT testing that was

conducted. SAC305 samples subjected to the HT cycling profile (-55 to 185°C) were observed to grow significant Sn-based intermetallics between the surface mount lead and solder joint within a short period of time. These intermetallic layers were responsible for the extensive cracking observed in the SAC305 joints at the conclusion of cycling. SAC305 samples subjected to the LT cycling profile (-55 to 150°C) did not exhibit this rapid intermetallic growth and therefore survived to the conclusion of testing. In both cases, the mechanical pull strength reflected the microstructural characteristics of the cross section samples in that HT profile SAC samples experienced significant drops in mechanical strength while LT profile SAC samples maintained consistently higher strength values during cycling. Ag-In TLPS samples exhibited mechanical integrity during this investigation, however, it was consistently the weakest solder material of the three. Extensive cracking along the AuIn intermetallic formed at the lead interface was responsible for the observed weakening of the Ag-In TLPS pull strength. Experimentation with varying test vehicle metallizations and work on improving the brittle nature of the material are suggested as developmental tasks to advance this promising material.

Although significant solder joint cracking was observed in portions of the SAC305 and Ag-In TLPS populations, all solder samples tested for electrical resistance during this investigation maintained continuity throughout the duration of thermal cycling. This result agrees with the mechanical data because although degradation of pull strength was observed, all samples maintained some level of mechanical integrity at the conclusion of testing.

6.2 Contributions

The major contributions provided by this work are as follows:

- The first implementation of Ag-In TLPS as a surface mount component attach
- The first study of indium particle size on Ag-In TLPS solder joint density
- The first characterization of Ag-In TLPS as a function of passive thermal cycling and subsequent comparison against a baseline HT solder material (eutectic Au-Sn) and commercial solder material (SAC305).
- The first study of SAC305 at 185°C on alloy 42.

6.3 Future Work

The following are suggestions for future work:

- Implementation of Ag-In TLPS on silver finished test assemblies to assess reliability without AuIn intermetallics observed during this study.
- Further optimization of the Ag-In TLPS paste to improve joint density.

Appendix A – MATLAB Lead Compliance Formulas

MATLAB code utilizing the Lead Compliance Formulas for the Inclined Gull-Wing Lead Structural Model from [49].

```
clear all
clc

%GEOMETRIES
%side view
%H = .762*(40/1000);
L1 = 8/1000;
L2 = 55/1000;
L3 = 0/1000;
L4 = 0/1000;
R1 = 30/1000;
R2 = 12/1000;
%X = .549*(40/1000);
alpha = 0;% atan(X/H); in RADIANS!
H = (R1+R2)*(1-sin(alpha))+(L1+L2)*cos(alpha)
Curv = L1+L2+L3+L4+(R1+R2)*(1.5708-alpha)
%cross-section view
l = 15/1000;
w = 8/1000;

l2 = 27/1000;
w2 = 8/1000;

%PRE-DEFINED CONSTANTS
C1 = H-R2;
C2 = .7854-(alpha/2)+(1/4)*sin(2*alpha);
C3 = .7854-(alpha/2)-(1/4)*sin(2*alpha);
C4 = L4*sin(alpha)+R1*cos(alpha);
C5 = L4*cos(alpha)+R1*(1-sin(alpha));
C6 = (L1+L2)*sin(alpha)+(R1+R2)*cos(alpha)+L4;

%ADDITIONAL PARAMETERS
f = 1.20;
A1 = l*w;
%A2 = A1;
A2 = l2*w2;

I1 = (l*w^3)/12;
%I2 = I1;
I2 = (l2*w2^3)/12;
```

```

I3 = (w*l^3)/12;
%I4 = I3;
I4 = (w2*l2^3)/12;

%E = 20.6*10^6; %(Alloy 42)
E = 17.5*10^6; %(Cu Alloy) lbf/in^2
%G = 7.92*10^6 %(Alloy 42)
G = 6.6*10^6; %(Cu Alloy) lbf/in^2

n1 = .65;
beta1 = .141+.088*(l/w-1)^n1
n2 = .47;
beta2 = .141+.088*(l2/w2-1)^n2
T1 = (1/12)*(1/beta1)*(l/w)^2*(E/G);
%T2 = T1;
T2 = (1/12)*(1/beta2)*(l2/w2)^2*(E/G);

%Flexural stiffness in x-direction
S1 = (1/3)*L1^3*(cos(alpha))^2+R1*L1*(1-sin(alpha))*(L1*cos(alpha)+R1*(1-
sin(alpha)))...
+R1^3*(2.3562-1.5*alpha-2*cos(alpha)+(1/4)*sin(2*alpha));

S2 = H^2*L3+(1/3)*L2^3*(cos(alpha))^2+L2*(R1*(1-
sin(alpha))+L1*cos(alpha))^2+R2*(C1^2*(1.5708-alpha)...
+2*C1*R2*cos(alpha)+C2*R2^2)+L2^2*cos(alpha)*(R1*(1-
sin(alpha))+L1*cos(alpha));

S11 = L4+R1*C2+L1*(sin(alpha))^2+f*(E/G)*(R1*C3+L1*(cos(alpha))^2);

S12 = L3+R2*C2+L2*(sin(alpha))^2+f*(E/G)*(R2*C3+L2*(cos(alpha))^2);

Kx = 1/(((1/E)*((S1/I1)+(S2/I2)))+((1/E)*((S11/A1)+(S12/A2))))

%Flexural stiffness in y-direction

S3 = (1/3)*(L4^3+(C4+L1)^3-
C4^3)+R1*(R1^2*C3+R1*L4*(cos(alpha))^2+L4^2*C2)...
+T1*(L1*C5^2+R1*(L4^2*C3+R1*L4*(1-sin(alpha))^2)...
+R1^3*(1.5708-alpha-2*cos(alpha)+C2));

S4 = (1/3)*((L1+L2)^3-L1^3+(C6+L3)^3-C6^3)+C4*(C4*L2+L2^2+2*L1*L2)...
+R2*((C1^2+C6^2)*(.7854-alpha/2)+(1/4)*(C6^2-
C1^2)*sin(2*alpha)+C1*C6*(cos(alpha))^2)...
+T2*(C5^2*L2+H^2*L3+R2*((C1^2+C6^2)*(.7854-
alpha/2)+(1/4)*sin(2*alpha)*(C1^2-C6^2))...

```

$-2*C6*R2*(1-\sin(\alpha))+C1*\cos(\alpha)*(2*R2-C6*\cos(\alpha))+R2^2*(1.5708-\alpha));$

$S13 = f*(E/G)*(L1+L4+R1*(1.5708-\alpha));$

$S14 = f*(E/G)*(L2+L3+R2*(1.5708-\alpha));$

$Ky = 1/(((1/E)*((S3/I3)+(S4/I4)))+(1/E)*((S13/A1)+(S14/A2))))$

%DIAGONAL FLEXURAL STIFFNESS

Lpack = .9;

Wpack = .9;

r = Lpack/Wpack;

$Kd = (1.414*Kx*Ky)/(\text{sqrt}(Kx^2+Ky^2))$

Appendix B – MATLAB codes for Electrical Data Analysis

Thermal Cycle Tagging Code

This code was created in order to apply cycle counts to the input data. Raw data from the data logger array came only with time stamps. Based on the collected temperature probe readings from the raw data, this program provided a data stamp with the cycle number of the resistance readings.

```
clear all
clc

% This part of the program is used to tag the data from the loggers with a
% the correct number of passive cycles experienced by the solder joints

[NUMERIC,TXT,RAW]=XLSREAD('G:\Research\Thesis Materials\The REAL
Deal\450 to 500 cycles AuSn and SAC305\Datalogger 3\Data INSTR 3 7_7_2008
15_44_57 3_tabs'...
,'Data INSTR 3 7_7_2008 15_44_57 ','ak45:ak5400');

[m,n]=size(NUMERIC);
count = zeros(1,m);
count(1)=1;
tot_cycle=1; %this sets a cycle counter that displays the cycle BEING completed...
             %not the cycle that HAS BEEN completed!
thres=85; %difference that needs to be exceeded between true cycle counts (this...
          %is the number of counts that occur between true full cycles...
          %for example, a cycle that takes 90 min long sampled every 10
          %seconds would require a threshold of approx. 540
          %(90min*(60sec/1min)*(1sample/10sec)=540samples
for i=1:m
    [Y1,I1]=max(count);
    if NUMERIC(i)>=45 & NUMERIC(i)<=55 & (i-I1)>thres
        count(i)=1;
        count(I1)=0;
        tot_cycle=1+tot_cycle;
    end
    cycle(i)=tot_cycle;
end

A = [NUMERIC, cycle'];
cycles = cycle';

num2clip(cycles)
tot_cycle
```

Automatic Resistance Signature Plotting Code

This code was created in an effort to simplify the characterization of electrical chain resistance signatures. The plots automatically generated and saved by this code provided snapshots of resistance signatures that could be quickly looked over for abnormal behavior. The creation of this code greatly facilitated work with electrical data during this investigation.

```
clear all
clc
```

```
[A,TXT,RAW]=XLSREAD('C:\Documents and Settings\toberc\My
Documents\Research\The REAL Deal\400-405 cycles P4, 800-810 cycles ELEC
Scruff\McGruff\is\the\coolest\dog\that\ever\has\lived\what\a\terrific\terrier!\
SAC (Data Salvaging)\DL4\Data INSTR 4 9_27_2008 16_14_46 4_tabs'...
    , 'Data INSTR 4 9_27_2008 16_14_46', 'd74:bo1349');
```

```
[m n] = size(A);
x = linspace(1,m,m);
```

```
for i=1:n
    max1 = max(A(:,i));
    min1 = min(A(:,i));
    plot(x,A(:,i))
    hold on
    if min1 > 0
        axis([0 m 0 max1])
    hold off
    else
        axis([0 m min1 max1])
    hold off
    end
    % ...
    filename=['C:\Documents and Settings\toberc\My Documents\Research\The REAL
Deal\400-405 cycles P4, 800-810 cycles ELEC SAC (Data Salvaging)\Figures\DL4\-'
0' num2str(i) '.bmp'];
    saveas(gcf,filename,'bmp');
end
```

```
%saveas(gcf, 'G:\Oberc\Matlab Files\Figures\'num2str(i), 'bmp')
```

Works Cited

- [1] "Performance Test Methods and Qualification Requirements for Surface Mount Solder Attachments." IPC-9701, Jan. 2002, pp. 13-14.
- [2] R. Kirschman, "Extreme Temperature Electronics." October 2008. Available: <http://www.extremetemperatureelectronics.com/index.html>.
- [3] P. Neudeck, D. Spry, G. Beheim, and R. Okojie, "6H-SiC Transistor Integrated Circuits Demonstrating Prolonged Operation at 500°C," Proceedings of International Conference on High Temperature Electronics, Albuquerque, NM, May 12-15, 2008.
- [4] M. Levinshtein, et al., "High-temperature (up to 773K) operation of 6-kV 4H-SiC junction diodes." Solid-State Electronics 49: no. 7, July 2005, pp. 1228-1232.
- [5] F. McCluskey, R. Grzybowski, and T. Podlesak, "High Temperature Electronics." CRC Press: Boca Raton, 1997, p. 9
- [6] R. German, "Liquid Phase Sintering." Plenum Press: New York, 1985, p.164.
- [7] US provisional patent serial number: US60/891,763; "Ag-In Transient Liquid Phase High Temperature Solder Paste Attach." Patent filed January, 2008.
- [8] P. Quintero, "Development of a Shifting Melting Point Ag-In Paste Via Transient Liquid Phase Sintering for High Temperature Environments." University of Maryland, PhD Thesis, 2008.
- [9] A. Choubey, et al., "Lead-Free Assemblies for High Temperature Applications." Proceeding of IMAPS International Conference on High Temperature Electronics (HITECH 2006), May 2006, pp. 384-389.
- [10] A. Choubey, et al., "Intermetallics Characterization of Lead-free Solder Joints under Isothermal Aging." Journal of Electronic Materials: Vol. 37, No. 8, August 2008, pp. 1130-1138.
- [11] A. Choubey, et al., "Effect of Aging on Pull Strength of SnPb, SnAgCu, and Mixed Solder Joints in Peripheral Surface Mount Components." University of Maryland CALCE Center, Internal Research Paper. 2007.
- [12] I. Kim, et al., "A Comparative Study of The Fatigue Behavior of SnAgCu and SnPb Solder Joints." Key Engineering Materials: Vols. 297-300, 2005, pp. 831-836.
- [13] J. Suhling, et al., "Thermal cycling reliability of lead free solders for automotive applications." The Ninth Intersociety Conference on Thermal and Thermomechanical Phenomena in Electronic Systems. Vol.2, 2004, pp. 350-357.

- [14] H. Ma, et al., "Reliability of the aging lead free solder joint." 2006 Proceedings 56th Electronic Components & Technology Conference. June 2006, p. 849 – 864
- [15] W. Brown and R. Ulrich, eds. Advanced Electronic Packaging. IEEE Press Series on Microelectronic Systems. A John Wiley & Sons, Inc: Piscataway, NJ. 2006.
- [16] M. Ishikawa, et al., "Application of Gold-Tin Solder Paste for Fine Parts and Devices." 2005 Proceedings of 55th Electronic Components and Technology Conference. June 2005, p. 701-709.
- [17] C. Lee and G. Matijasevic. "Highly reliable die-attachment on polished GaAs surfaces using gold-tin eutectic alloy." IEEE Transactions on Components, Hybrids, and Manufacturing Technology: Vol. 12, No. 3, Sept. 1989.
- [18] G. Matijasevic and C. Lee, "Void-free Au-Sn eutectic bonding of GaAs dice and its characterization using scanning acoustic microscopy." Journal of Electronic Materials: Vol. 18, No. 2, Mar. 1989, p. 327-337.
- [19] G. Matijasevic, C. Wang, and C. Lee, "Void Free Bonding of Large Silicon Dice Using Gold-Tin Alloys." IEEE Transactions on Component, Hybrids, and Manufacturing Technology, Vol. 13, No. 4, Dec. 1990, p. 1128-1134.
- [20] K. Hungar and W. Mokwa, "Gold/tin soldering of flexible silicon chips onto polymer tapes." Journal of Micromechanics and Microengineering: Vol. 18, June 2008.
- [21] X. Qiao and S. Corbin, "Development of Transient Liquid Phase Sintered (TLPS) Sn-Bi Solder Pastes." Materials Science and Engineering A: Vol. 283, 2000, p. 38-45.
- [22] S. Corbin, "High Temperature Variable Melting Point Sn-Sb Lead-free Solder Pastes using Transient Liquid Phase Powder Processing." Journal of Electronic Materials: Vol. 34, 2005, p. 1016-1025.
- [23] M. Palmer, N. Erdman, and D. McCall, "Forming high temperature solder joints through liquid phase sintering of solder paste." Journal of Electronic Materials: Vol. 28, No. 11, 1999.
- [24] C. Gallagher, G. Matijasevic, and J. Maguire, "Transient Liquid Phase Sintering Conductive Adhesives as Solder Replacements." Electronic Components and Technology Conference: 1997.
- [25] C. Shearer, B. Shearer, G. Matijasevic, and P. Gandhi, "Transient Liquid Phase Sintering Composites: Polymer Adhesives with Metallurgical Bonds." Journal of Electronic Materials: Vol. 28, No. 11, 1999.

- [26] C. Lee and W. So, "High temperature silver-indium joints manufactured at low temperatures." *Thin Solid Films*: 366, 2000, p. 196-201.
- [27] R. Chuang and C. Lee, "Silver-Indium Joints Produced at Low Temperature for High Temperature Devices." *IEEE Transactions on Components and Packaging Technologies*: Vol. 25, No. 3, Sept. 2002.
- [28] R. German and J. Dunlap, "Processing of Iron-Titanium Powder Mixtures by Transient Liquid Phase Sintering." *Metallurgical Transactions A*: Vol. 17A, Feb. 1986, p. 205-13.
- [29] M. Hou and T. Eagar, "Low Temperature Transient Liquid Phase (LTTLP) Bonding for Au/Cu and Cu/Cu Interconnections." *Journal of Electronic Packaging*: Vol. 114, Dec. 1992, p. 443-47.
- [30] M. Hansen and K. Anderko. *Constitution of Binary Alloys*, McGraw-Hill, New York, 1958.
- [31] G. Vander Voort, "Metallography, Principles and Practice." ASM International: Ohio, 1999.
- [32] Point-counting Technique. ASTM Specification E562.
- [33] "ImageJ Analyze Menu." Image J: Image Processing and Analysis in Java. 2008. Available: <http://rsbweb.nih.gov/ij/docs/menus/analyze.html>.
- [34] J. Johnson, J. Brezovsky, and R. German, "Effects of Tungsten Particle Size and Copper Content on Densification of Liquid-Phase-Sintered W-Cu." *Metallurgical and Materials Transactions A*: Vol. 36A, Oct. 2005, p. 2807-14.
- [35] B. Rabin and R. Wright, "Synthesis of Iron Aluminides from Elemental Powders: Reaction Mechanisms and Densification Behavior." *Metallurgical Transactions A*: Vol. 22A, Feb. 1991, p. 277-86.
- [36] "Process Change Notification PCN072 Update." Altera Corporation. Available: <http://www.altera.com/literature/pcn/pcn0702.pdf>. p. 6.
- [37] "EnviroMark 907 Lead-Free No-clean Solder Paste." Kester Product Data Sheet.
- [38] C. Harper. *Electronic Packaging and Interconnection Handbook*. McGraw-Hill Professional, 2004. ISBN 0071430482. Chap 5, p. 26.
- [39] "NC-SMQ51SC Solder Paste." Indium Corporation of America Data Sheet.

- [40] "Eutectic Gold-Tin Solder Paste." Indium Corporation of America Data Sheet.
- [41] "Stencil Design Guidelines." IPC-7525: May 2000.
- [42] Omega LMF-3550 Product Manual. Accessed 2008. Available: <http://omega.com/manuals/manualpdf/M2159.pdf>. p. 43.
- [43] "EC12 Product Manual." Sun Electronics.
- [44] "Guideline for Accelerated Reliability Testing of Surface Mount Solder Attachments." IPC-SM-785: Nov. 1992, p. 33.
- [45] R. Abernethy, "The New Weibull Handbook 3rd Edition." 1998. p. 31.
- [46] "Environmental and Endurance Test Methods for Surface Mount Solder Joint: Pull Strength Test." IEC 91/579/CDV: Jan. 2006.
- [47] J. Clech and J. Augis, "Surface Mount Attachment Reliability and Figures of Merit for Design for Reliability in Solder Joint Reliability: Theory and Applications." J. Lau, Ed. New York: Van Nostrand Reinhold, 1991, pp. 591-94.
- [48] R. Kotlowitz, "Comparative Compliance of Representative Lead Designs for Surface Mounted Components." IEEE Transactions on Components, Hybrids, and Manufacturing Technology: Vol. 12, No. 4, Dec. 1989.
- [49] R. Kotlowitz and L. Taylor, "Compliance Metrics for the Inclined Gull-Wing, Spider J-Bend, and Spider Gull-Wing Lead Designs for Surface Mount Components." IEEE Transactions on Components, Hybrids, and Manufacturing Technology: Vol. 14, No. 4, Dec. 1991.
- [50] R. Kotlowitz and A. Rizzo, "Comparative Compliance of a Representative Surface Mount Leadless Solder Connection and Commercial Lead Designs." 44th Proceedings of Electronic Components and Technology Conference: 1994.
- [51] S. Timoshenko. *Strength of Materials 3rd Edition*. Malabar: Robert E. Krieger Publishing Company, 1958, p. 60.
- [52] Matweb Material Property Data. Available: <http://www.matweb.com/>.
- [53] CQFP Lead Stiffness Agreement Reference: Performance Characteristics of IC Packages: Ch. 4, Intel, p. 4-32. Available: www.intel.com/design/packtech/ch_04.pdf.
- [54] H. Qi, et. al., "Analysis of Solder Joint Failure Criteria and Measurement Techniques in the Qualification of Electronic Products." IEEE Transactions on Components and Packaging Technologies: Vol. 31, No. 2, June 2008, p. 469-477.

[55] E. Kreyszig. *Advanced Engineering Mathematics, 9th Edition*. John Wiley & Sons, Inc., 2006, p. 1053.

[56] B. Yan, et. al., "The Microstructure of Eutectic Au-Sn and In-Sn Solders on Au/Ti and Au/Ni Metallizations during Laser Solder Bonding Process for Optical Fiber Alignment." IEEE 2006 7th International Conference on Electronics Packaging Technology, 2006.